COMPUTATIONAL FLUID DYNAMIC (CFD) MODELING AND EXPERIMENTAL STUDY OF THE FORMATION AND BUOYANCY-DRIVEN DETACHMENT OF BUBBLES IN VARIABLE GRAVITY ENVIRONMENTS

A Dissertation

by

PAUL ANDREW BURKE

Submitted to the Office of Graduate and Professional Studies of
Texas A&M University
in partial fulfillment of the requirements for the degree of

DOCTOR OF PHILOSOPHY

Chair of Committee,	Bonnie J. Dunbar
Committee Members,	Helen L. Reed
	Edward White
	Richard Cable Kurwitz
Head of Department,	Srinivas R. Vadali

May 2021

Major Subject: Aerospace Engineering

ABSTRACT

The United States and other nations plan to return humans to the surface of the Moon in this decade. On the horizon, the United States plans to send humans to the surface of Mars. Multiphase fluid systems, including boiling heat exchangers, chemical processes, cryogenic fuel management, life-support systems, In-Situ Resource Utilization (ISRU), and microfluidics, will be critical components of human missions to the Lunar and Martian surfaces. Both the Moon and Mars have reduced, or partial gravity environments ($\frac{1}{6}$ g and $\frac{3}{8}$ g, respectively). While much is known about fluids in microgravity, the effects of partial gravity on fluid behavior are not well understood. In microgravity, surface tension dominates fluid behavior, whereas on Earth, buoyancy dominates. Modeling the *transition* from buoyancy-dominated fluid flows to surface tension dominated fluid flows is critical to understanding partial gravity heat and mass transfer.

Of specific importance, is understanding two-phase fluid systems in contact with a solid surface. This research investigates the adiabatic and isothermal formation, growth, and buoyancy-driven detachment of a gas bubble from an orifice submerged in a liquid. Specifically, the effect of gravitational acceleration and orifice plate material surface energy on a bubble's volume at detachment was measured. The research is presented in three phases. First, a theoretical force balance analysis was conducted, in order to isolate the forces acting on a bubble forming at an orifice. Secondly, a volume of fluid (VOF) Computational Fluid Dynamic (CFD) model was developed to model bubble growth and detachment as a function of gravitational acceleration and orifice plate surface energy. Thirdly, the results of the CFD model were validated in 1 g by experiment.

The research presents three important results: (1) The volume of a gas bubble at the point of detachment from a submerged orifice, under gravitational accelerations ranging from microgravity to Earth's gravity (1g), is directly proportional to $g^{-1.5}$, where g is the acceleration due to gravity. (2) Bubble volume at detachment from an orifice is highly dependent upon the apparent surface energy of the orifice plate. This has significant implications for heat and mass transfer in reduced gravity. (3) A new dimensionless quantity, Bu, was derived, which describes submerged orifice bubble behavior across gravity levels and orifice plate materials. Additionally, a critical value of Bu, denoted Bu^*, was derived. For a given material and fluid combination, Bu^* predicts the point at which the bubble will detach from the orifice. Bu^* is constant across all gravity levels and is entirely dependent upon the orifice plate's apparent surface energy and fluid surface tension. The results of this research demonstrate that the design of multiphase fluid systems for the Moon and Mars must involve the judicious selection of materials which are in contact with the fluids.

DEDICATION

To my parents, Kate and Tom.

Thank you for every piece of love and support you have given me every day throughout the years.

To my brother, Brian.

Thank you for the love, support, guidance, and for showing me the way as a great older brother.

To my darling fiancée, Sasheenie.

Thank you for being on my team and for giving me love and support in abundance.

I could not have made it here without the support of my loving family. My accomplishments are their accomplishments.

To the community of lifelong learners and scholars at the University of Virginia. Thank you for the challenges and grand opportunities you offered to me in order to shape me into the inquisitive scholar and academic I am today.

ACKNOWLEDGMENTS

I extend my sincere thanks to the members of the dissertation committee for carefully reviewing this dissertation. I offer a special thanks to Dr. Dunbar for supporting this research, helping me grow as an independent thinker and researcher, and bringing me onto the Aerospace Human Systems Laboratory team as her first doctoral student. I also extend my utmost gratitude to Dr. Reed, Dr. White, and Dr. Kurwitz for being supportive committee members with valuable guidance throughout my academic career. I also thank all members of the Aerospace Human Systems Laboratory (AHSL) and Department of Aerospace Engineering at Texas A&M for supporting and furthering my education. I especially thank former AHSL Master of Science student Daniel Varnum-Lowry who worked innumerable hours by my side and was an excellent lab mate as we learned together and formulated our respective research objectives.

I am also grateful to other research groups for use of their equipment and resources while conducting the research presented in this dissertation. I appreciate the Texas A&M High Performance Research Computing (HPRC) Group for the use of their high-performance computing capabilities when developing and running all CFD models. I also extend gratitude to Dr. David Schechter and I Wayan Rakananda Saputra of the Texas A&M Oilfield Chemistry Rock-Fluid Interaction Lab for use of their goniometer, which helped characterize the orifice plate material properties.

CONTRIBUTORS AND FUNDING SOURCES

Contributors

This work was supported by a dissertation committee consisting of Professor Bonnie J. Dunbar (advisor), Professors Helen Reed and Edward White of the Department of Aerospace Engineering and Professor Cable Kurwitz of the Department of Nuclear Engineering.

The camera calibration and image analysis code were written in collaboration with Master of Science student Daniel Varnum-Lowry and were published in 2020 in his master's thesis within the Department of Aerospace Engineering at Texas A&M University [1]. All other work conducted for this dissertation was completed by Paul A. Burke independently.

Funding Sources

This work was partially funded by the Texas A&M University Aerospace Human Systems Laboratory (AHSL), directed by Dr. Bonnie J. Dunbar, which was financially supported by the Chancellors Research Initiative (CRI). This work was also partially funded by the Texas A&M Presidents Excellence grant entitled *Texas A&M Lunar Surface Experiments Program (LSEP)*, with Dr. Jeff Bullard as Principal Investigator and Dr. Bonnie J. Dunbar as LSEP FLUIDS Experiment Lead. The final semester of work was financially supported by the Aerospace Engineering Ph.D. Graduate Excellence Departmental Fellowship awarded to Paul A. Burke.

NOMENCLATURE

g	Acceleration due to gravity on the Earth's surface (Equal to 9.81 m/s^2)
LEO	Low Earth Orbit
ISS	International Space Station
CFD	Computational Fluid Dynamics
ECLSS	Environmental Control and Life Support Systems
EVA	Extravehicular Activity
EMU	Extravehicular mobility unit
PLSS	Portable life support system
ISRU	In-Situ Resource Utilization
AHSL	Aerospace Human Systems Laboratory
NASA	National Aeronautics and Space Administration
VOF	Volume of Fluid
CLSVOF	Coupled level set and volume of fluid
We	Weber Number
ρ	Density
v	Velocity
D	Characteristic length
σ	Surface tension or surface energy
ESA	European Space Agency
FPS	Frames per second
BXF	Boiling Experiment Facility
MABE	Microheater Array Boiling Experiment

NPBX	Nucleate Pool Boiling Experiment
BDB	Buoyancy dominated boiling
SDB	Surface tension dominated boiling
q	Heat flux
F_B	Force of buoyancy
F_K	Kinetic force of the injected gas
F_I	Inertial force counteracting the hydrostatic pressure during bubble expansion
F_D	Drag force
F_σ	Surface tension/interfacial tension forces
F_w	Weight of the gas
Bu	Bubble scaling number (a dimensionless quantity)
Bu^*	Critical value of the Bubble scaling number, at which bubble detachment occurs
d_o	Orifice diameter
d_b	Bubble diameter
d_c	Contact diameter
d_d	Bubble diameter at detachment
$\rho_{displaced}$	Density of displaced fluid
$V_{displaced}$	Volume of displaced fluid
ρ_{gas}	Density of gas
ρ_g	Density of gas
ρ_{liquid}	Density of liquid
ρ_l	Density of liquid
V_{gas}	Volume of gas contained within bubble
σ	Surface tension
φ	Bubble inclination angle

V_b	Bubble volume
$\Delta\rho$	Difference in fluid densities
V_d	Bubble volume at detachment
$V_{b\,max}$	Maximum bubble volume before detachment begins
$d_{c\,max}$	Maximum contact diameter before detachment begins
$d_{b\,max}$	Maximum bubble diameter before detachment begins
g-BUBB	**G**round-**B**ased apparat**U**s for the study of **B**ubbles and **B**uoyancy
CAD	Computer-aided design
LED	Light-emitting diode
CMOS	Complementary metal oxide semiconductor
USB	Universal serial bus
θ	Equilibrium contact angle
Φ	Free energy ratio
σ_{sg}	Solid-gas surface tension (Solid surface energy)
σ_{lg}	Liquid-gas surface tension
σ_{ls}	Liquid-solid surface tension
V_l	Molar volume of a liquid
V_s	Molar volume of a solid
CV	Computer vision
β	Brightness
Ψ	Contrast
γ	Gamma value
V_b	Bubble volume
t_d	Time of bubble detachment
p	Pressure

u	Velocity in x-direction
v	Velocity in y-direction
w	Velocity in z-direction
t	Time
b_h	Height of bubble
b_w	Width of bubble
AR	Bubble aspect ratio
C	Courant Number
V_{CFD}	Bubble volume at detachment as modeled by CFD
V_{exp}	Bubble volume at detachment as measured by experimental data
1D	One-dimensional
2D	Two-dimensional
3D	Three-dimensional
HPRC	Texas A&M High Performance Research Computing Group
CPU	Central processing unit
ESD	Equivalent spherical diameter
α	Phase Fraction
a	Capillary length
L	Laplace constant

TABLE OF CONTENTS

Page

LIST OF FIGURES

LIST OF TABLES

1. INTRODUCTION

1.1 History and Background

For more than sixty years, the behavior of fluids in variable gravity environments has been a topic of extensive research. The first documented fluids experiment to take place in a microgravity environment was conducted by Mercury astronaut Scott Carpenter on board Aurora 7 in May 1962 [3]. Since then, fluids research has significantly increased with experiments being flown on Skylab and the Space Shuttle [4–6]. Most recently, extensive fluids research has been conducted onboard the International Space Station (ISS) in a microgravity environment [7, 8]. When studying two-phase fluids in convection or buoyancy-driven flows, the gravity levels of interest are discussed in four general categories: terrestrial gravity (1 g), microgravity (10^{-6} g), partial gravity (between 10^{-6} g and 1 g), and hypergravity (greater than 1 g) [9]. Nearly all of the fluids research conducted in space has focused on fluid physics in the microgravity environment of Low Earth Orbit (LEO) [10–26]. Comparatively, little research has been done to study fluids in partial gravity environments. Unfortunately, no fluid experiments were conducted during any Apollo mission. Partial gravity levels are difficult to reproduce in ground-based analog experiments. Drop towers and parabolic flights have been used to produce reduced gravity environments on Earth. However, drop towers and parabolic flights offer limited durations of reduced gravity (maximum of 30 seconds) and often produce large amounts of noise in the acceleration experienced by the experiment [27, 28]. Nonetheless, researchers have been able to successfully conduct limited fluid experiments in parabolic flights and drop towers, such as investigations of boiling heat exchangers, phase separators, and multiphase pipe flows [2, 29–34].

Fluids in containers in microgravity are dominated by surface/interfacial tension forces, while buoyancy is typically neglected [2]. While in the terrestrial and hypergravity regimes, surface and interfacial tension forces are often minimal compared to the buoyant force, which dominates in these regimes. In partial gravity, fluids experience significant influences from both surface/interfacial tension and buoyant forces. The parametric relation between the surface/interfacial tension and buoyant forces versus gravitational acceleration is not well understood and has yet to be thoroughly investigated experimentally. In addition, little research has been conducted to develop Computational Fluid Dynamic (CFD) models of two-phase fluid behavior between 1 g and 10^{-6} g, particularly when the liquid and gas phases are in contact with a solid.

Flows can be characterized in two basic categories: single-phase and multiphase flows. Single-phase flows contain a single fluid phase: either gas or liquid. Two-phase flows are defined as flows which contain both the vapor and liquid phases of the working fluid or dissimilar liquids and gases [35]. Although two-phase fluid systems are complex, they have multiple advantages over their single-phase counter parts. Specifically, two-phase systems save volume, mass, and power. A two-phase flow of interest is bubble formation and detachment.

The study of bubble detachment, primarily through the study of boiling, only commenced just over a century ago [36]. The first thorough theoretical study of boiling was carried out by Lord Rayleigh [37]. The study of boiling and bubbles progressed in the following decades by those such as Nukiyama, who produced boiling curves [38]. Boiling research further progressed as Lee and Merte [39] and Di Marco [40] conducted some of the first boiling experiments on board parabolic aircraft and spacecraft. After experimental work had dominated the study of boiling and bubbles, early numerical simulations started to be developed in the 1990s and early 2000s [36, 41–44]. However, due to the complexity of the problem, and limited computational resources and techniques, many open questions about the fundamental physics of bubble growth and detachment remain [36].

1.2 Importance of Work

Over five decades ago, the first humans stepped foot on the Lunar surface. Humans and animals survive in space due to the presence of environmental control and life support systems (ECLSS). ECLSS is integral to all spacecraft systems which support human life, such as Extra Vehicular Activity (EVA) suits and space habitats. In order to effectively control heat and mass transfer, ECLSS relies on both single-phase and multiphase fluid systems. Even systems which do not involve humans, such as In-Situ Resource Utilization (ISRU) processing, resource extraction, cryogenic fuel systems, phase separators, and heat exchangers, rely heavily on multiphase fluid systems. The applications of fluid physics research are a critical step on the road to human exploration of the Moon and Mars. As NASA and its partners aim to establish a human presence on the Lunar and Martian surfaces in the coming decades, multiphase fluid systems which are designed in Earth's gravity (1 g or 9.81 m/s^2) will be required to operate in microgravity and the partial gravity environments of the Lunar and Martian Surfaces ($\frac{1}{6}$ g or 1.62 m/s^2 and $\frac{3}{8}$ g or 3.71 m/s^2, respectively). A fundamental understanding of two-phase fluids in these gravitational environments will be paramount to future human space exploration.

In microgravity, problems with the nucleation or formation and transport of bubbles have caused significant problems, including reduced flow in heat pipes, the destruction of biological samples utilizing microfluidics, bubbles in intravenous medical systems, and reduced heat transfer in heat exchangers [45, 46]. At present, problems in the International Space Station ECLSS system still occur in LEO which cannot be replicated in 1 g [31]. Many single-phase systems even experience two-phase problems when factors such as corrosion introduce bubble nucleation sites. A fundamental knowledge of the competing effects of buoyancy and surface tension on a bubble attached to a surface is critical for designing exploration systems which do not experience these problems. Modeling bubble formation and detachment in microgravity is an on-going effort; modeling for partial gravity environments, where there is no empirical data, is still in its infancy.

Due to its importance, NASA is very interested in the topic of reduced-gravity fluid physics. Multiple workshops have been held to discuss the critical areas in reduced-gravity fluids research which must be studied [45]. A 2004 report was produced on Critical Issues in Microgravity Fluids, Transport, and Reaction Processes in Advanced Human Support Technology [45]. The report first conveys the fact that nearly all subsystems which involve fluid processes only involve single-phase fluids. In order to improve the efficiency of these systems (both mass and energy efficiencies), the report recommends the implementation of two-phase fluid systems. The report then discusses the lack of experimental flow data in reduced gravity regimes even though fluid flow, heat and mass transfer, and phase separation are all affected by gravity. Therefore, the report stresses the importance of a full understanding of both single and multiphase transport phenomena in order to design the next generation of advanced fluid subsystems. In particular, the report recommends research in the areas of:

1. The understanding of the fundamental fluid physics involved in microgravity boiling.
2. Empirical data for microgravity boiling.
3. The development of models, scaling laws, and empirical correlations for boiling across reduced gravity levels.

Bubble formation and detachment mechanisms are key components of heat and mass transfer due to boiling across all gravity levels. In order to maintain thermal control of heat exchangers across the various environments in which future space hardware will operate, a characterization of the fundamental physics involved in bubble formation (including size, shape, and growth rate) and detachment must be established [45]. The study of bubbles may appear simple on the surface. However, the small time and length scales over which bubbles form and their sensitivity to several interdependent factors, makes exhaustive experimental and computational studies difficult to achieve [36]. It is often advantageous to isolate as many parameters as possible to simplify the study of this complex and dynamic process. The isolated parameters can then be varied to measure their influence on the bubble formation and detachment process [36]. Therefore, to better understand the dynamics of boiling and bubble formation and detachment, the simplified adiabatic case offers several advantages. By forming a single bubble through an orifice or needle injection, thermal effects, such as convection, and bubble-to-bubble interactions can be eliminated [36, 47]. Bubble formation through an orifice also allows for the precise control of environmental conditions, fluid properties, and injection rates. To this end, several researchers have studied, both experimentally and numerically, adiabatic bubble growth and formation from an orifice to more precisely isolate the effects that variables of interest have on bubble behavior [48–59]. Historically however, most numerical solutions and computational models have not been properly validated due to the inability to account for all experimental parameters in the models [36]. There is a need, therefore, to develop models of adiabatic bubble formation and detachment from an orifice and rigorously validate them by experimental data. This will create firm progress towards modeling and understanding more complex processes such as boiling or multi-orifice bubble formation. This research could eventually lead to improved control of bubbles (movement, size, rate of detachment, etc.). The area of bubble control remains an important topic of research, especially as partial gravity could offer some buoyancy-induced control of bubbles, not previously used in microgravity heat exchangers.

2. SCOPE OF RESEARCH AND RESEARCH OBJECTIVES

2.1 Scope of Research

Heat and mass transfer due to bubble formation, detachment, and rise must be carefully understood when designing various space exploration systems, such as Environmental Control and Life Support systems (ECLSS) and heat exchangers. With a variation of temperature and/or pressure, gas bubbles nucleate heterogeneously from a liquid. The bubbles then grow and detach through the force of buoyancy. Although gas bubbles forming through an orifice experience an adiabatic and isothermal environment (as compared to bubbles produced by boiling), they allow for the careful study of the fundamental physics of bubble growth and detachment. Submerged orifice bubble formation allows for the controlled study of the balance between buoyant and interfacial tension forces.

The research presented will report on the modeling and experimental study of single gas bubble formation, growth, and detachment from an orifice submerged in a liquid across a range of gravitational levels and in contact with four different materials of varying surface energies. First, a force balance analysis was conducted. Next, empirical data was collected in 1 g and compared to the 1 g results produced by CFD models, in order to validate the models. CFD was then used to predict bubble size and detachment dynamics in a variety of gravitational environments using the same materials used in the 1 g empirical research. A new dimensionless quantity was then developed to characterize the scaling of bubble behavior across gravity levels and orifice plate materials. The results from the gravity variation study were then compared to the trends predicted by the dimensionless quantity.

Even though there is a need to create in-situ empirical data for partial gravity multiphase fluid experiments, the scope of this dissertation research does not include a flight experiment. It is recognized, however, that the design of hardware and fluid systems in Lunar and Martian gravity environments will require such empirical data in order to fully validate CFD models.

The scope of the experiment which has been conducted and modeled is as follows. The experiment studied gas being passed into a nonflowing liquid phase through a bottom-submerged orifice. Specifically, the experimental and computational research focuses on atmospheric air bubbles forming and detaching from an orifice submerged in distilled water in an isothermal and adiabatic environment. Multiple phenomena can occur during bubble formation and detachment: boiling, chain bubbling, coalescence, and foaming. This research will only study single gas bubble formation and detachment, in which bubble-to-bubble interactions are absent [2]. Bubble rise dynamics are also outside of the scope of this dissertation.

2.2 Research Objectives

The research presented in this dissertation reports on the study of gas bubble formation, growth, and detachment from an orifice submerged in a liquid. The research aimed to validate 1 g CFD models using a custom-designed and calibrated experimental platform across various orifice plate materials. After model validation, the objective of the research focused on modeling bubble formation and detachment in variable gravity environments. At all stages of the research, results were compared to the theoretical force balance analysis and dimensionless quantities. To summarize, the research objectives of this dissertation are as follows:

1. Conduct an analytical study of gas bubble formation and detachment using a force balance analysis.
2. In Earth's gravity (1 g), perform multi-axis high-speed imaging to track the formation and buoyancy-driven detachment of a single gas bubble from an orifice machined into the surface of various substrates (with varying surface energies) submerged in a nonflowing liquid.
3. Use a volume of fluid (VOF)-based Computational Fluid Dynamic (CFD) solver to model the formation and buoyancy-driven detachment of gas bubbles in a nonflowing liquid in 1 g.
4. Validate 1 g CFD models with empirical data collected in the Earth-based experiment.

5. Utilize CFD to model the formation and buoyancy-driven detachment of gas bubbles in a nonflowing liquid in steady-state partial gravity levels between 10^{-6} g and 1 g, especially the gravity on the Moon $\left(\frac{1}{6}\,g\right)$ and Mars $\left(\frac{3}{8}\,g\right)$.

3. LITERATURE REVIEW

There has been extensive research of two-phase fluids in Earth's gravity and multiple research campaigns on fluids research in microgravity. Although fluid systems are expected to be critical in the future of human space exploration, minimal research has been concentrated on two-phase fluids in partial gravity. An extensive literature review was conducted which concentrated on the modeling, experimentation, and scaling of fluid behaviors across variable gravity regimes, in which the dominance of buoyant and surface and interfacial tension forces varies. The proceeding sections will present the major and relevant contributions to the study of bubble formation and detachment in variable gravity environments. Sorted by principal investigator, the review will reveal the open gaps in the field of partial gravity bubble modeling.

3.1 Kulkarni: A Review of Bubble Formation and Gas-Liquid Systems

Kulkarni presents a literature review of all past work (experimental and modeling efforts) which have studied the phenomena of gas bubble formation, detachment, and rise in liquid pools from orifices [60]. His paper is presented as a comprehensive review up to 2005 in order to expose the gaps of knowledge and inform future research investigations.

After reviewing the various modes of bubbling (single, chain, jetting, and foaming), Kulkarni reviews the factors which influence bubble formation. Surface and interfacial tension forces cause the bubble to adhere to the orifice edge, resulting in the delay of detachment. As the bubble grows, the contact angle of the bubble with the orifice changes as surface tension influences the bubble adherence [60]. Once the bubble nears detachment, the surface tension becomes static. Although surface and interfacial tension effects are small compared to other forces in terrestrial gravity, they dominate in reduced gravity regimes and can increase significantly, based on orifice geometry. Liquid and gas density determine the buoyancy experienced by the bubble. As the difference between the two decreases, buoyancy also decreases. Orifice configuration has significant influence on bubble formation. Orifice geometry includes factors such as rim roughness, orifice diameter, and orifice shape. Since the surface and interfacial tension forces are distributed across the entire orifice rim, the amount of surface area in contact with the bubble base can significantly affect detachment. An increase in orifice diameter, for instance, can increase the surface and interfacial tension force acting to resist bubble detachment [60]. Finally, the material of the orifice plate affects the surface and interfacial tension forces, and hence the bubble's adherence to the orifice rim. The influence of orifice plate composition is typically quantified using the bubble's contact angle on the orifice plate material (and therefore the material's surface energy) and the material's wettability [60]. A more wettable orifice plate would result in smaller bubbles since the liquid would adhere to the orifice, inducing bubble necking faster than nonwettable materials [60].

Kulkarni then presents previous methods used to model the mechanism of bubble formation and detachment. In general, the models fall into three categories: single-stage, two-stage, or multistage models [60]. The approaches can be categorized as force balance analysis, dimensional analysis, and finite difference/finite element methods [60]. Since single stage models are widely considered insufficient, two-stage models, first proposed by Satyanarayana, are the most common, consisting of bubble growth/expansion and subsequent bubble detachment as the two stages [61]. In force balance methods, the difference of various forces is analyzed to model the dynamic growth of the bubble. The first stage starts when the bubble crests the orifice level. The second stage starts exactly when the buoyant force is equal to the forces (mainly surface and interfacial tension) which prevent detachment. The second stage ends at detachment. It is often assumed that the gas inflow rate is zero as detachment proceeds, resulting in under estimation of bubble volume under constant flow rate conditions. Under the force balance method, various assumptions are made which are summarized in Table 2 of Kulkarni [60]. These include the neglection of forces, such as surface tension, the drag force, kinetic energy of the injected gas, the weight of the gas in the bubble, etc. The models result in a predicted bubble size (either quantified by bubble diameter or volume at detachment) based on the balance of forces at detachment.

Others have used potential flow theory to model the equations of motion and continuity of bubbles. Wraith was the first to attempt to use potential flow theory [62]. Marmur and Rubin extended Wraith's potential flow theory models to include 11 coupled equations solved using finite difference methods [63]. Finally, others applied potential flow theory by forming a model using the boundary integral method.

Methods have also been developed to model bubbles under special, nontraditional conditions, including non-Newtonian fluids and multi-orifice systems. Most pertinent to this proposed research however, is the growth and detachment of bubbles under reduced gravity. During the expansion of the bubble, surface and interfacial tension forces are dominant. During the phase of bubble detachment, buoyant forces are dominant as the bubble rises and detaches. Buoyancy significantly influences bubble detachment. To better understand buoyancy and other competing forces, it is necessary to isolate the forces [60]. This is done by modeling bubble formation at reduced gravity levels where buoyancy effects are eliminated. When gravity has no influence on the system, individual, less significant forces can be analyzed by viewing the effect of changing values such as viscosity or flow rate. In addition to better understanding the individual forces, bubble formation in microgravity and partial gravity has wide applications in space exploration technologies.

Due to the unavailability of reliable and cheap test platforms, very little experimental work has been conducted in the microgravity regime compared to Earth-based experimental work. Previous experiments and models of bubble formation in reduced gravity are summarized in detail in the below literature search, however, a brief summary is as follows. In microgravity, bubble formation is dominated by and highly sensitive to changes in surface tension and wall adhesion [60]. Under low gas flow rates, bubbles never detach in microgravity and detach at larger volumes in partial gravity than in Earth's gravity. Due to the decreased detachment rate, much work is now concentrated on both active and passive controls of bubble movement and detachment, such as liquid cross flows or orifice plate surface modification. Again, however, much of the work in reduced gravity remains simplified via assumptions and heavily based on theory rather than experimental verification [60].

Lastly, Kulkarni discusses various experimental methods used to research bubble formation and detachment. In transparent liquids, the most utilized and widely accepted data collection method is high-speed (500-2000 frames per second) photography and videography [60]. Bubble properties such as size and shape, are calculated based on a calibrated imaging system.

In conclusion, Kulkarni states that previous research efforts typically concentrate on how the bubble size and shape is affected by the variation of various experimental parameters [60]. Although much work has been conducted in the past, discrepancies remain. He suggests that future advances in computing power and CFD will reveal new and more detailed models of bubble formation and detachment.

3.2 Pamperin: Analysis and Prediction of Bubble Detachment in Microgravity using Weber Number

Pamperin's work was motivated by the fact that bubble formation and detachment in microgravity are not completely understood and have yet to be modeled [64]. Pamperin's work investigated the influence of buoyancy on air bubble formation and detachment from a submerged orifice in water at a constant flow rate of gas. The research was two-fold. First, experimental work was completed in terrestrial gravity and in the microgravity regime by using a 4.7-second drop tower. Theoretical analysis was then conducted using force balance equations and dimensionless parameters, specifically, the Weber Number. It is important to note that Pamperin's work was only conducted in terrestrial and microgravity and did not include any fluid models - only theoretical work, using force balance equations [64]. The equation for Weber Number, which compares the influence of a fluid's inertia to its surface tension, is presented in Equation 3.1.

$$We = \frac{\rho v^2 D}{\sigma} \tag{3.1}$$

Pamperin identified two separate and distinct flow regimes in the microgravity experimental runs [64]. While bubble detachment occurs at all Weber Numbers in terrestrial gravity, Pamperin found that bubble detachment only occurs in microgravity at Weber Numbers greater than ten [64]. The detachment at high Weber Numbers can be attributed to the increase in kinetic energy due to the increased volumetric flow rate of gas into the bubble [64]. It was found that in direct opposition to terrestrial bubble formation, in microgravity, bubble size decreases as Weber Number increases [64]. It was also found that bubble diameter is directly proportional to orifice diameter in microgravity.

To complement and justify the experimental results, Pamperin performed theoretical analysis using force balance analysis. Using the force balance equation(s) and the definition of the Weber Number, Pamperin found that theory only allows bubble detachment to occur when the Weber Number was greater than eight [64]. This critical Weber Number is sufficiently close to the experimentally found critical Weber Number of ten. An important result is thus demonstrated by Pamperin: in direct opposition to terrestrial experiments, bubble detachment in microgravity, occurs only depending upon the Weber Number value [64].

Finally, the most important comparison between microgravity and experimental results is the fact that the behavior of the bubble formation process under both gravity conditions are observed to be similar at Weber Numbers greater than 30 [64]. Thus, as Weber Number increases in both microgravity and terrestrial gravity, bubble sizes approach each other. Therefore, the influence of buoyancy on bubble size decreases as Weber Numbers increase. With regard to the research presented in this dissertation, however, the Weber Number does not consider any variation in gravity and examines fluid which is flowing. As discussed in upcoming sections, the bubbles studied as part of this dissertation detach at gas injection rates which minimize jetting effects.

3.3 Tsuge: Bubble Formation by Low Gas Flow Rates under Reduced Gravity

In order to expand research in the areas of two-phase fluid systems in various space-related applications, Tsuge's research goal was to model bubble formation across varying gravity levels [65]. Tsuge's analytical work and two-dimensional models explored bubble formation across varying gravity levels, including that of the Moon [65]. His experimental work was conducted in microgravity conditions created by the drop tower at the Japan Microgravity Center. The experimental bubble shape and volume measurements agree well with the theoretical ones.

To analytically model the bubble, Tsuge used a non-spherical bubble formation model [65]. The model divides the surface of the bubble into multiple two-dimensional axisymmetric elements. The model resulted in two differential equations, which describe a two-dimensional plane of a bubble which is assumed to be axisymmetric. Tsuge next analytically solved the equations for gravity levels of 1 g, 0.17 g (Lunar), 0.05 g, and 0.01 g [65]. Interesting results are observed from the analysis. First, the volume of the bubble increases with a decrease in gravity level. Next, at lower gravity levels, bubble parameters, such as volume and formation time, are more dependent upon gas flow rate than bubbles formed at higher gravity levels [65]. At low gravity levels (0.01 g) and low gas flow rates, the bubble's volume can be as high as 20 times terrestrial bubble volumes.

During the experimental runs conducted by Tsuge, the bubbles grew in a predicted manner, but did not detach in the ten seconds of microgravity [65]. The bubble shape, as it grew, agreed well with the bubble size and shape as predicted by the analytical model. Although the analytical model and experimental work agreed well, limitations remain in Tsuge's approach. Ten seconds of microgravity forced the gas pump rate to increase to levels which may affect bubble shape and introduce gas jets, which could cause premature bubble detachment. Also, Tsuge's models simply track a two-dimensional slice of the bubble's perimeter, or phase front, without any information on the fluid dynamics within and surrounding the bubble during growth and detachment. Finally, Tsuge's work leaves significant gaps in the range of partial gravity levels examined. Only concentrating on Lunar gravity levels and below, leaves the range between 1 g and Lunar gravity, particularly Martian gravity, completely unexplored.

3.4 Herman: The Control of Bubble Detachment in Microgravity

Herman built upon previous experimental work conducted on bubble formation and detachment in microgravity [46]. In order to enhance heat transfer in pool boiling processes, Herman studied the effect an induced electric field had on a bubble forming at an orifice in a dielectric liquid, PF5052 [66]. All work conducted by Herman was conducted on the KC-135, a parabolic aircraft operated by NASA [67]. Unfortunately, data was unable to be collected in partial gravity regimes due to limited flight opportunities, which resulted on data being collected entirely in microgravity conditions.

In the presence of an electrical field in microgravity, the bubbles were observed to lose their typical spherical shape. The bubbles instead stretched along electric field lines, which Herman used to note that electric fields have potential to greatly improve heat and mass transfer induced by bubble detachment in reduced gravity conditions. Also, in agreement with Pamperin and Rath [64], Weber number was observed to be the best predictor of bubble detachment [68].

In conjunction with the experimental work, models were created. The models were simple, two-dimensional equilibrium models based on force balance analysis developed by Fritz and modified to account for electric field influences [69]. The models assume a spherical bubble attached to a solid surface without an orifice. Similar to Tsuge, the models agree well with experimental results, with some limitations. As mentioned above, the models only tracked a two-dimensional shape of the bubble's perimeter and do not reveal any information on the fluid dynamics within and surrounding the bubble during growth and detachment. Also, g-jitter was observed during parabolic flights and its effects and significance were not accounted for in the models. The assumption of a spherical bubble can be very limiting. As shown in CFD results presented later, bubble shape can change with variations in gravitational acceleration, displaying a deviation from spherical bubbles.

3.5 Suñol: Bubble Formation and Rise in Hypergravity Environments

Suñol conducted bubble rise experiments in artificial hypergravity environments [70]. The hypergravity environment (ranging from 1 g to 19 g) was created by the ESA large-diameter centrifuge [70]. The experiment injected air at a constant flow rate through an orifice into a distilled water fluid chamber. The resulting bubble column was imaged with a 2000 frames per second (FPS) high-speed camera [70].

Suñol's work mainly focused on the bubble's rise trajectory. Although no CFD models were created, force balance diagrams were analyzed to predict the path of the bubble's centroid during rise. Suñol presented the features which are unique to bubble formation and rise in an artificial hypergravity environment. First, bubble size is determined only by gravitational acceleration (buoyant force) and surface tension forces [70]. The bubble's initial trajectory just after orifice detachment, is deviated by the Coriolis force. Subsequent bubble rise experiences oscillatory zig-zag trajectories [70]. These oscillations are not caused by the Coriolis forces, but are due to the fact that vorticity increases with increasing gravity level, thus occurring in hypergravity environments. The vorticity then generates a wake instability which causes the oscillatory zig-zag trajectory. As gravity levels increase, the observed oscillations increase in frequency and decrease in amplitude [70].

Although artificial *partial* gravity could be created in a similar way on a centrifuge in a microgravity environment (on the ISS, for example), Suñol's work presents the limitations of artificial gravity when compared to steady-state partial gravity. In order to apply CFD models to the steady-state partial gravity environments of the Moon or Mars, any Coriolis or vorticity effects must be eliminated. Thus, all CFD models and experiments presented in this dissertation will only study steady-state gravitational environments.

3.6 Kim: Scaling Pool Boiling Heat Transfer Across Gravity Levels

Pool boiling is of great importance to thermal management in reduced gravity regimes. When a liquid comes in contact with a hot component, such as an electrical component which needs to be kept cool, boiling occurs. The superheated gas vapor immediately expands, dramatically decreasing its density [2]. In terrestrial gravity, the buoyant force then makes the bubble rise, inducing cooler liquid to take its place. The amount of heat which is exchanged between the cooling liquid and the heated component is measured by the heat flux of the system. Critical heat flux is the maximum exchange of heat which can occur during boiling. The efficacy of boiling heat exchangers is often measured by the system's critical heat flux [2]. In terrestrial gravity, the critical heat flux is greatly improved by the fact that rising bubbles create mixing within the liquid [2].

In microgravity, the absence of the buoyant force and presence of surface and interfacial tension forces, make the bubbles formed by boiling remain in place on the heated surface. This dramatically decreases the critical heat flux of heat exchangers in microgravity. Pool boiling in microgravity has been studied extensively using the Boiling Experiment Facility (BXF) on board the ISS [71]. These various experiments include the Microheater Array Boiling Experiment (MABE) and the Nucleate Pool Boiling Experiment (NPBX) [2, 8]. While microgravity pool boiling has been studied by multiple investigators, the effect of partial gravity levels on critical heat flux and boiling phenomena had not been studied for decades, until Kim [2]. Kim performed these studies on platinum heater arrays. Kim found that critical heat flux changes dramatically between two regimes (the surface tension dominated boiling (SDB) regime and the buoyancy-dominated boiling (BDB) regime) [2]. The two regimes are separated by a sharp increase in critical heat flux as shown in Figure3.1 below, reproduced from Kim [2]. The effect that gravity has on boiling remains unclear since many of the heat transfer mechanisms which dominate in microgravity are unable to be observed in Earth's gravity [2]. Kim notes that there is much work which remains in regard to boiling and heat transfer in partial gravity since numerical simulations of bubble growth and detachment, although powerful, are still not fully developed. Thus, complete deterministic numerical models of boiling across gravity levels remain for future work [2].

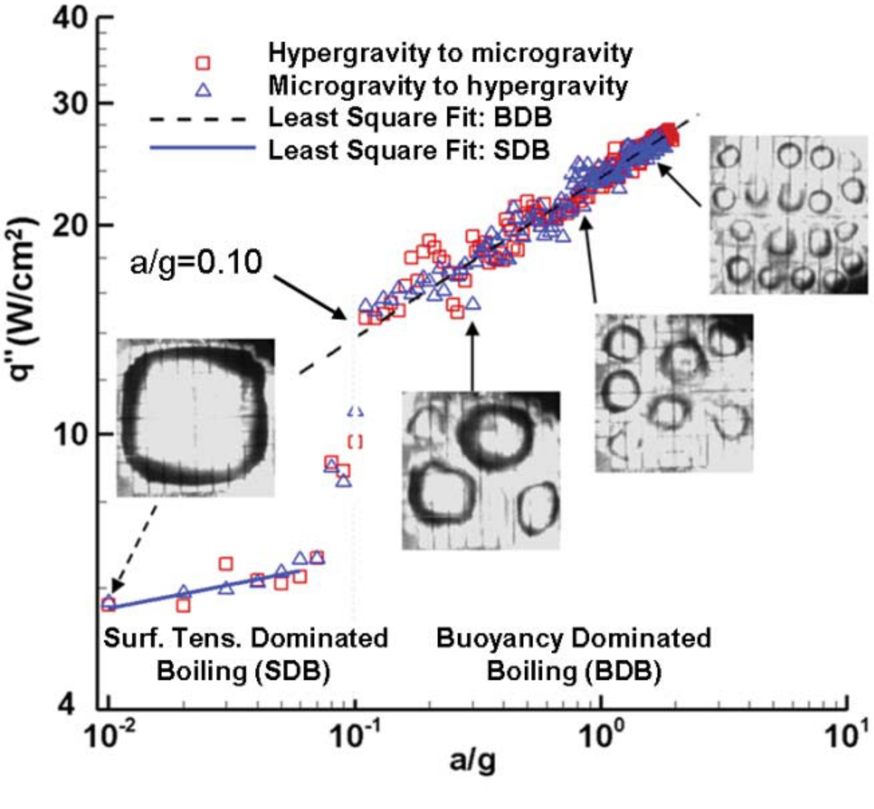

Figure 3.1: Plot of heat flux versus gravitational acceleration. Distinct surface tension and buoyancy dominated regimes are evident. Figure reprinted from Kim [2].

The observation of two distinct regions of heat flux explains why previous attempts to model heat flux versus gravity using a single power law coefficient consistently failed. Yaddanapudi even showed that predicted bubble diameter values obtained from the literature had errors which varied between 26% to 1400% [72]. While other factors influenced heat flux, bubble size was found to have the most significant impact on heat flux [2].

Although pool boiling is not in the scope of the research presented in this dissertation, bubble size and shape at detachment *are* within the scope. Important consideration has been taken therefore, to carefully characterize trends in bubble behavior when scaled across gravity levels. The nonlinear trend observed in Kim's work, for instance, is in direct opposition to the linear and near-linear scaling which is often predicted by traditional scaling methods. It is also important to note the gravity level where this discontinuous jump happens: near Lunar gravity. This means that when designing fluid systems, such as heat exchangers, to operate in Lunar gravity, tests in 1 g may not provide any insight as to how they will operate on the Moon.

3.7 Dhruv: Modeling Pool Boiling in Reduced Gravity

Dhruv presents a numerical modeling effort to model pool boiling dynamics across reduced gravity levels [73]. The model development presented by Dhruv is based off and validated by data from the Microheater Array Boiling Experiments (MABE), which are discussed above. MABE and other related work established a division of pool boiling behavior into two regimes: the surface tension dominated boiling (SDB) regime and the buoyancy-dominated boiling (BDB) regime. The relation between heat flux and gravity levels varies sharply between these regions [29]. Much work has been done to model pool boiling in terrestrial gravity and microgravity. However, gaps remain, especially in the area of high-fidelity models of the fundamental physics and mechanisms of bubble growth and detachment. Dhruv's research is the first high-fidelity model which uses a level-set solver and dynamic contact angles [73]. The model developed is three-dimensional and fully explicit in time.

The model results agree well with Kim's [2] experimental results. Both experimental and CFD results show a lower heat flux in the SDB regime compared to the BDB regime. The boundary of the SDB and BDB regimes is a sharp jump whose location is dependent upon heater size and fluid properties.

Dhruv draws some important conclusions. First, Dhruv's models provide nearly twice the refinement of current models. It is also shown that gravity level has a strong effect on wall heat transfer and boiling characteristics such as bubble size, shape, and behavior. The fundamental physics which are occurring at bubble nucleation and detachment sites are yet to be fully studied and shall be undertaken in the future. Most of the bubble dynamics and cause of bubble detachment being modeled by Dhruv involve bubble-to-bubble interactions. In contrast, this dissertation research focuses on single bubble formation and buoyancy-driven detachment from an orifice, without any bubble-to-bubble interactions.

3.8 Analytical Analysis of Bubble Contours

Before the vast resources of CFD were available, researchers used analytical methods to study the formation and detachment of bubbles. To do this, researchers solved the differential equations for the bubble's contour, or profile [74]. Then, by comparing the analytical solutions to experimental data, empirical correlations could be made. The focus of this research was concentrated on bubbles forming through the process of boiling on a heated plate. Fritz was one of the first to develop such an analytical solution for the diameter of a bubble, formed by boiling, at departure [69, 75]. By solving the differential equation for the contour of a bubble attached to a flat plate, Fritz found that the maximum volume of a bubble could be written as a function (Equation 3.2) of the static contact angle between liquid and wall and the Laplace constant L (Equation 3.3) [69, 75]. Then, assuming a spherical bubble and assuming that the maximum bubble volume occurs at detachment, the bubble diameter at detachment can be expressed in Equation 3.4 [69, 75]. The constant in Equation 3.4 was found by empirical correlation [69, 75].

$$\left(\frac{V_d}{L^3}\right)^{1/3} = f(\theta) \tag{3.2}$$

$$L = \sqrt{\frac{2\sigma}{g(\rho_{liquid} - \rho_{gas})}} \tag{3.3}$$

$$d_d = 0.851 * sin(\theta)\sqrt{\frac{2\sigma}{g(\rho_l - \rho_g)}} \tag{3.4}$$

Son and Dhir expended upon Fritz's work to further refine and validate the analytical solutions through continued empirical validation experiments [76, 77]. Son was able to extend the analytical solutions to not only bubble departure contours, but also bubble contours during growth [76].

Chesters aimed to find similar analytical solutions for adiabatic bubbles which spread beyond orifices, called mode B or Fritz mode [78]. Chesters performed analysis which proved that the detachment diameter of bubbles formed at an orifice, not by boiling, could be modeled by the same equation first proposed by Fritz (Equation 3.4) [78]. Only the constant in the equation changed slightly. Chesters also developed an analytical solution for the maximum amount of bubble spreading beyond the orifice, called the maximum contact diameter. The maximum contact diameter is shown in Equation 3.5, where a is the capillary length [78]. Chesters noted that increased bubble spreading results in larger bubble detachment volumes.

$$d_{c\,max} = 2a\sqrt{\frac{3}{32}}sin(\theta)^2 \tag{3.5}$$

3.9 Simulations and CFD models of Bubble Detachment in 1 g

Due to its simplicity when compared to boiling, adiabatic bubble formation from nozzles and orifices has been an area of interest for many researchers. This research has consisted of the numeric simulation of bubble shape and CFD models of the process of bubble formation and detachment in Earth's gravity. Das used a smoothed particle hydrodynamic (SPH) solver to model bubble growth from a submerged orifice [79]. Das was able to validate the model with experimental data and tune the parameters of the SPH simulation to properly account for the liquid's surface tension [79, 80]. However, unlike the research discussed in this dissertation, Das modeled gas being injected at a constant pressure, instead of a constant flow rate. This created jetting effects, including bubble coalescence and secondary bubble formation [80].

Many researchers have used a coupled level set/volume-of-fluid (CLSVOF) CFD solver to model bubble formation and detachment from submerged orifices and nozzles. Ohta developed an experimentally verified CLSVOF CFD model of bubbles growing and detaching from a submerged nozzle, where the bubble is pinned at the nozzle edge [81]. Similar to Das, Ohta studied fast gas injection rates in which significant bubble-to-bubble interactions were present [82]. Again, the research presented in this dissertation aims to eliminate jetting effects by minimizing gas injection rates. Chakraborty also used a CLSVOF solver to model bubble growth and detachment in 1 g. However, Chakraborty's primary goal was to study the influence of outside forces, such as cross flows, wall effects, and bubble pairing, on premature bubble detachment and bubble shape [83, 84]. The addition of other forces, such as cross flows, obscures the balance between buoyancy and surface and interfacial tension forces on a bubble.

Gerlach presents extensive research on the modeling of bubble formation and detachment in 1 g. Gerlach studied both bubble coalescence and single bubble formation and detachment [85]. Due to its relevance to this dissertation, Gerlach's work on single bubble formation will be the concentration of the below summary. Gerlach's CFD models utilize a CLSVOF solver to simulate an axisymmetric bubble forming and detaching from a submerged orifice at a constant gas injection rate [86]. First, Gerlach notes that bubbles can form at an orifice in two modes: mode A in which the bubble remains pinned to the orifice perimeter, and mode B in which the bubble spreads beyond the orifice. The presence of bubble spreading, Gerlach explains, is dependent upon the orifice plate material's static contact angle boundary condition [87]. Bubble spreading typically occurs at smaller orifices and when the instantaneous contact angle falls below the static contact angle [87]. After validating the CFD models, Gerlach presents some important conclusions. First, bubble volume at detachment is significantly affected by the orifice plate material [87]. When mode B growth and bubble spreading occurs, the bubbles increase in volume significantly [87]. As the static contact angle of the material increases, the bubble's volume at detachment increases cubically [86].

Next, bubble volume at detachment is also dependent upon gas injection rate [86]. However, at low enough gas injection rates, the bubble volume approaches a constant value [86]. This indicates that jetting effects are minimized at these low gas injection rates. Many aspects of Gerlach's CFD models, such as the static contact angle boundary condition, axisymmetric assumption, and gas injection rates, are similar to the CFD models presented in this dissertation.

3.10 Di Bari: Numerical Study of the Effects of Gravity on Bubble Formation and Detachment

Building off of models of bubble formation and detachment in 1 g, Di Bari conducted one of the first studies of bubble formation and detachment from an orifice in variable gravity environments. Di Bari used TransAT, a commercial level-set CFD solver, to model adiabatic bubble growth and detachment from a 1 mm diameter aluminum orifice [36]. Di Bari first validated the CFD models in 1 g against empirical data collected by high-speed imagery [88]. He found great agreement between the CFD model and experimental data when comparing key parameters such as bubble center of gravity, bubble perimeter location, and bubble volume at detachment [36]. After 1 g model validation, Di Bari modeled bubble detachment at the variable gravity levels of 0.1 g, 0.5 g, and 1.5 g [36]. Due to computational limitations, the 0.1 g model had to be stopped before completion and was not included in the data set. Di Bari found some general trends in bubble behavior across gravity levels. First, as bubbles grew at all gravity levels, the bubbles spread beyond the orifice during growth before returning to the orifice rim just before detachment [36]. Next, at any given volume, the bubble's center of gravity decreased at gravity decreased [36]. Most applicable to this dissertation, Di Bari found a correlation between the bubble volume at detachment from an orifice and gravitational acceleration. Di Bari found that the bubble volume at detachment had an inverse relationship with the gravitational acceleration according to Equation 3.6 [36].

$$V_d \propto g^{-1.058} \tag{3.6}$$

Some limitations exist in Di Bari's work, however. First, only an aluminum orifice plate was tested. This means that the influence of the solid material's surface energy on bubble volume was never studied. Most importantly, Di Bari only modeled bubble formation and detachment at three gravity levels: 0.5 g, 1 g, and 1.5 g. Di Bari's correlation of bubble volume versus gravity level ($V_d \propto g^{-1.058:}$) is only based on a single partial gravity data point: 0.5 g. Many gaps remain in the study of *partial gravity* bubble detachment.

3.11 Qui: Experimental Investigation of Pool Boiling across Variable Gravity Levels

In collaboration with the NASA Glenn Research Center, Qui conducted an extensive experimental investigation of bubble dynamics during pool boiling under reduced gravity [89]. The experiment studied bubbles nucleating and detaching from a silicon heater submerged in distilled water [89]. After collecting data in the lab in 1 g, reduced gravity experiments were conducted on the KC-135 parabolic aircraft. Bubbles were imaged with high-speed imagery as the plane completed parabolic flight profiles. Data was continuously collected across all parts of the parabolic profile to obtain a data set ranging from 0.03 g to 1.8 g. The experiments resulted in many important conclusions. First, the location of bubble nucleation could be controlled by etching a small imperfection within the silicon heater [89]. However, it was found that accelerations in the off-axis directions caused the bubbles to slide and detach prematurely. Next, time to bubble detachment was significantly influenced by heater subcooling and gravity level [89]. Most importantly, it was found through empirical correlation that bubble detachment volume scaled inversely proportional to gravity level according to 3.7 [89].

$$V_d \propto g^{-1.5} \tag{3.7}$$

This scaling is significantly different from the scaling modeled by Di Bari ($V_d \propto g^{-1.058}$) and could be caused by two different factors. First, it is possible that bubble formation from an orifice is significantly different from pool boiling in reduced gravity regimes and thus, the bubble volume scales differently with gravity level. It is also possible that Di Bari did not collect enough data across the wide range of partial gravity levels.

Just like Di Bari's work, limitations exist in Qui's research. First, the scaling of bubble volume versus gravity level was entirely determined via empirical correlation. No models were developed and no theoretical force balance analysis was conducted. Secondly, all gravity levels created by the plane were transient. At any gravity level between the minimum (0.3 g) and maximum (1.8 g), the experiment was experiencing constantly changing accelerations. Qui's data reports only the g-level at the moment of bubble detachment, while not considering the gravity level during bubble growth. Lastly, significant g-jitter was experienced, leading to off-axis accelerations and premature bubble detachment. It is evident from Qui's research that bubble behavior in reduced gravity remains not fully understood nor modeled.

4. FORCE BALANCE ANALYSIS

As stated in Section 2.1, bubble formation can occur under various modes: single bubble, chain bubbling, and jetting, to name a few. This research has only focused on the formation and detachment of single bubbles from an orifice submerged in a liquid. As a single bubble grows from an orifice, six forces act upon it. These forces are: the buoyant force ($\boldsymbol{F_B}$), the drag force ($\boldsymbol{F_D}$), the interfacial and surface tension force ($\boldsymbol{F_\sigma}$), the inertial force counteracting the hydrostatic pressure during bubble expansion ($\boldsymbol{F_I}$), the inertial force due to kinetic energy of the injected gas ($\boldsymbol{F_K}$), and the weight of the gas contained in the bubble ($\boldsymbol{F_w}$). Bubble growth can occur in two modes: mode A and mode B [78, 90]. Mode A bubble growth is defined as bubble growth during which the bubble boundary is constrained to the orifice rim [78]. Mode B bubble growth occurs when the bubble spreads beyond the edge of the orifice during growth [78]. Mode A occurs on orifice plates with low equilibrium contact angles (more wetting) and mode B occurs on orifice plates with higher equilibrium contact angles (less wetting). Figure 4.1 shows a force balance diagram containing all six forces which can act on a bubble forming at a submerged orifice.

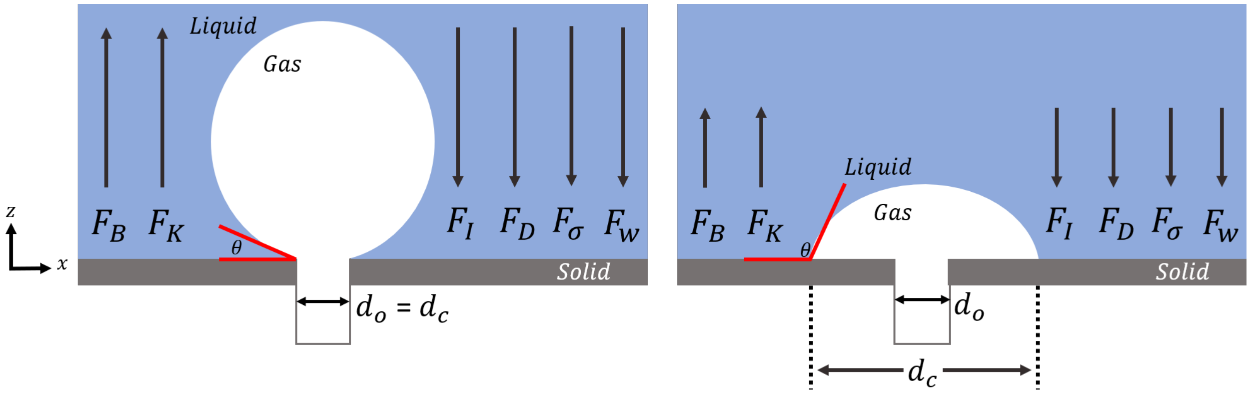

Figure 4.1: Force balance diagram showing all six forces which act on a bubble forming at a submerged orifice. Two modes of bubble growth are shown: mode A (left) which is pinned to the orifice rim and mode B (right) which spreads beyond the orifice.

Besides the forces, Figure 4.1 displays other parameters important to bubble growth and detachment. The equilibrium contact angle is shown as θ. As discussed, mode A occurs when the contact angle is small. The orifice diameter is labeled as d_o. The contact diameter d_c is defined as the diameter of the bubble cross section which is in contact with the orifice plate. In the case of mode A growth, $d_c = d_o$, since the bubble is constrained to the orifice rim. In the case of mode B bubble growth, d_c changes as the bubble grows and is greater than d_o.

The force balance can be stated as:

$$\sum \boldsymbol{F} = \boldsymbol{F_B} + \boldsymbol{F_K} + \boldsymbol{F_I} + \boldsymbol{F_D} + \boldsymbol{F_\sigma} + \boldsymbol{F_w} = 0 \tag{4.1}$$

The primary research objective was to study the *buoyancy-driven* detachment of bubbles from a submerged orifice. Only the simple balance between buoyancy, bubble weight, and interfacial tension forces was studied. To this end, every effort was made to eliminate the effect that any other force has on the bubble, by injecting the gas through the orifice at sufficiently low flow rates. As explained below, the following force balance analysis will assume that at sufficiently low gas injection rates, $\boldsymbol{F_D}$, $\boldsymbol{F_K}$, and $\boldsymbol{F_I}$ can be neglected.

The inertial force ($\boldsymbol{F_I}$) is the force, created by the hydrostatic pressure due to the column of fluid above the orifice, that the bubble must overcome as the phase front expands against the hydrostatic pressure of the liquid. This force is in the negative z-direction, as it counteracts the expansion of the bubble [60]. At low gas injection rates, the bubble is assumed to experience quasi-static expansion. Since bubble detachment occurs so fast, relative to gas injection and bubble expansion, the bubble's phase front is assumed to not be expanding during these moments and $\boldsymbol{F_I}$ is neglected.

The drag force ($\boldsymbol{F_D}$) is a force in the negative z-direction, counteracting the growth and rise of the gas bubble. The drag force is velocity dependent. As the bubble grows, and especially as it rises, the centroid of the bubble has a velocity in the positive z-direction. As the centroid of the bubble and the phase front move through the water, the water exerts a force upon it, which opposes motion. Whereas the bubble experiences significant drag as it rises, the bubble's centroid has minimal velocity when the bubble remains attached to the orifice during bubble growth. Again, at sufficiently low gas injection rates, the bubble experiences a negligible amount of drag force during growth and detachment.

The kinetic force ($\boldsymbol{F_K}$) of the gas is a force in the positive z-direction, forcing the bubble to detach from the orifice. As the inlet gas flows through the orifice and into the bubble, the gas which enters the fluid chamber gives the gas molecules within the bubble a certain amount of kinetic energy and imparts a force upon them. The molecular collisions and momentum transfer between the inlet gas and the bubble gas exerts an upward force on the bubble, promoting detachment. This phenomenon is sometimes called jetting. At sufficiently low gas injection rates, the bubble experiences a negligible amount of jetting and $\boldsymbol{F_K}$ can be neglected.

After the neglection of $\boldsymbol{F_D}$, $\boldsymbol{F_K}$, and $\boldsymbol{F_I}$, the force balance can be simplified, as shown in Equation 4.2.

$$\sum \boldsymbol{F} = \boldsymbol{F_B} + \boldsymbol{F_\sigma} + \boldsymbol{F_w} = 0 \tag{4.2}$$

The buoyant force ($\boldsymbol{F_B}$) is defined as the upward force exerted by a fluid on an object which is submerged in the fluid. The buoyant force is equal to the weight of the fluid which is displaced by the object, in this case a gas bubble. The equation for the buoyant force is shown in Equation 4.3, where $\rho_{displaced}$ and $V_{displaced}$ are the density and volume of the displaced fluid, respectively. The density of the displaced fluid and the gravitational acceleration term in the equation are both constant in steady-state gravity environments. The only term which varies with time is the volume of the gas bubble, as gas is pumped through the orifice.

$$\boldsymbol{F_B} = \rho_{displaced} * g * V_{displaced} \tag{4.3}$$

The weight of the gas ($\boldsymbol{F_w}$) is directly related to the gravitational acceleration. The weight of the gas is the product of the gas density, bubble volume, and gravitational acceleration. Weight is a force in the negative z-direction, counteracting bubble detachment. The equation for the bubble's weight is displayed in Equation 4.4 where ρ_{gas} and V_{gas} are the density and volume of the gas, respectively.

$$\boldsymbol{F_w} = -\rho_{gas} * g * V_{gas} \tag{4.4}$$

The surface tension and interfacial tension forces ($\boldsymbol{F_\sigma}$) act in the negative z-direction, counteracting the detachment of the bubble from the orifice. The surface tension force results from the intermolecular attractions between liquid molecules which are in contact with a gas phase. The interfacial tension force is due to the molecular attraction of the orifice plate to the phase boundary between the liquid and gas. Therefore, surface tension maintains a bubble's shape and prevents necking, while interfacial tension prevents the detachment of the bubble from the solid orifice plate. Interfacial tension forces are higher in mode B bubble growth, compared to mode A bubble growth. That is, the larger the contact diameter, the larger the interfacial force. Equation 4.5 presents the equation for the interfacial and surface tension force, where d_c is the contact diameter. Equation 4.5 can handle both mode A and mode B bubble growth by setting $d_c = d_o$ during mode A bubble growth. The bubble's inclination angle, φ, is defined as $tan^{-1}(x(t)/y(t))$, where $x(t)$ and $y(t)$ are the coordinates of the bubble centroid [91, 92]. Since the bubble rises vertically, φ is equal to zero degrees [91].

$$\boldsymbol{F_\sigma} = -\pi * d_c * \sigma * cos(\varphi) = -\pi * d_c * \sigma \tag{4.5}$$

Substituting equations 4.3, 4.4, and 4.5 into equation 4.2 gives equation 4.6.

$$\sum \boldsymbol{F} = \rho_{displaced} * g * V_{displaced} - \pi * d_c * \sigma - \rho_{gas} * g * V_{gas} = 0 \tag{4.6}$$

Noting that the volume of the gas bubble (V_{gas}) is equal to the volume displaced ($V_{displaced}$) and the displaced fluid is a liquid, the equation simplifies to equation 4.7.

$$\sum \boldsymbol{F} = (\rho_{liquid} - \rho_{gas}) * g * V_{gas} - \pi * d_c * \sigma = 0 \tag{4.7}$$

Occurring immediately after the expansion stage, the detachment stage is the stage in which the downward forces (which favors bubble attachment) are completely balanced by the upward forces, which favor bubble detachment. At the instant the upward forces exactly equal the downward forces, Equation 4.7 is completely balanced. The minimal amount of gas injected at the next instant increases the magnitude of the upward (buoyant) force on the bubble to a level which is differentially larger than the downward forces on the bubble. When this occurs, the detachment stage then sees the necking of the bubble. Necking is a phenomenon caused by surface tension which ends with the complete detachment of the bubble from the orifice. Once the bubble is detached, the bubble subsequently rises vertically in the liquid phase. The present study will not examine the rise of bubbles.

5. EXPERIMENTAL METHODOLOGY

An experimental platform was developed to study gas bubble formation, growth, and detachment from an orifice submerged in a liquid in Earth's gravity. This section presents the experimental setup, calibration procedures, image capture and processing method, and the accuracy of the experimental platform. The variables tested in the experiment will subsequently be presented. This section of experimental methodology is presented before the CFD methodology since several components of the experimental methodology informed the boundary conditions and geometry of the CFD model.

5.1 Experimental Setup

The **G**round-**B**ased apparat**U**s for the study of **B**ubbles and **B**uoyancy (g-BUBB) is an Earth-based experimental platform developed by the Aerospace Human Systems Laboratory. Its purpose is to capture high-speed imagery of single gas bubble formation, growth, and detachment from an orifice submerged in a liquid. The platform is based off of a simplified version of the experimental setup used by Herman to study the formation and detachment of bubbles [67]. Similar to Herman's experimental platform, g-BUBB is comprised of a fluid chamber, a gas injection system, and an imaging system. All data and command are controlled by a laptop computer and Raspberry Pi microcontroller. A CAD assembly of the experimental setup is shown and labeled in Figure 5.1. A photograph of the physical experimental platform is shown and labeled in Figure 5.2.

5.1.1 Fluid Chamber

To facilitate the imaging of the gas bubbles, the custom-built fluid chamber was made of transparent, $1/8^{th}$-inch polycarbonate. The fluid chamber was a square cylinder with a height of 60 mm and a side length of 50.8 mm. The bottom of the fluid chamber was constructed with a polycarbonate interface plate. The interface plate served as the interface between the gas injection system and the orifice plate, through which gas was injected into the fluid chamber. The interface plate sealed to the bottom of the fluid chamber using an O-ring and four screws. Orifice plates, each

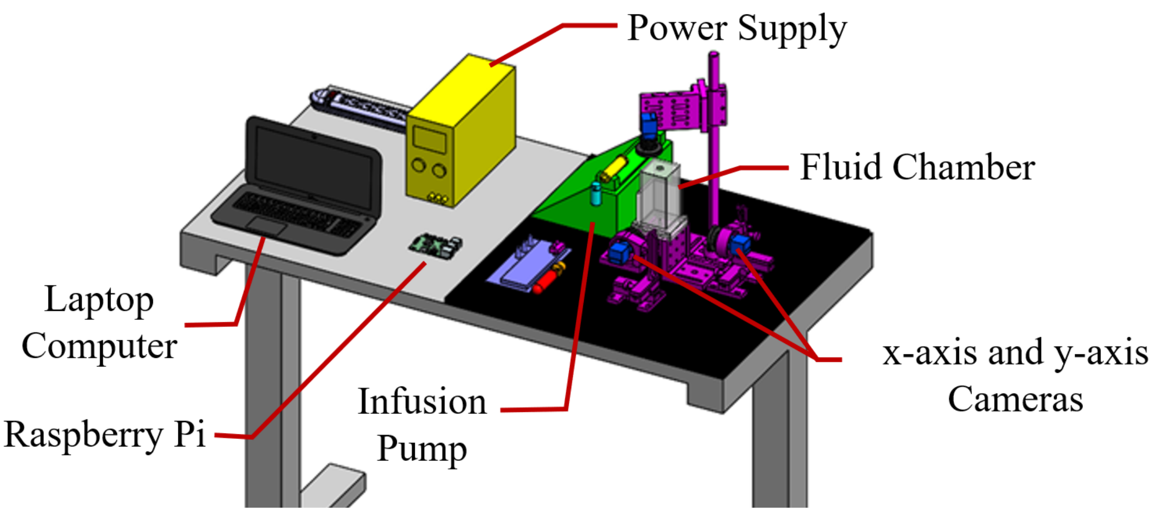

Figure 5.1: CAD assembly of the g-BUBB experimental platform.

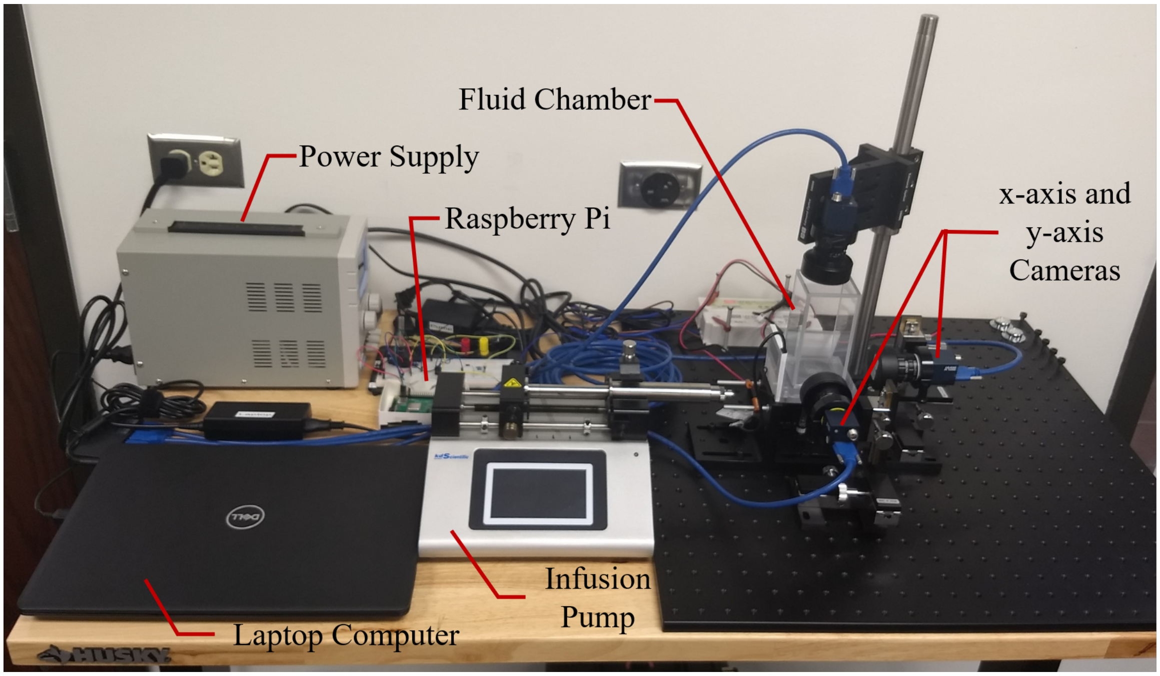

Figure 5.2: Photograph of the g-BUBB experimental platform. All experimental data presented in this dissertation was collected on the shown experimental setup.

containing a single 0.8 mm-diameter orifice in the center, were mounted on top of the interface plates. The interface plates were interchangeable, to allow for the testing of multiple orifice plate materials, including quartz, polycarbonate, stainless steel, and aluminum. When designing the orifice plate and fluid chamber, special attention was given to the orifice diameter and fluid chamber wall dimensions. Albadawi found that fluid chamber wall effects can be neglected if the width of the chamber walls are five times the bubble radius at detachment [93]. Following this recommendation, the final design included an orifice diameter of 0.8 mm and a fluid chamber with 50.8 mm wide walls. As discussed in Section 7.2, the largest bubble observed experimentally had a radius of 2 mm. Thus, the fluid chamber walls are more than ten times the bubble radius, and wall effects can be neglected. Dimensioned drawings of the fluid chamber and orifice plates are displayed in Figures A.1, A.2, A.3 in Appendix A. The parts of the fluid chamber, including the orifice plates, are shown in a simplified diagram in Figure 5.3.

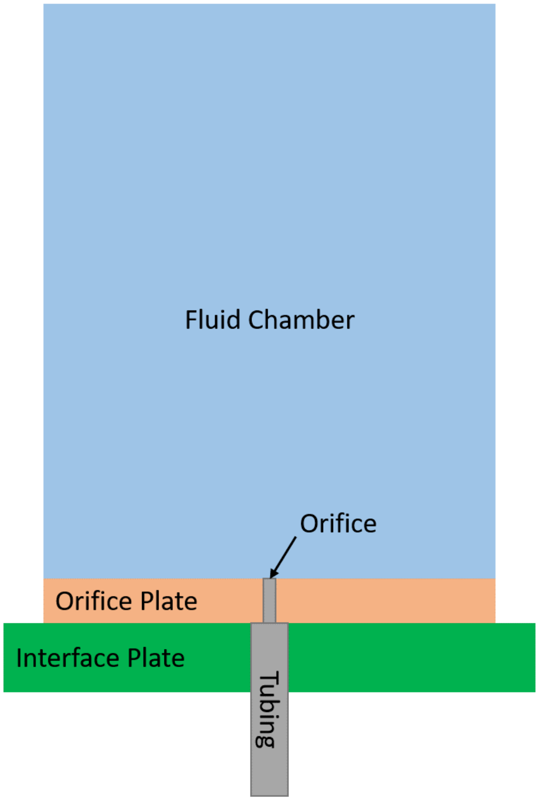

Figure 5.3: Labeled diagram showing all parts of the experimental fluid chamber system.

5.1.2 Gas Injection System

The purpose of the gas injection system was to inject small amounts of gas at a constant volumetric flow rate through the orifice and into the fluid chamber. Commercially available components were chosen for the gas injection system. First, a Legato 110 medical infusion pump was used to inject the gas at volumetric flow rates as low as 44 nanoliters per minute and as high as 45 milliliters per minute. The syringe, being pumped down by the infusion pump, was a Harvard Apparatus 20-milliliter, gas-tight, stainless-steel syringe (model 70-2254) [94]. The infusion pump pumps the gas though Tygon tubing, which connects to the fluid chamber via the interface plate. The temperature and humidity of the ambient air (used as the injected gas) was measured and recorded by a PerfectPrime Data Logger (model TH1165) [95]. The temperature of the liquid was measured by a Thermco liquid thermometer (model ACC340DIG). An image of the infusion pump is shown in Figure 5.4.

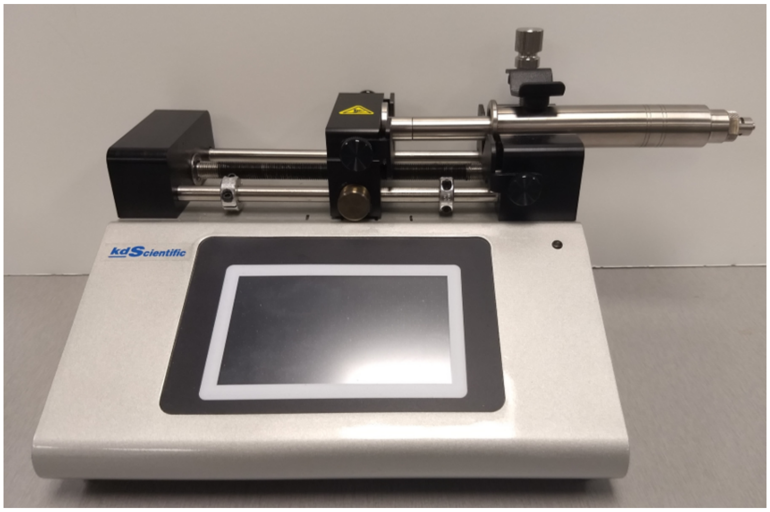

Figure 5.4: Photograph of the Legato 110: the infusion pump used to inject gas through the orifice and into the fluid chamber.

5.1.3 Two-Axis Imaging System

As noted by past experimentalists, the typical and most accurate method for measuring a bubble's volume is via a calibrated, high-speed imaging system [64, 65, 96]. Post-processing tools are used to determine the bubble's volume within each frame. The imaging system designed and utilized in this dissertation offers an improvement upon past work. Instead of the standard single-axis camera technique, this research utilizes a multi-axis imaging system and shadowgraphy technique. Two 60-watt LED panels were placed on two orthogonal sides of the fluid chamber so that the bottom of the LED panel was level with the orifice. Each LED was a 2-inch square panel, manufactured by LEDCONN. On opposite sides of the fluid chamber from the LED panels, two black-and-white CMOS high-speed cameras (Daheng Imaging MER-031-860-U3M) were placed so that the cameras were orthogonal and that the center line of the camera aligned with the level of the orifice. The cameras and fluid chamber were secured in place by optical table mounts. Each camera could record video at a resolution of 224 by 342 pixels at 950 to 1100 frames per second, depending on the length of the video [97]. Attached to the cameras were 3.5 mm fixed focal length lens, manufactured by Edmund Optics [98].

The LED panels backlit the fluid chamber, enabling the use of a shadowgraphy imaging technique [99–101]. The two cameras allow for video capture of two orthogonal two-dimensional slices of the bubble at any moment in time. The two axes in which video capture occurred were defined as the x-axis and y-axis. Figure 5.5 shows an image of the high-speed camera and lens system.

5.1.4 Command and Data Handling System

All data and commands were handled through a Dell Latitude 3490 laptop computer and Raspberry Pi 3 B+ microcontroller. A custom-written Python script handled all data and commands through the system. Power was provided to the laptop, Raspberry Pi, and infusion pump from 120-volt wall outlets and appropriate power adaptors. The cameras were powered through USB 3.0 connections from the laptop. Using the same USB connection, image capture commands were

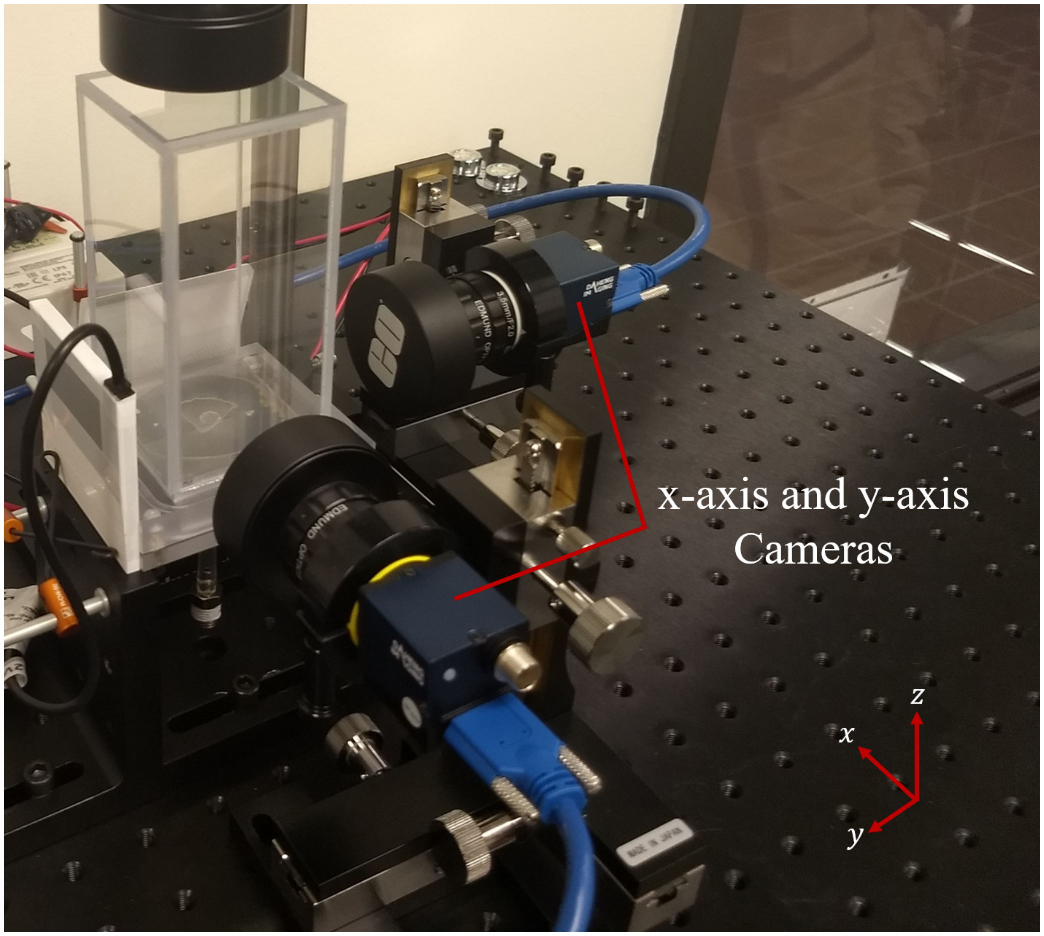

Figure 5.5: Photograph of the g-BUBB high-speed imaging system, including a set of reference coordinate axes.

sent from the laptop to the high-speed cameras and the frame data was sent from the camera to the laptop. Each frame was saved as an individual JPG file. Image capture was the only data collected by the imaging and gas injection systems. Using the same Python script, the laptop sent pumping commands through an ethernet connection to the Raspberry Pi and subsequently to the infusion pump. The laptop and Raspberry Pi work in a master/slave system, where the laptop commands the Raspberry Pi to execute commands to other peripheral components, in this case, the infusion pump [1]. A systems diagram of the command, data, and power systems of g-BUBB is shown in Figure 5.6.

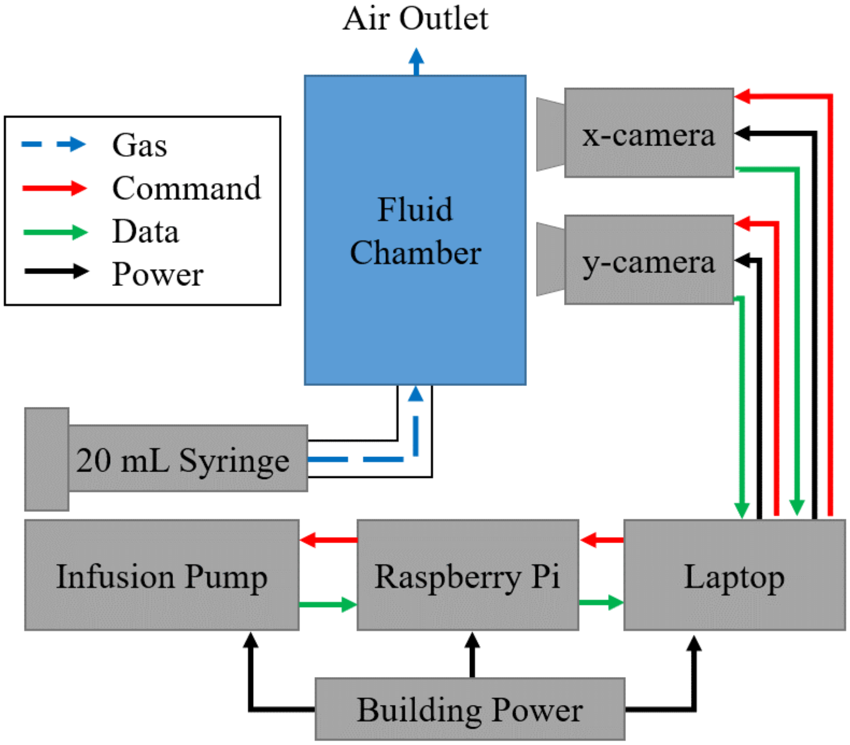

Figure 5.6: Systems diagram of the g-BUBB command and data handling, gas injection, and imaging systems.

5.2 Sessile Drop Contact Angle Measurements

Before conducting any experimental trials, the experimental platform had to be properly characterized. More specifically, the orifice plates had to be characterized. Since the primary purpose of the 1 g experimental platform was validation of CFD models, all orifice plate materials had to be characterized to ensure that the boundary conditions imposed in the CFD models matched with the actual properties of the experimental fluid chamber and orifice plates. As discussed in Section 6, the boundary condition of interest was the equilibrium Sessile drop contact angle on each orifice plate.

Before measurement of the contact angle, all orifice plates were machined to 2-inch by 2-inch squares and had 0.8 mm orifices drilled in their centers. After machining, each orifice plate was polished using a water-fed, manual polishing wheel. The polishing process was performed to ensure a uniform surface topology and surface roughness across the orifice plate. Each orifice plate was polished using the same grit progression: 400 → 600 → 1200 → 2000. The duration on each grit varied greatly between each orifice plate material. In between each grit, the sample was rinsed with distilled water and dried with compressed air. After polishing the plates on the 2000 grit sandpaper, diamond slurries and polishing clothes were used to achieve the final polish. The progression of the diamond slurries is as follows: 6 μm $\rightarrow$ 3 μm $\rightarrow$ 1 μm $\rightarrow$ 0.5 μm $\rightarrow$ 0.1 μm. Again, the orifice plates were washed with distilled water and dried with compressed air following each stage of the polishing process.

After each plate was polished, the plates were brought to the Texas A&M Oilfield Chemistry Rock-Fluid Interaction Laboratory. Contact angles measurements were performed by a Dataphysics OCA 15 Pro goniometer [102]. Figure 5.7 shows an image of the goniometer used to conduct all contact angle measurements.

Figure 5.7: All Sessile drop contact angle measurements were performed on the Dataphysics OCA 15 Pro goniometer.

On the polycarbonate, stainless-steel, and aluminum orifice plates, 10 contact angle measurements were recorded. For quartz, since the standard deviation of the measurements was higher than the other plates, 20 contact angles were measured and recorded. All contact angle measurements were performed on the bulk, non-machined material away from the orifice. The location of each measurement can be summarized by Figure 5.8.

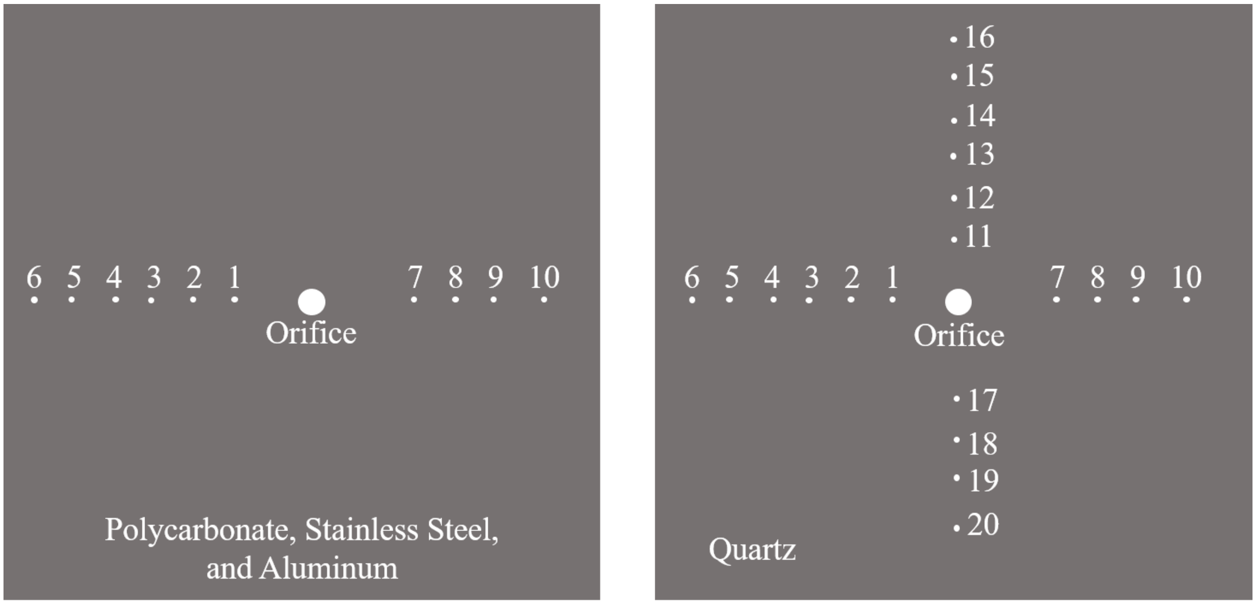

Figure 5.8: Location of Sessile drop contact angle measurements as performed on the goniometer. Ten measurements were performed on the polycarbonate, stainless-steel, and aluminum orifice plates (left), while twenty measurements were performed on the quartz orifice plate (right).

A sample contact angle measurement on stainless steel outputted by the goniometer software (SCA20_U) is shown in Figure 5.9. Note that the left and right contact angles are nearly equal, indicating symmetry in the drop, and thus uniformity in the surface properties.

After all measurements were recorded, the contact angles (θ) were averaged and the standard deviation was calculated for each orifice plate. To be clear, the method of contact angle measurement (placing the drop on the plate via a syringe) means that all contact angles measured and reported here are advancing contact angles. Since the droplets were at rest during the measure-

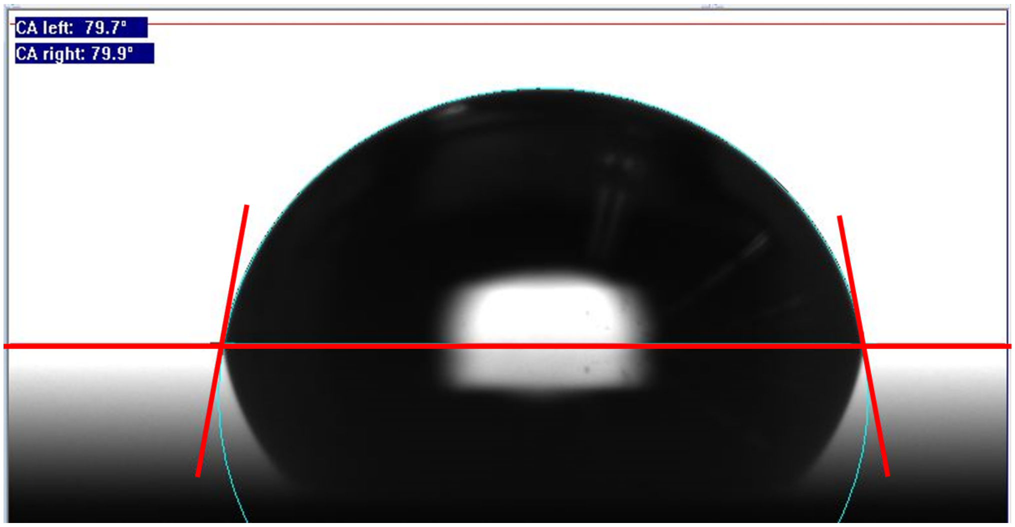

Figure 5.9: A sample contact angle measurement, as performed by the goniometer on the stainless-steel orifice plate.

ments, they will be referred to as the equilibrium contact angle from this point forward. Using Equations 5.1 and 5.2, the surface energy (σ_{sg}) for each material was also calculated. The averaged contact angle, calculated surface energy, and surface energy range from the literature are reported in Table 5.1. The surface energy reported from the literature for aluminum assumes that a thin layer of alumina forms on the aluminum sample upon contact with air [103, 104].

$$cos(\theta) = 2\Phi \left(\frac{\sigma_{sg}}{\sigma_{lg}} \right)^{\frac{1}{2}} - 1 \tag{5.1}$$

$$\Phi = \frac{4(V_s * V_l)^{\frac{1}{3}}}{\left(V_s^{\frac{1}{3}} * V_l^{\frac{1}{3}} \right)^2} \tag{5.2}$$

For each orifice plate, the surface energy, as calculated from the measured equilibrium contact angle using Equations 5.1-5.2, fell within the range of the published literature.

Table 5.1: Equilibrium Sessile drop contact angles and surface energies of orifice plates

Orifice Plate Material	**Measured Sessile Drop Contact Angle (Degrees)**	**Standard Deviation (Degrees)**	**Calculated Surface Energy (mJ/m^2)**	**Published Surface Energy (mJ/m^2)**
Quartz	46.24	5.75	51.67	30 - 76 [105]
Polycarbonate	73.06	0.91	41.48	34 - 50 [106]
304 Stainless Steel	80.35	1.69	25.79	25.5 - 30.7 [107]
Aluminum 6061	77.38	1.86	27.25	23.2 - 33.1 [104, 108]

5.3 Experimental Procedures

After polishing and characterizing each orifice plate, experimental trials of gas bubble formation and detachment were conducted. A full experiment involved three basic processes. The three stages were: camera calibration, experimental trials, image post-processing. The experimental procedures were identical for each orifice plate, so the subsequent sections will discuss the standard experimental procedures, regardless of variables tested. The flowchart in Figure 5.10 summarizes the experimental process presented in proceeding subsections.

5.3.1 Calibration of Imaging System

As discussed in the Contributors Section, the calibration code and methodology was originally developed and written in collaboration with Master of Science Student Daniel Varnum-Lowry. Preliminary methodology and results were published in Varnum-Lowry's thesis [1] and have since been developed further as part of this dissertation. The imaging system was calibrated for two purposes: determination of distortion parameters and determination of a scale factor. All imaging systems contain some amount of distortion. The first stage of the camera calibration process measured this distortion in order to remove it during post-processing. The second stage of camera calibration was to determine a scale factor which allowed for the measurement of real, physical

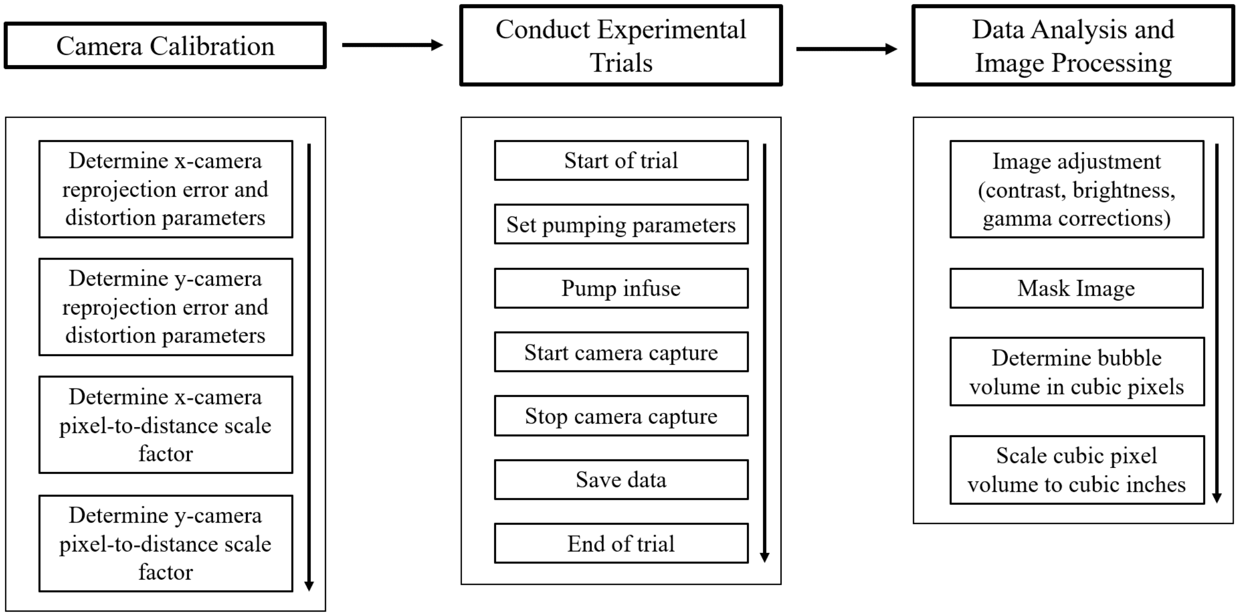

Figure 5.10: Flowchart of the experimental procedures followed during a typical set of experimental trials.

distances to be obtained from pixel measurements. Before any experiments were conducted, the imaging system had to be calibrated to obtain accurate measurements of the bubble. A camera calibration was conducted each day data was to be collected. The calibration of the imaging system could be conducted by either one or two operators.

The two-dimensional camera calibration method, originally developed by Zhang, was used to calibrate the experimental platform [109]. While other calibration methods exist, such as one-dimensional or three-dimensional calibrations, the two-dimensional method selected is one of the most robust and computationally efficient [110, 111]. The calibration code was written in Python, using the OpenCV computer vision library. The two-dimensional calibration object chosen was a black-and-white, square checkerboard pattern (shown in Figure 5.11). To calibrate, the fluid chamber was filled with water and the checkerboard was placed in the water on top of the orifice. This step ensured that, just as in the experimental trials, the cameras were being calibrated through the polycarbonate fluid chamber walls and water in the fluid chamber. In other words, the index of refraction through the water and fluid chamber was the same during the calibration and experimental trials. The x-axis camera and y-axis camera were then verified to be orthogonal to each other and level, using a square and high-precision levels, respectively. The two cameras were then focused on the checkerboard. After focusing, between 25 and 50 images were taken of the checkerboard with each camera.

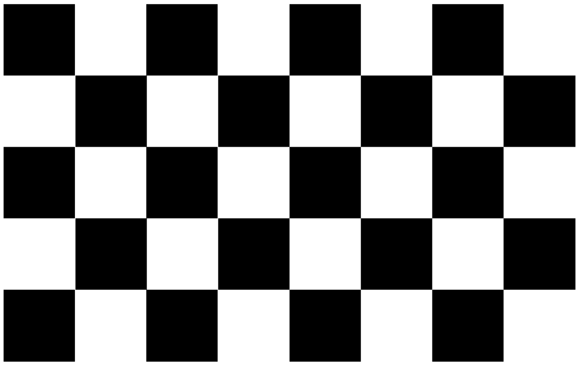

Figure 5.11: Two-dimensional 8 by 5 checkerboard used to calibrate the imaging system.

After checkerboard images were obtained, the Python script was run to determine the distortion parameters and reprojection error. In general, camera systems have two types of distortion: extrinsic and intrinsic distortion [109]. Extrinsic distortion occurs outside of the lens-camera system, while intrinsic distortion occurs inside the lens-camera system [1]. Both distortions can be modeled linearly as radial and tangential distortions [112]. The *calibrateCamera* function, used in this method, uses a least-squares method for approximating the intrinsic and extrinsic distortion parameters. To determine if the distortion parameters had been modeled accurately, the reprojection error was used as a diagnostic [1]. The reprojection error, which is the geometric error for a projected point on an image versus its measured point, is a great measure for calibration accuracy [1]. The most accurate calibrations have a reprojection error close to zero. As found by Varnum-Lowry, the maximum acceptable reprojection error for this experiment was 0.220 [1]. Thus, checkerboard images were collected during camera calibration until the reprojection error was below 0.220.

Using the distortion parameters to undistort an image was the first stage of the calibration process. Next, a scale factor had to be determined. A scale factor allows for real, physical distances to be obtained from pixel measurements within an image. This allowed for the accurate measurement of physical properties of the bubble, such as volume or bubble diameter. To determine the scale factor, a reference object of a known size was chosen and imaged. During all calibrations of the imaging system, a 0.5-inch 440C stainless-steel ball with a tolerance of 0.0001-inch was used. The ball was placed on the orifice and imaged with each camera. The image of the ball was then undistorted using the previously determined distortion parameters. Using computer vision algorithms, the ball's volume was calculated in cubic pixels. The scale factor for each camera was then determined by dividing the pixel volume by the reference object's known volume. After determination of the scale factor, the imaging system was then said to be calibrated. The cameras and fluid chamber then remained fixed in their respective locations until a new calibration was conducted.

5.3.2 Experimental Trials

After the imaging system was properly calibrated, experimental trials were conducted. Experimental trials could be conducted by a single experimental operator. To start the trial, the orifice plate was cleaned with isopropyl alcohol, rinsed with distilled water, and left to air dry. After cleaning, the fluid chamber was assembled and connected to the gas injection system via Luer Lock connectors and filled with 6 cm of distilled water. The room air temperature, relative humidity, and water temperature were then all recorded.

The next step was to set all pumping parameters within the Python execution code. The parameters to be set included the constant volumetric flow rate and the total volume pumped. Since each trial was to only analyze a single bubble, the pumping was stopped after a total pump volume of approximately two to three times the expected bubble volume. After setting all pumping parameters, the Python script was executed and the pump started to infuse the gas through the orifice at the specified constant volumetric flow rate. Once the pumping started, the high-speed cameras were triggered and started capturing image frames in order to image bubble formation, growth, and detachment. For all experimental trials, the imaging system was triggered after the first bubble detachment in order to capture the *second* bubble to detach within a pumping cycle. Immediately following bubble detachment, the cameras were commanded by the experimental operator to stop image capture. All individual frames were then saved to file folders. A typical camera capture contains approximately 2,000 frames over two seconds of image capture. The process described above constitutes a single bubble formation and detachment trial. The same process was then repeated for each trial as variables, such as orifice plate material or flow rate, were varied.

5.3.3 Image Processing

As discussed in the Contributors Section, the image analysis code and methodology was originally developed and written in collaboration with Master of Science Student Daniel Varnum-Lowry. Methodology and results of this development were published in Varnum-Lowry's thesis [1]. The primary purpose of image processing, or image analysis, was to determine the bubble's volume. The image processing included three stages: image adjustment, masking, and volume measurement.

5.3.3.1 Image Adjustment

After collecting image frames from an experimental trial and before any computer vision algorithms could process the video frames, the image clarity had to be improved. The operator chose a set of frames from an experimental trial to process. First, all frames were undistorted, using the distortion parameters found during camera calibration. Using a video editing software, the frame number of the bubble detachment frame was determined and recorded. Then, using the bubble detachment frame, the operator would adjust the image contrast, brightness, and gamma. This was a manual, trial and error process until a clear image with a dark bubble and white background behind the bubble was obtained. The same contrast, brightness, and gamma corrections were then applied to every single frame within the experimental trial. An example of an adjusted image can be viewed in Figure 5.13.

In a black and white image, the pixels within an image make up a matrix with cell values ranging from 0 to 255, where 0 is black and 255 is pure white. Brightness and contrast adjust these pixel values according to Equation 5.3, where $\boldsymbol{f(i,j)}$ is the input pixel values, β is the brightness, Ψ is the contrast, and $\boldsymbol{g(i,j)}$ is the output pixel values [1]. Gamma correction adjusts the pixel values according to Equation 5.4, where I_{in} is an input image, γ is the gamma value, and I_{out} is the output image. I_{out} is subsequently scaled back to values between 0 and 255 [1].

$$\boldsymbol{g(i,j)} = \Psi \boldsymbol{f(i,j)} + \beta \tag{5.3}$$

$$I_{out} = \left(\frac{I_{in}}{255}\right)^{\gamma} * 255 \tag{5.4}$$

Once the image was properly adjusted to achieve the clearest image possible, the image was cropped. The operator manually cropped the image by selecting a region of interest around the bubble. This ensured that the bubble was centered and any unnecessary features, such as the orifice plate, were eliminated. An example of a cropped, adjusted image is shown in Figure 5.13.

5.3.3.2 Image Masking

The last step before bubble volume measurement was masking of the image. The process of masking was automated by using functions within the Python OpenCV library. Figure 5.12 shows the steps of image processing, including image adjustment and masking. After cropping the image to the specified region of interest, the image was converted from a grayscale image [0-255] to a purely black and white image [0, 255], often referred to as a binary image. This means that the only pixel values were 0 and 255. This was performed automatically in OpenCV via a threshold command, which sets all pixel values above and below a threshold value to 255 and 0, respectively. After thresholding the image, the contiguous background behind the bubble was flood filled with white pixels. Only the bubble interior remained after the flood fill. The next step inverted all pixels, making all black pixels white and all white pixels black. Next, a *bitwise OR* function was used to combine the threshold image and the inverted image. The *bitwise OR* function compares two images of the same size. The function sets an output pixel to white if the pixel was white in either image, otherwise the output pixel is set to black. The final step was noise reduction, using the open and close functions within OpenCV. The final image was then considered masked and ready for bubble volume measurement. Figure 5.13 shows the process of image adjustment, cropping, and masking on an example experimental trial conducted on polycarbonate.

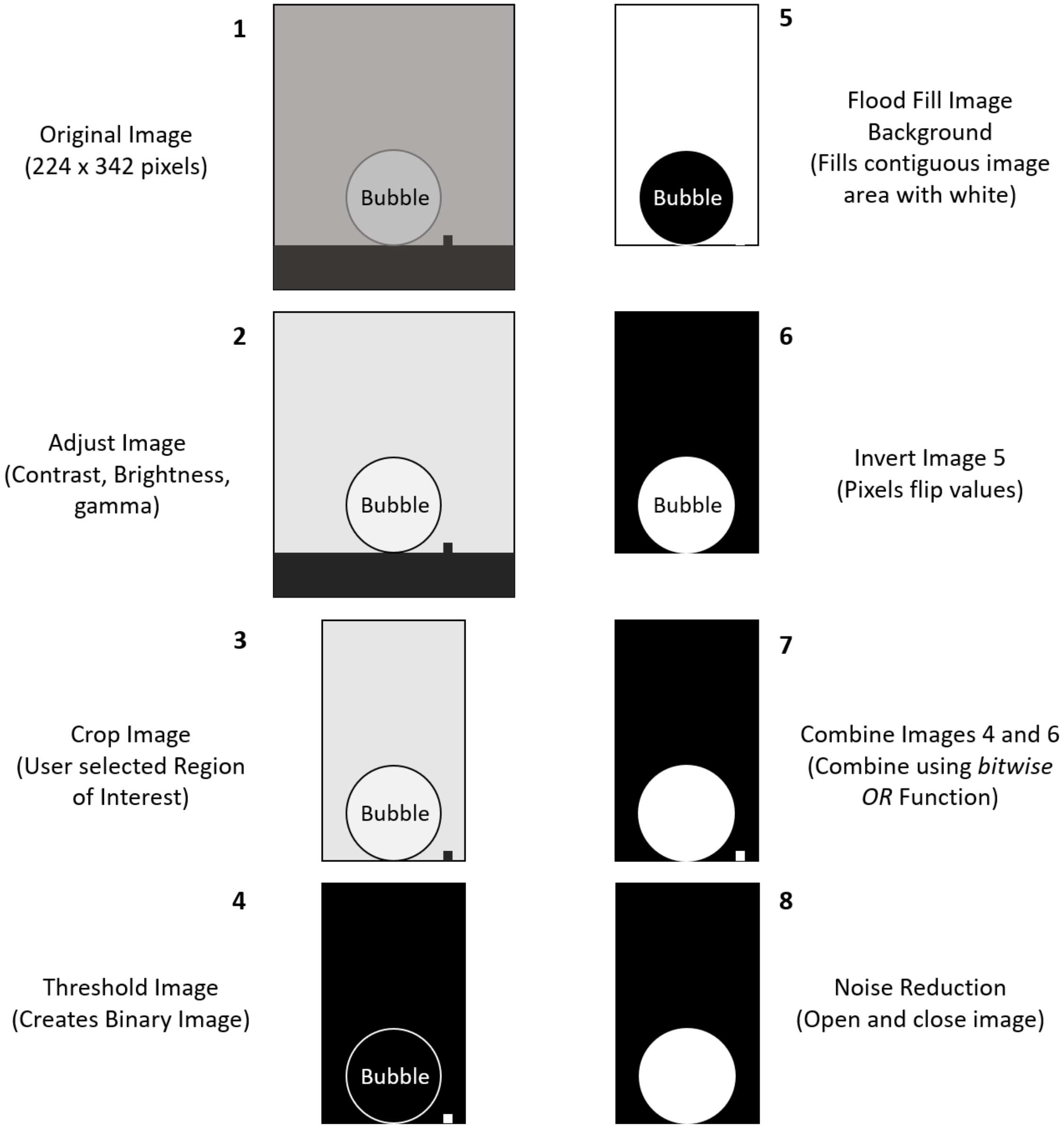

Figure 5.12: Image processing steps using the Python OpenCV library.

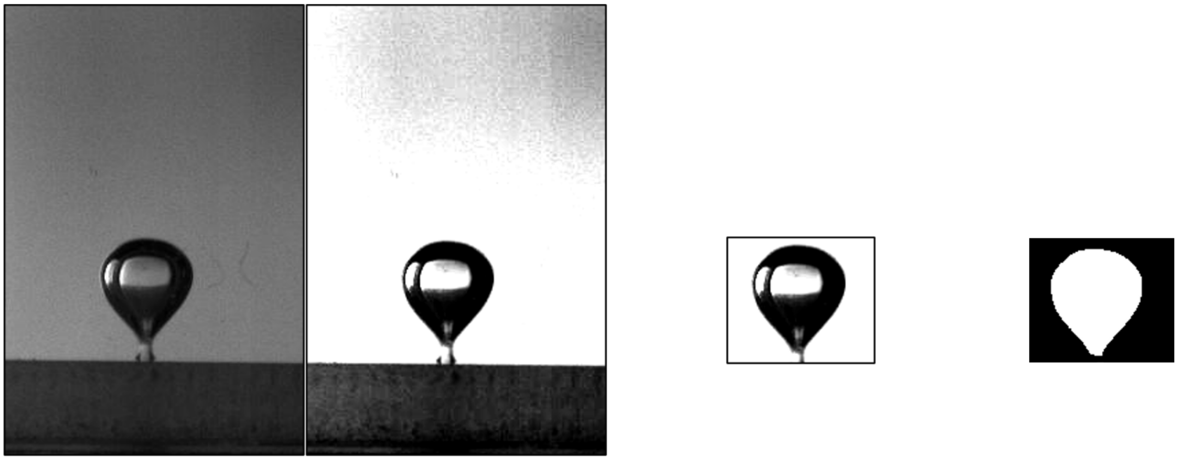

Original Image Adjusted Image Cropped, Adjusted Image Masked Image

Figure 5.13: Example bubble detachment frame showing the process of image adjustment, cropping, and masking.

5.3.3.3 Bubble Volume Measurement

The measurement of bubble volume used the masked image produced from the prior stage of image processing and the scale factor determined during camera calibration. Before any measurement was performed, the bubble detachment frame was determined. The bubble detachment frame was considered to the last frame which contained a visible bubble neck. Figure 5.14 shows the determination of a bubble detachment frame. All subsequent analysis took place on the bubble detachment frame.

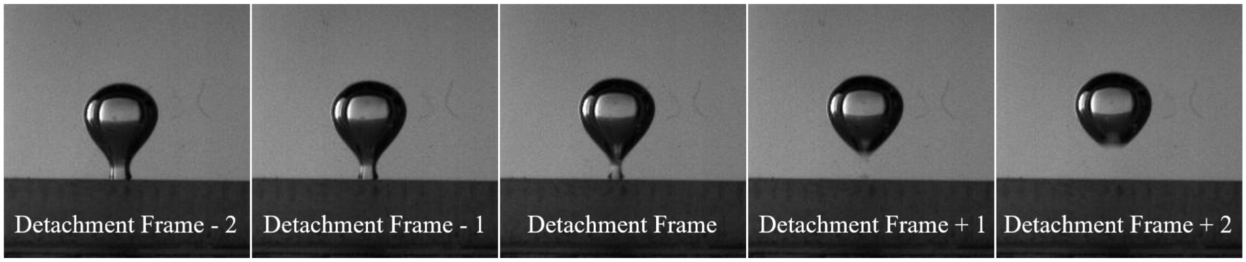

Figure 5.14: Determination of the bubble detachment frame.

The bubble volume measurement in this research assumes an axisymmetric bubble. This can be justified through experimental observation. Various bubble volume measurements, including those which did not make an axisymmetric assumption, were explored by Varnum-Lowry [1]. Varnum-Lowry found that no significance difference exists between axisymmetric and non-axisymmetric volume measurement techniques for this specific bubble formation experiment [1]. The masked image was analyzed using the OpenCV equivalent spherical diameter (ESD) function. The *ESD* function reads in a closed shape (in this case the bubble outline) and outputs the diameter of a sphere with the same cross-sectional area as the shape. Using this diameter, a bubble volume was calculated according to Equation 5.5. Then, using the scale factor determined in the camera calibration phase, the bubble volume was converted from cubic pixels to microliters. This process was performed for the x-axis and y-axis cameras. The two bubble volumes were then averaged. By using precise image system calibrations, the x-axis and y-axis volume measurements typically differed by less than 0.4 μL.

$$V_b = \frac{1}{6}\pi(d_b)^3 \tag{5.5}$$

5.4 Experimental Variables

5.4.1 Materials

Four materials were used for the orifice plates in the experimental research: quartz glass, polycarbonate, 304 stainless steel, and aluminum 6061. The selection of these materials was intentional. First, these materials span the three material classes: metals, polymers, and ceramics. Secondly, these materials are commonly used in spaceflight systems. Quartz and polycarbonate are common materials for viewing windows of microgravity fluid experiments. Aluminum 6061 is commonly used in aircraft and spacecraft structures. Finally, 304 stainless steel is used in various components of the ISS environmental control and life support systems (ECLSS) and the portable life support system (PLSS) of the extravehicular mobility unit (EMU) [113–116].

5.4.2 Gas Injection Rates

To satisfy research objectives 2 and 4, a 1 g experimental gas injection study was conducted. The purpose of the gas injection study was two-fold. First, the study aimed to find the gas injection rate, below which, bubble detachment volume remained constant. This would ensure that all jetting effects caused by the kinetic force of gas injection, drag caused by bubble expansion, and the inertial force of the hydrostatic pressure during bubble expansion were all negligible. The experimental gas injection study also served to provide data to validate 1 g CFD models.

In all experimental trials, the gas and liquid used were room air and distilled water, respectively. The only variable for each orifice plate was the rate at which gas was injected through the orifice. On each of the four orifice plate materials, the gas injection rate was varied from 7 μL/s to 100 μL/s. The following gas injection rates were tested on each material: 7, 10, 12.5, 17, 20, 25, 27.5, 30, 35, 50, and 100 μL/s. For each orifice plate and gas injection rate combination, 15 trials were conducted. A summary of the experimental gas injection study variables is shown in Table 5.2.

The dependent variable measured in the gas injection study was the bubble volume at detachment. Water temperature, room air temperature, and relative humidity were also recorded as independent variables. These measurements were used when specifying boundary conditions and fluid properties in the CFD models.

Table 5.2: Experimental gas injection study variables

Orifice Plate Material	**Constant Flow Rate (μL/s)**	**Number of Trials (N)**
Quartz, Polycarbonate, 304 Stainless Steel, Aluminum 6061	7	15
Quartz, Polycarbonate, 304 Stainless Steel, Aluminum 6061	10	15
Quartz, Polycarbonate, 304 Stainless Steel, Aluminum 6061	12.5	15
Quartz, Polycarbonate, 304 Stainless Steel, Aluminum 6061	17	15
Quartz, Polycarbonate, 304 Stainless Steel, Aluminum 6061	20	15
Quartz, Polycarbonate, 304 Stainless Steel, Aluminum 6061	25	15
Quartz, Polycarbonate, 304 Stainless Steel, Aluminum 6061	27.5	15
Quartz, Polycarbonate, 304 Stainless Steel, Aluminum 6061	30	15
Quartz, Polycarbonate, 304 Stainless Steel, Aluminum 6061	35	15
Quartz, Polycarbonate, 304 Stainless Steel, Aluminum 6061	50	15
Quartz, Polycarbonate, 304 Stainless Steel, Aluminum 6061	100	15

6. COMPUTATIONAL FLUID DYNAMIC (CFD) MODELING METHODOLOGY

A Computational Fluid Dynamic (CFD) model was developed to model gas bubble formation, growth, and detachment from an orifice submerged in a liquid. This section presents the solver, geometry, boundary conditions, mesh generation and refinement, parallelization, and computational efficiency of the CFD model. The variables tested with the CFD model will subsequently be presented.

6.1 CFD Solver

The case of a gas bubble forming and detaching within a liquid is within a category of multiphase flows known as an interfacial flows. Interfacial flows are those which include two or more immiscible fluids separated by a distinct interface [36]. A free surface is the interface between a gas and the other fluid (in this case a liquid) with which it is in contact. In other words, a free boundary is a surface on which discontinuities exist in a variable [117]. In the case of gas bubbles in a liquid, multiple variables, specifically fluid properties, experience discontinuities across the phase interface. In order to accurately resolve the phase front between a gas bubble and a liquid, the location of the free surface must be tracked by the CFD solver. This tracking is typically done by interface tracking methods [36]. Interface tracking allows for the variables': (1) discrete representation, (2) evolution in time, and (3) proper implementation of boundary conditions across phase boundaries [117]. Different CFD solvers handle interface tracking in various ways. Level set method, volume of fluid (VOF) method, and Lagrangian particle tracking are all valid ways to track the free surface of a fluid in finite-difference numerical simulations [36, 93].

For the present research, a volume of fluid solver was chosen. Of all interface tracking methods, the VOF method is the simplest method and, on average, increases the computational efficiency of the simulation. In general, the level set method is less computationally efficient than VOF. While Lagrangian methods are typically efficient methods to track a free surface, they do not handle fluid separation, such as bubble detachment, well without fluid element deformation. For these reasons, a volume of fluid solver was the best for this application. The VOF method is described as follows [117]. Suppose a function G is defined as one at a point which contains a fluid and zero otherwise. In the case of a CFD mesh, G would be defined as equal to one in a cell which contains the fluid and zero in a cell which was empty of the fluid. In all cells which contain a free surface, G would have a value between zero and one [117]. This allows the simulation to identify and track the free surface while storing minimal information (only cells which have a G value between zero and one). Then, by taking the derivative of G, a surface normal could be found which can then indicate a general direction and location of the free surface [117]. G evolves in time and space via Equation 6.1.

$$\frac{\partial G}{\partial t} + u\frac{\partial G}{\partial x} + v\frac{\partial G}{\partial y} + w\frac{\partial G}{\partial z} = 0 \tag{6.1}$$

As mentioned, a volume of fluid tracking method allows for the efficient tracking of free surfaces within a numerical model and eliminates logical problems involved with tracking intersecting surfaces rather than regions [117]. The VOF method is simply used to track the fluid free surface while the Navier-Stokes equations are solved separately.

The specific volume of fluid solver chosen was OpenFOAM's InterFoam solver. InterFoam is a multiphase, transient, incompressible, isothermal, immiscible volume of fluid solver. InterFoam was chosen to model the bubble formation and detachment experiment for the following reasons. First, the experiment uses standard sea-level air injected into distilled water. These fluids can be assumed to be an immiscible, two-phase fluid system. The gas velocities through the orifice are on the order of 1-30 mm/s and a primary goal of the experiment and model was to minimize any jetting effects by minimizing injection rates. It is therefore reasonable to assume the incompressibility of the air and water. The experiment was controlled to ensure that the gas, liquid, and fluid chamber walls are at the same room temperature during all experimental trials. Thus, InterFoam's isothermal assumption applies. Finally, InterFoam, like many other OpenFOAM solvers, allow for the modification of Sessile drop contact angle boundary conditions on the walls. As presented later, the orifice plate's equilibrium contact angle will be a critical variable tested in this research.

InterFoam's constant-density continuity and momentum equations are presented in Equation 6.2, and Equation 6.3, respectively [118].

$$\frac{\partial u_j}{\partial x_j} = 0 \tag{6.2}$$

$$\frac{\partial(\rho u_i)}{\partial t} + \frac{\partial}{\partial x_j}(\rho u_j u_i) = -\frac{\partial p}{\partial x_i} + \frac{\partial}{\partial x_j}(\tau_{ij} + \tau_{t_{ij}}) + \rho g_i + f_{\sigma i} \tag{6.3}$$

The density is defined by Equation 6.4, where α is the phase fraction.

$$\rho = \alpha\rho_1 + (1-\alpha)\rho_2 \tag{6.4}$$

The source terms in the momentum equation are the gravity body force and surface tension. The surface tension is defined by Equation 6.5 and is modeled as a continuum surface force [119].

$$f_{\sigma i} = \sigma\kappa\frac{\partial\alpha}{\partial x_i} \tag{6.5}$$

The curvature, κ, is defined by Equation 6.6.

$$\kappa = -\frac{\partial n_i}{\partial x_i} = -\frac{\partial}{\partial x_i}\left(\frac{\partial\alpha/\partial x_i}{|\partial\alpha/\partial x_i|}\right) \tag{6.6}$$

The interphase equation in Equation 6.7 is the free surface tracking equation which accounts for the location of the phase front between the fluids.

$$\frac{\partial\alpha}{\partial t} + \frac{\partial(\alpha u_j)}{\partial x_j} = 0 \tag{6.7}$$

6.2 CFD Case Parameters

When setting up each case directory, certain control parameters were common across all CFD cases. All models had a start time of $t = 0$. The maximum allowable timestep was 0.01 seconds. However, all models were run with an adjustable timestep scheme, which adjusts the timestep to keep the Courant number below one. The Courant number is a dimensionless number and serves as a condition for convergence when solving the Navier-Stokes equations by numerical analysis. Equation 6.8 shows the equation for the Courant number and the condition that it must be below a maximum value, chosen to be one in this case. Once the length interval (mesh size) and velocity magnitude are set, the timestep must be decreased to satisfy the Courant condition. Typical timesteps experienced by the model were on the order of 10^{-6} - 10^{-7} seconds. Finally, the write interval, the interval at which data is written to the results, was specified as 0.05 seconds.

$$C = \frac{u\Delta t}{\Delta x} \tag{6.8}$$

6.3 Model Geometry

The CFD model's geometry closely approximates the geometry of the physical experimental setup. Gmsh, a mesh and geometry creation software, was used to create the model's geometry. The model is axisymmetric about the z-axis, which is the center axis of the orifice. The assumption of symmetry is justified by experimental observation. OpenFOAM requires that all axisymmetric models be a wedge which is a single cell in thickness. OpenFOAM also requires that the wedge straddles a coordinate plane. Thus, the geometry created for this model is a 5° wedge centered along the z-axis and straddling the $x - y$ coordinate plane. The geometry of the model is presented in Figure 6.1.

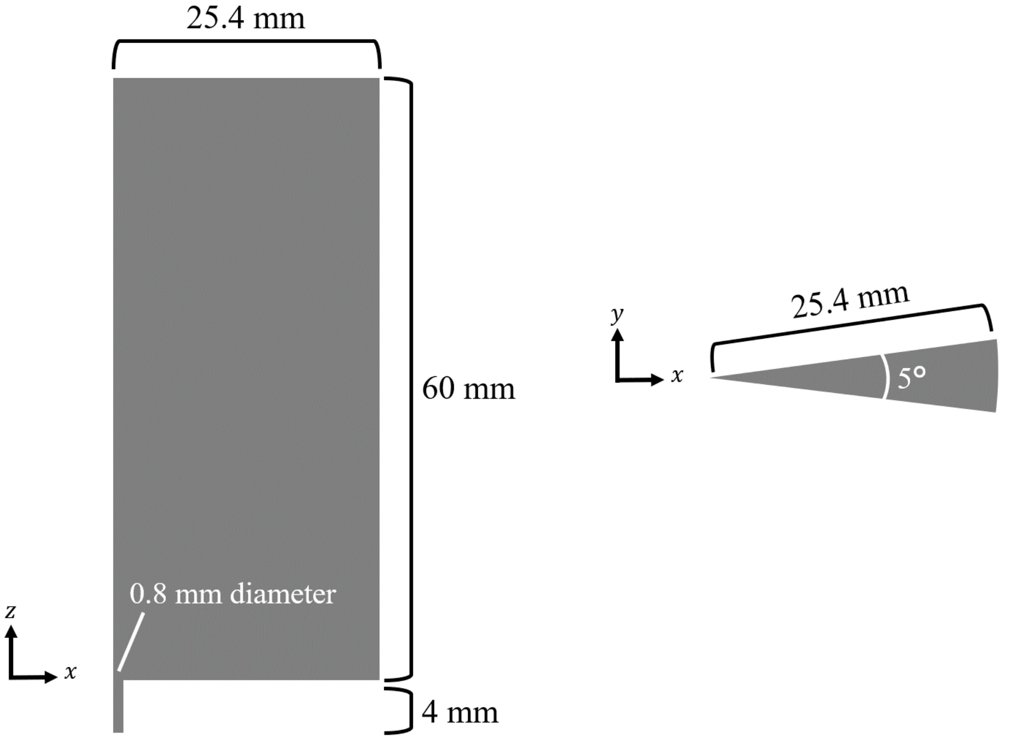

Figure 6.1: Geometry and dimensions of the CFD model, consisting of a 5° wedge.

The dimensions of the model closely follow the experimental fluid chamber dimensions. Just as in the experimental setup, the orifice is 0.8 mm in diameter. Leading into the orifice is a 4 mm long pipe drilled into the orifice plate. The source of gas injection is the inlet at the bottom of the pipe. The fluid chamber is assumed to be a 60 mm tall cylinder with a diameter of 50.8 mm, or two inches. The orifice plate, containing the orifice, is the bottom wall of the fluid chamber. The fluid chamber shape is the sole deviation from the experimental setup. The experimental fluid chamber is actually a 60 mm tall by 50.8 mm wide *square* cylinder. This assumption was made for the purposes of creating an axisymmetric model. The assumption of a round fluid chamber is justified by making the chamber walls wide enough as to eliminate any wall effects. Albadawi states that walls effects can be neglected if the fluid chamber is at least five times as wide as the bubble radius [93]. The 1 g bubble radii produced by the experiment and CFD were no larger than 2.1 mm. So, a fluid chamber with a radius of more than ten times the bubble radius was reasonably assumed to eliminate all wall effects. Lastly, the CFD model's geometry does not include a circular vent in the top wall of the fluid chamber as the experimental fluid chamber does. As will be discussed as part of the model's boundary conditions, the entire top of the fluid chamber will be modeled as a vent to atmosphere.

6.4 Boundary and Initial Conditions

As discussed in Section 6.3, to model the bubble formation experiment as axisymmetric, a 5° wedge with a single cell thickness in the θ-direction was created. The model consists of seven parts, all labeled in Figure 6.2: outlet, inlet, fluid chamber walls, orifice plate, pipe, wedge front, and wedge back. All parts of the model assume isothermal boundary conditions. The front and back wedge faces use the *wedge* type boundary condition. The *wedge* boundary condition is unique to OpenFOAM and ensures that the model is axisymmetric. As Figure 6.3 shows, the front and back patches of the same cell within the wedge are equal to one another and thus creates an axisymmetric boundary condition.

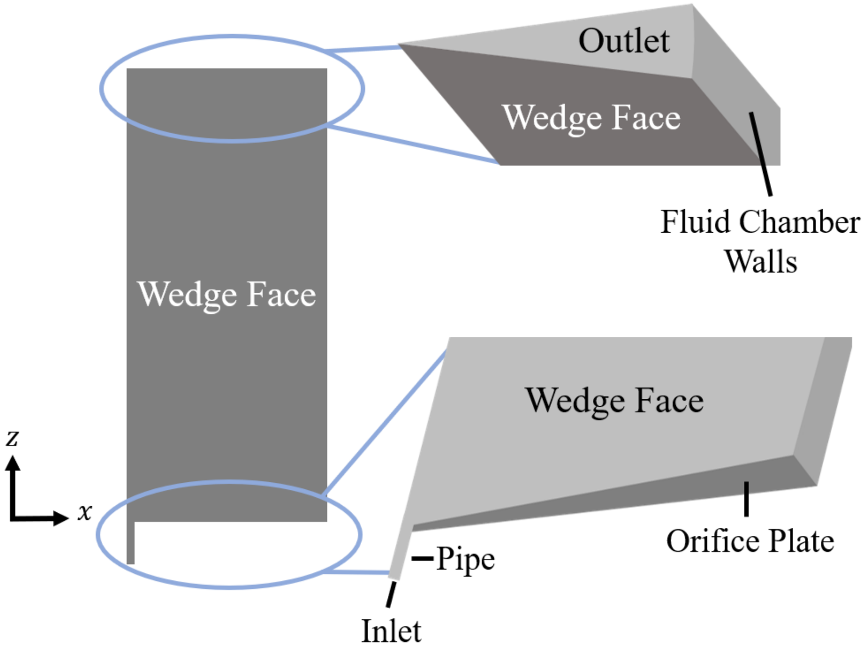

Figure 6.2: Labeled diagram of all parts of the model, including the inlet, outlet, wedge faces, fluid chamber walls, pipe, and orifice plate.

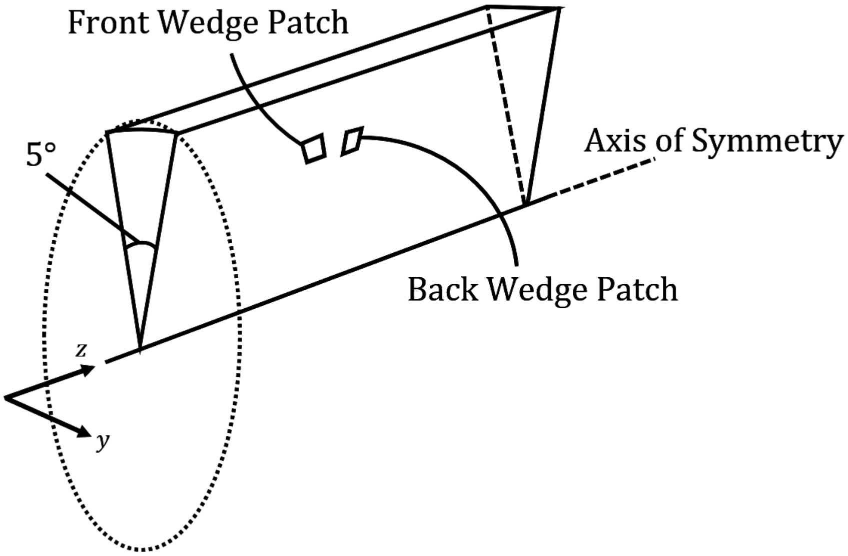

Figure 6.3: Schematic of the axisymmetric nature of the wedge geometry.

The fluid chamber is modeled as a wall with boundary conditions of fixed flux pressure and no slip. To model polycarbonate walls, the fluid chamber was also given a constant contact angle of $73.06°$, which was the average equilibrium contact angle for polycarbonate, as measured on the experimental fluid chamber by the goniometer and displayed in Table 5.1. The constant contact angle boundary condition only requires the measured equilibrium contact angle, unlike dynamic contact angle boundary conditions, which require measurements of the advancing contact angle, receding contact angle, contact angle rate of change. Many previous works suggest the use of the constant contact angle boundary condition [93]. The pipe and orifice plate were also modeled as walls with imposed boundary conditions of fixed flux pressure and no slip. Similar to the fluid chamber walls, the pipe and orifice plate were given a constant contact angle boundary condition. The value of the contact angle is dependent upon the material being studied: quartz, polycarbonate, stainless steel, or aluminum. The average contact angles measured by the goniometer and presented in Table 6.1 were used. The outlet was given a zero-gradient pressure boundary condition, to model a free fluid surface open to the ambient atmosphere. The inlet was given a constant, uniform velocity along the positive z-axis. The specific value of the inlet velocity was varied, as discussed in Section 6.9.3.

Table 6.1: Equilibrium Sessile drop contact angles used for the orifice plate CFD boundary conditions

Orifice Plate Material	**Orifice Plate Constant Contact Angle Boundary Condition (Degrees)**
Quartz	46.24
Polycarbonate	73.06
304 Stainless Steel	80.35
Aluminum 6061	77.38

Initial conditions were also set. At the first timestep, $t = 0$, the constant, uniform velocity at the inlet was started. The initial air and water fields were set such that at the first timestep, air entirely filled the pipe up to the level of the orifice plate. Water filled the entire fluid chamber above the orifice plate.

6.5 Physical Properties

As with any modeling effort, the physical properties of the fluids and materials had to be set. The physical properties were either taken from the literature, or measured experimentally. Table 6.2 displays all of the physical properties taken from the literature. When determining fluid properties, it was assumed that all experimental trials were conducted at sea level and with dry, sea-level air composed of 78.09% nitrogen, 20.95% oxygen, 0.92% argon, 0.035% carbon dioxide, and small traces of other gases [120]. The room temperature of all fluids was measured experimentally in the lab and had a range from $23.5°$C to $26°$C, depending on the day the experimental trial was conducted. For the purposes of the CFD model, a constant room temperature of $25°$C was assumed.

The measured physical properties included the Sessile drop contact angles of water droplets on each orifice plate. The methodology of collecting these measurements are described in Section 5.2. For the CFD model, the constant contact angle boundary condition on each orifice plate was taken to be the average experimental contact angle. For completeness, the table which summarizes the contact angle for each orifice plate is repeated in Table 6.3.

Table 6.2: Values of all physical properties used in CFD models

Physical Property	Value
Acceleration due to Gravity on Earth	$9.81\ m/s^2$
Temperature as measured in lab	25°C
Surface Tension Between Water and Air [121]	$0.0720\ N/m$
Air Density [122]	$1.184\ kg/m^3$
Water Density [121]	$997\ kg/m^3$
Kinematic Viscosity of Air [122]	$15.62 * 10^{-6}\ m^2/s$
Kinematic Viscosity of Water [121]	$0.893 * 10^{-6}\ m^2/s$

Table 6.3: Equilibrium contact angles used for the orifice plate CFD boundary conditions

Orifice Plate Material	Measured Sessile Drop Contact Angle (Degrees)	Standard Deviation (Degrees)	Calculated Surface Energy (mJ/m^2)	Published Surface Energy (mJ/m^2)
Quartz	46.24	5.75	51.67	30 - 76 [105]
Polycarbonate	73.06	0.91	41.48	34 - 50 [106]
304 Stainless Steel	80.35	1.69	25.79	25.5 - 30.7 [107]
Aluminum 6061	77.38	1.86	27.25	23.2 - 33.1 [104, 108]

6.6 Mesh Generation and Refinement

After creation of the model's axisymmetric wedge geometry, the mesh was then generated. Gmsh, the program used to create the model's geometry, was also used for mesh generation. For the entirety of the model, a structured mesh was used. Structured meshes are characterized by regular connectivity and when compared to their unstructured counterparts, structured meshes are more space efficient and offer higher resolution [123]. The mesh primarily consists of hexahedral cells with prismatic cells along the axis of symmetry.

The scope of the CFD research was focused on bubble formation, growth, and detachment. The bubble's interaction with the orifice plate was a top priority which required heavy mesh refinement. Bubble rise dynamics and flow away from the orifice, which were not in the scope of the CFD study, therefore, required less mesh refinement. To increase computational efficiency and resolution near the orifice, a selective mesh refinement scheme was implemented. Figure 6.4 shows the scheme of this selective mesh refinement. Regions of interest were used to concentrate mesh refinement near the orifice, where the bubble would growth and detach. The mesh becomes progressively less refined away from the orifice near the fluid chamber walls and outlet. Bubble growth and detachment entirely takes place within the region of highest mesh refinement.

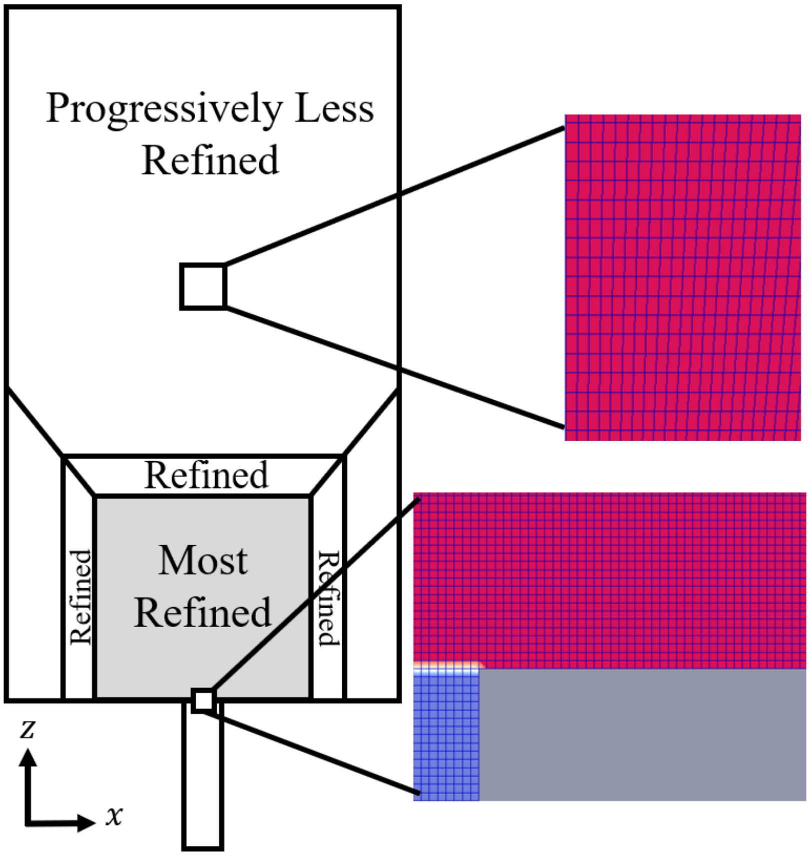

Figure 6.4: Mesh refinement scheme, showing the most refined mesh region near the orifice and progressively less refined mesh away from the orifice.

After mesh generation, a mesh refinement study was conducted to verify mesh independence, while maximizing computational efficiency. In 3D modeling, insufficient spatial resolution of the mesh can lead to inaccuracies in parameters, such as local velocity and wall shear stress [124]. The CFD literature advocates for the demonstration of mesh independence as a necessary condition for the validity of a computational model [124–126]. However, while increasing the mesh refinement eliminates inaccuracies caused by coarser meshes, it will also increase the computational cost. A critical value of mesh refinement must be determined: one which achieves mesh independence, but also minimizes computational cost. In general, a mesh independence study is conducted to find the critical level of mesh resolution, such that, as the mesh is further refined beyond the critical value, key parameters remain constant. When applied to the bubble formation CFD model, this means that mesh independence is achieved when the bubble volume at detachment remains constant, even after additional mesh refinement.

Seven mesh versions were created as part of the mesh refinement study. The number of cells in each mesh ranged from 34,000 to 175,000. Across all meshes, the *ratio* of cells in each mesh refinement region remained constant. The number of cells in each refinement region were simply scaled by the same linear factor. A standard bubble detachment trial was run on each mesh, with the number of cells being the only variable. The mesh was considered independent when the increase of cells varied a critical parameter, in this case the bubble detachment volume, by no more than 2.25%. Mesh independence was achieved with mesh version 5, containing 138,360 cells. Figure 6.5 shows the graph of mesh independence. As shown, bubble detachment volume begins to level off with mesh version 5.

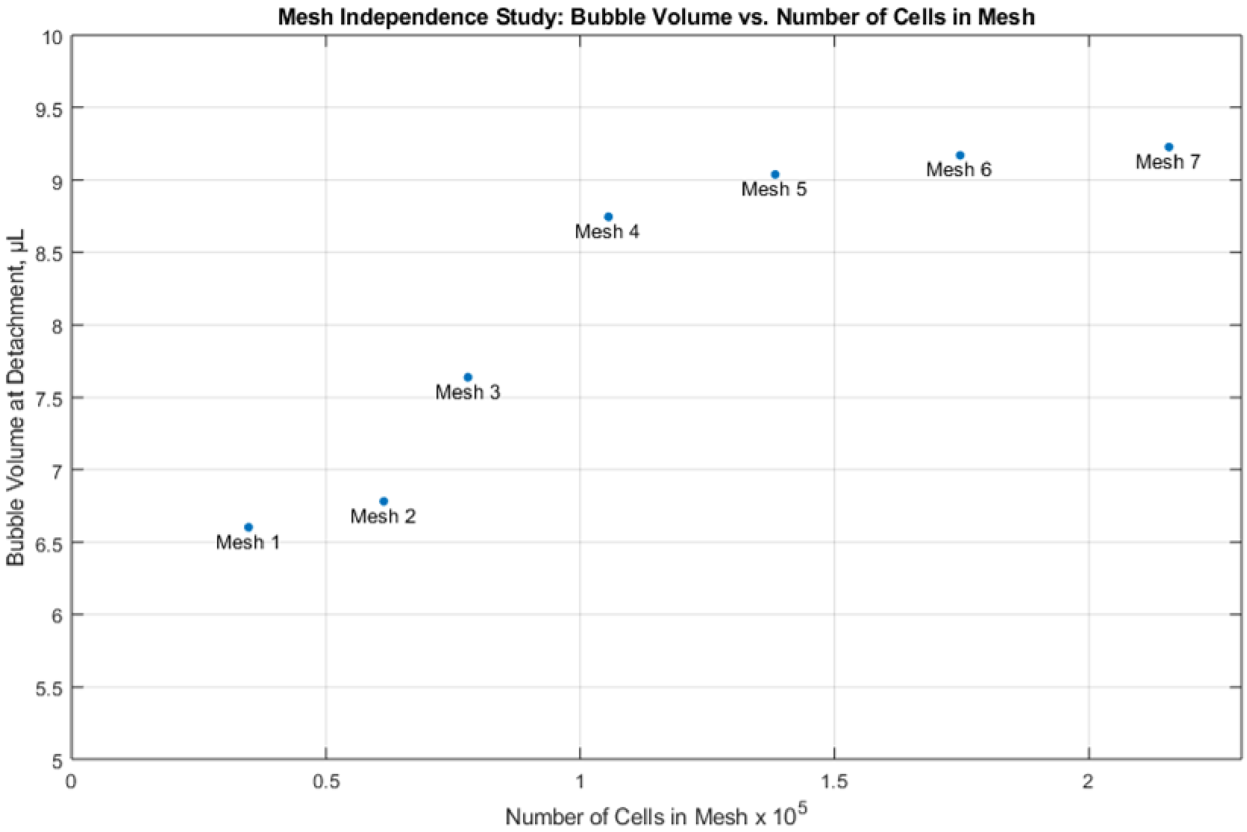

Figure 6.5: Graph of bubble detachment volume versus number of cells in the mesh. Mesh independence is achieved by mesh version 5 with 138,360 cells.

Table 6.4 presents a detailed report of the mesh refinement study. The mesh scale factor and bubble detachment volume are each normalized to mesh version 5, the chosen mesh. Mesh 5 greatly reduces the computational cost, when compared to mesh versions 6 and 7, without significant difference in bubble detachment volume. For all subsequent modeling efforts, mesh version 5 was used.

6.7 Computational Efficiency and Parallelization of the CFD Model

The computation of all CFD models in this dissertation took place on the Ada cluster of the Texas A&M High Performance Research Computing (HPRC) Group. When running a model across multiple cores, the model is decomposed into subdomains, enabling the parallelization of their computation. The efficiency of a model is typically measured by the CPU time and clock

Table 6.4: Data collected during the mesh independence study. In order to maximize efficiency while still achieving mesh independence, mesh version 5 was chosen.

Mesh Version	**Number of Cells**	**Mesh Scale Factor from Mesh Version 5**	**Clock Time per Second of Model Time (Hours)**	**Bubble Volume (μL)**	**Bubble Volume Percent Difference from Mesh Version 5**
1	34,810	0.25	3.82	6.60	31.18%
2	61,372	0.44	2.96	6.78	28.53%
3	77,910	0.56	3.44	7.64	16.81%
4	105,514	0.76	4.51	8.75	3.28%
5	138,360	1	6.85	9.04	0.00%
6	174,698	1.26	13.07	9.17	1.43%
7	215,775	1.56	18.55	9.23	2.05%

time. Clock time is the total amount of time, as measured by a standard watch or wall clock, it took for the completion of the model. The CPU time is the clock time multiplied by the number of CPUs, which equals the number of subdomains in the model. Since high performance computing time is typically charged by CPU time, the goal of a decomposition study is to minimize the CPU time.

The method of the model's decomposition can be modified in various ways. The *number* of subdomains can be increased or decreased. The orientation of the subdomains can also be varied. To demonstrate this concept, Figure 6.6 displays two different methods to distribute four subdomains across a two-dimensional square grid. Four subdomains can be applied in the y-direction, or two subdomains can be applied in both the x-direction and y-direction. The product of these decomposition coefficients must always equal the total number of subdomains.

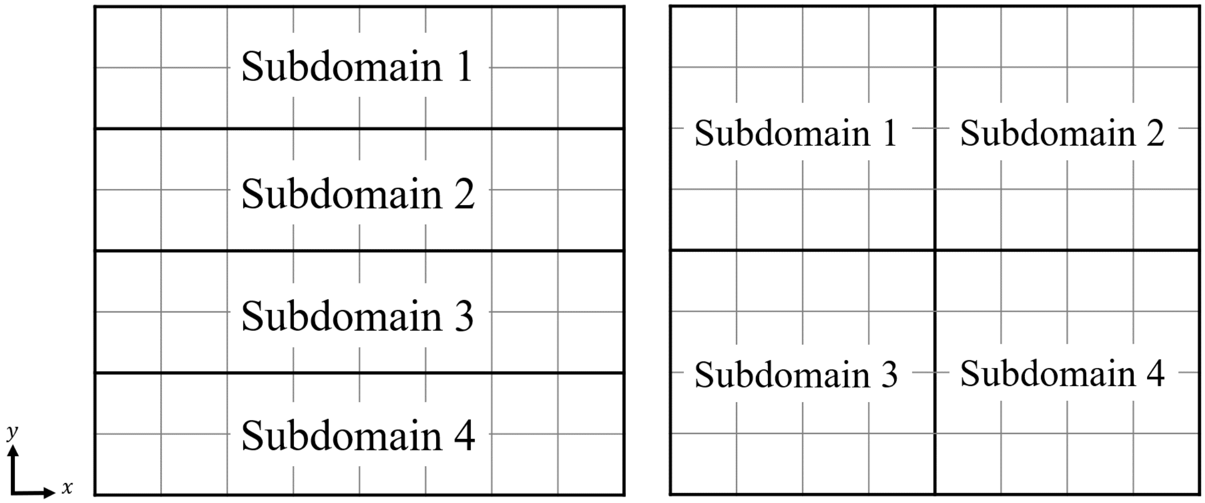

Figure 6.6: Four-subdomain decomposition methods of a two-dimensional square. On the left, the decomposition coefficients are $x = 1$ and $y = 4$. The right shows a decomposition method with coefficients of $x = 2$ and $y = 2$.

A decomposition study was conducted on the model to maximize computational efficiency. Similar to the mesh independence study, the only variables in this study were the number of subdomains and their corresponding decomposition coefficients. Using a simple decomposition method, the number of subdomains were varied from ten to twenty. Seven different decomposition methods were tested, as listed in Table 6.5. The reported clock and CPU times are normalized to one second of model time.

Decomposition method A minimized the clock time. Although decomposition method A was not the most computationally efficient (did not minimize CPU time), in order to save the greatest amount of clock time, method A has been used in all subsequent models. Due to the generous allocation of CPU time from the Texas A&M HPRC group, CPU time was not a constraining resource. Thus, the next most constraining resource, clock time, was chosen to be minimized by using decomposition method A. In total, the research presented in this dissertation consisted of over 3,500 clock hours, or 70,000 CPU hours, of CFD computation time.

Table 6.5: A summary of the computational efficiency study. In order to minimize the clock time, decomposition method A was chosen.

Decomposition Method	**Number of Subdomains**	**Decomposition Coefficients**			**Clock Time per Second of Model Time (Hours)**	**CPU Time per Second of Model Time (Hours)**
		x	y	z		
A	20	2	1	10	4.51	90.1
B	20	5	1	4	5.46	109.2
C	20	4	1	5	5.45	108.9
D	20	10	1	2	4.82	96.3
E	10	1	1	10	6.83	68.5
F	10	2	1	5	6.87	68.8
G	10	10	1	1	5.75	57.6

6.8 CFD Data Analysis

In order to extract meaningful data upon model completion, careful post-processing and data analysis were performed. Once the CFD models completed, the parallel results were reconstructed using OpenFOAM's *reconstrucPar* method and downloaded from the supercomputer. All data analysis took place in ParaView, using the ParaFoam application. The bubble detachment volume for each case was measured at the three timesteps immediately following detachment. The reported bubble detachment volume was taken to be the average of these three measurements. More information on how the bubble's volume was measured is presented in Section 9.2.2.

6.9 CFD Variables

6.9.1 Materials

As detailed in Section 5.4.1, four materials were used for the orifice plates in the CFD model: quartz glass, polycarbonate, 304 stainless steel, and aluminum 6061. Again, these materials were carefully selected for two reasons. First, these materials span the three material classes: metals, polymers, and ceramics. Next, the materials chosen are commonly used in spaceflight systems. Quartz and polycarbonate are common materials for viewing windows of microgravity fluid experiments. Aluminum 6061 is commonly used in spacecraft structures. Finally, 304 stainless steel is used in various components of the ISS environmental control and life support systems (ECLSS) and the portable life support system (PLSS) of the extravehicular mobility unit (EMU) [113–116].

6.9.2 Gas Injection Rates

To satisfy research objectives 3 and 4, a 1 g CFD gas injection study was conducted. The purpose of the CFD gas injection study was to find the gas injection rate, below which, bubble detachment volume remained constant. This would ensure that all jetting effects caused by the kinetic force of gas injection, drag caused by bubble expansion, and the inertial force of the hydrostatic pressure during bubble expansion were all negligible. In all models, the gas and liquid used were room air and distilled water, respectively. The only variable for each orifice plate was the rate at which gas was injected through the orifice.

On each of the four orifice plate materials, the gas injection rate was varied from 7 μL/s to 100 μL/s. The following gas injection rates were tested on each material: 7, 10, 12.5, 17, 20, 25, 27.5, 35, 50, and 100 μL/s. Table 6.6 displays a summary of all variables tested in the 1 g CFD gas injection study. To be discussed in the results in Section 7, the gas injection rate which eliminated jetting effects for each material was chosen and used in all subsequent cases.

6.9.3 Gravity Variation Study

After conducting the 1 g CFD gas injection study and choosing the appropriate gas injection rate, a gravity variation study was conducted. The purpose of the gravity variation study was to study the effects that gravitational acceleration level has on bubble volume at detachment. Thus, on each material, the only variable was the acceleration due to gravity.

For each of the four materials, CFD cases were run at gravity levels between microgravity (10^{-6} g) and 1 g, in $\frac{1}{10}^{th}$ g increments. Lunar and Martian gravity levels were also tested. Table 6.7 presents the gravitational levels tested as part of the CFD gravity variation study.

Table 6.6: 1 g CFD gas injection study variables

Orifice Plate Material	**Constant Flow Rate (μL/s)**
Quartz, Polycarbonate, 304 Stainless Steel, Aluminum 6061	7
Quartz, Polycarbonate, 304 Stainless Steel, Aluminum 6061	10
Quartz, Polycarbonate, 304 Stainless Steel, Aluminum 6061	12.5
Quartz, Polycarbonate, 304 Stainless Steel, Aluminum 6061	17
Quartz, Polycarbonate, 304 Stainless Steel, Aluminum 6061	20
Quartz, Polycarbonate, 304 Stainless Steel, Aluminum 6061	25
Quartz, Polycarbonate, 304 Stainless Steel, Aluminum 6061	27.5
Quartz, Polycarbonate, 304 Stainless Steel, Aluminum 6061	35
Quartz, Polycarbonate, 304 Stainless Steel, Aluminum 6061	50
Quartz, Polycarbonate, 304 Stainless Steel, Aluminum 6061	100

Table 6.7: A summary of all gravitational levels tested as part of the CFD gravity variation study.

G-Level	10^{-6} g	0.1 g	0.167 g (Lunar)	0.2 g	0.3 g	0.378 g (Mars)	0.4 g	0.5 g	0.6 g	0.7 g	0.8 g	0.9 g	1 g
Gravitational Acceleration ($\mathrm{m/s^2}$)	$9.81 * 10^{-6}$	0.981	1.625	1.962	2.943	3.711	3.924	4.905	5.886	6.867	7.848	8.829	9.81

7. VALIDATION OF 1 g CFD RESULTS

7.1 Results of the 1 g CFD Gas Injection Study

The purpose of the 1 g CFD gas injection study was to determine the gas injection rate, below which, the bubble volume at detachment remained constant. Gas injection rates at and below this sufficiently low rate allow for the study of the force balance between buoyancy and interfacial tension by minimizing jetting effects and any other forces which could cause artificially large bubbles or premature detachment. Following the methodology described in Section 6, a CFD model was run at all gas injection rates across all four orifice plate materials and the bubble volume at detachment was measured. Figure 7.1 presents the plots of bubble detachment volume as modeled by CFD versus gas injection rate for the quartz, polycarbonate, 304 stainless-steel, and aluminum 6061 orifice plates.

The data presented in Figure 7.1 includes error bars for each data point. As discussed in Section 5.2, the Sessile drop contact angles, which were used as boundary conditions in the CFD model, had small variations, just as any experimental measurement. Assuming the variations in experimental measurements followed a normal distribution, the error bars were determined as follows. For each gas injection rate, a curve of bubble detachment volume versus equilibrium contact angle was plotted using the results from the four orifice plate materials: quartz, polycarbonate, 304 stainless steel, and aluminum 6061. Regression analysis was then used to determine a curve fit of bubble detachment volume versus equilibrium contact angle for the given gas injection rate. Then, using the equation of the curve fit, the bubble detachment volumes were calculated for ± 1 standard error of the Sessile drop contact angle measurement. The resulting maximum and minimum bubble detachment volumes (with a single standard error variation) were used as the error bars in Figure 7.1. The error bars show that for each material, the difference in bubble volume at detachment is statistically insignificant below gas injection rates of approximately 27.5 μL/s or 35 μL/s. This was taken into account when determining the gas injection rate which eliminated jetting effects.

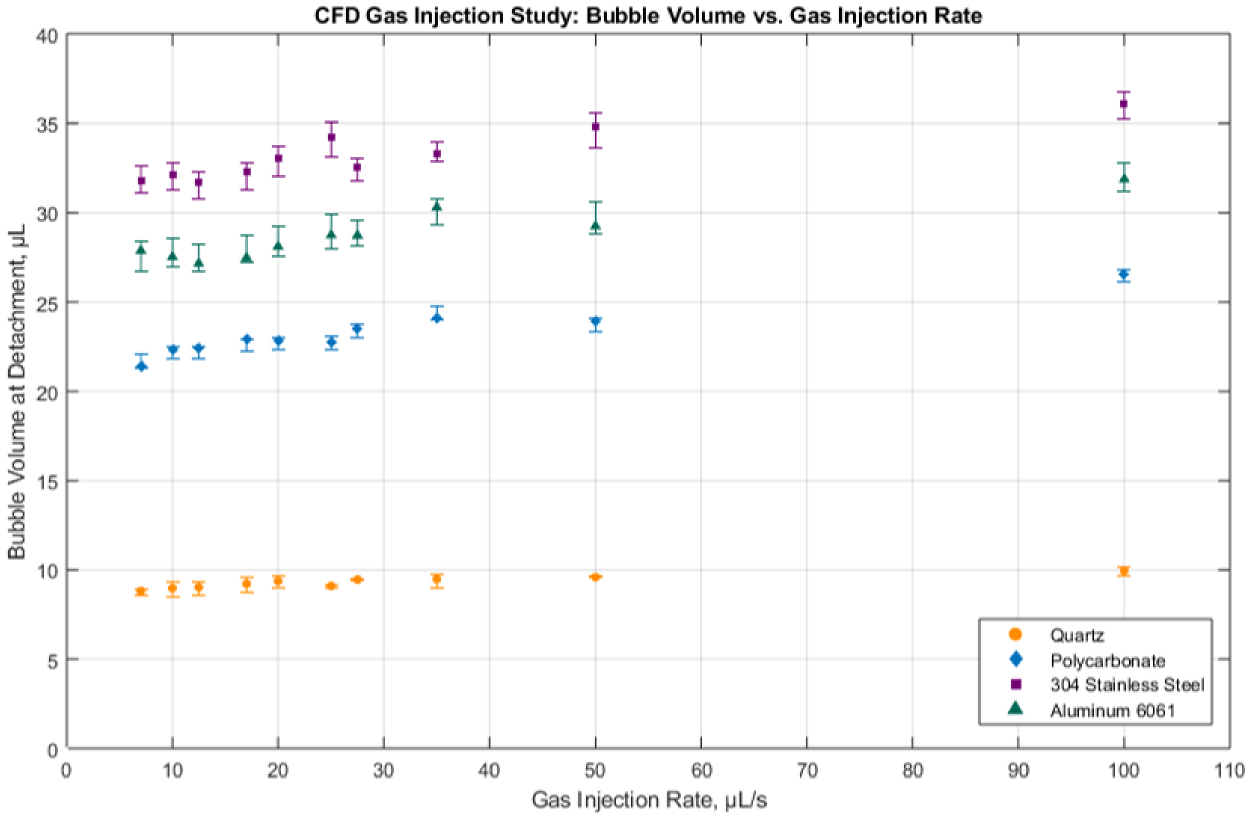

Figure 7.1: Bubble volume at detachment versus volumetric gas injection rate, as modeled by CFD in 1 g.

Each data set follows a similar trend. As the gas injection rate decreases, the bubble volume at detachment decreases, before stabilizing to within ± 1 μL. In the CFD analysis, stabilization was considered the flow rate, below which, the bubble volume at detachment varied by no more than 6%. The gas injection rate at which stabilization occurs varies between each material. For quartz and polycarbonate orifice plates, the CFD bubble volume at detachment stabilized below flow rates of 25 μL/s. For the stainless-steel and aluminum orifice plates, the CFD bubble detachment volume stabilized at gas injection rates at and below 27.5 μL/s. The gas injection rates at which bubble detachment volume stabilized in the CFD models are summarized in Table 7.1.

7.2 Results of the 1 g Experimental Gas Injection Study

The experimental 1 g gas injection study had two objectives. The first objective was to determine the volumetric gas flow rate, below which, the bubble volume at detachment remained

Table 7.1: CFD gas injection rates which eliminated jetting for each orifice plate

Orifice Plate Material	**CFD Gas Injection Rate which Eliminated Jetting (μL/s)**
Quartz	25
Polycarbonate	25
304 Stainless Steel	27.5
Aluminum 6061	27.5

constant. Gas injection rates below this threshold thus, minimize any jetting effects, which could cause artificially large bubble or premature bubble detachment. This gas injection rate is defined as a sufficiently low gas injection rate. The second objective of the experimental 1 g gas injection study was to collect bubble detachment volume data to be used to validate 1 g CFD models.

As described in Section 5, 11 gas injection rates were tested on each of the four orifice plate materials. At each flow rate, a total of 15 experimental trials were conducted and the bubble volume was measured by both the x-axis and y-axis cameras. The experimental data presented in this section reflect the average volume measured by the x-axis and y-axis cameras.

Figure 7.2 presents the plots of bubble volume at detachment versus volumetric gas injection rate for the quartz, polycarbonate, 304 stainless steel, and aluminum 6061 orifice plates. Error bars were determined for each experimental data point. However, the standard error of the mean is so low (on the order of 0.1 μL), that the error bars are not visible on the plot in Figure 7.2. Each data set follows a similar trend. That is, as gas injection rate decreases, the bubble volume at detachment decreases, until it stabilizes to within $\pm$ 1 μL. The point at which the stabilization occurs varies between each material. For quartz and stainless-steel orifice plates, the bubble volume at detachment stabilized at gas injection rates of 30 μL/s and below. On the polycarbonate orifice plate, the bubble volume at detachment was found to stabilize at a gas injection rate of 25 μL/s. Lastly, the aluminum orifice plate plot indicates that bubble volume at detachment stabilizes at a gas injection rate of 27.5 μL/s. The experimental gas injection rates which minimized jetting for each orifice plate are shown in Table 7.2.

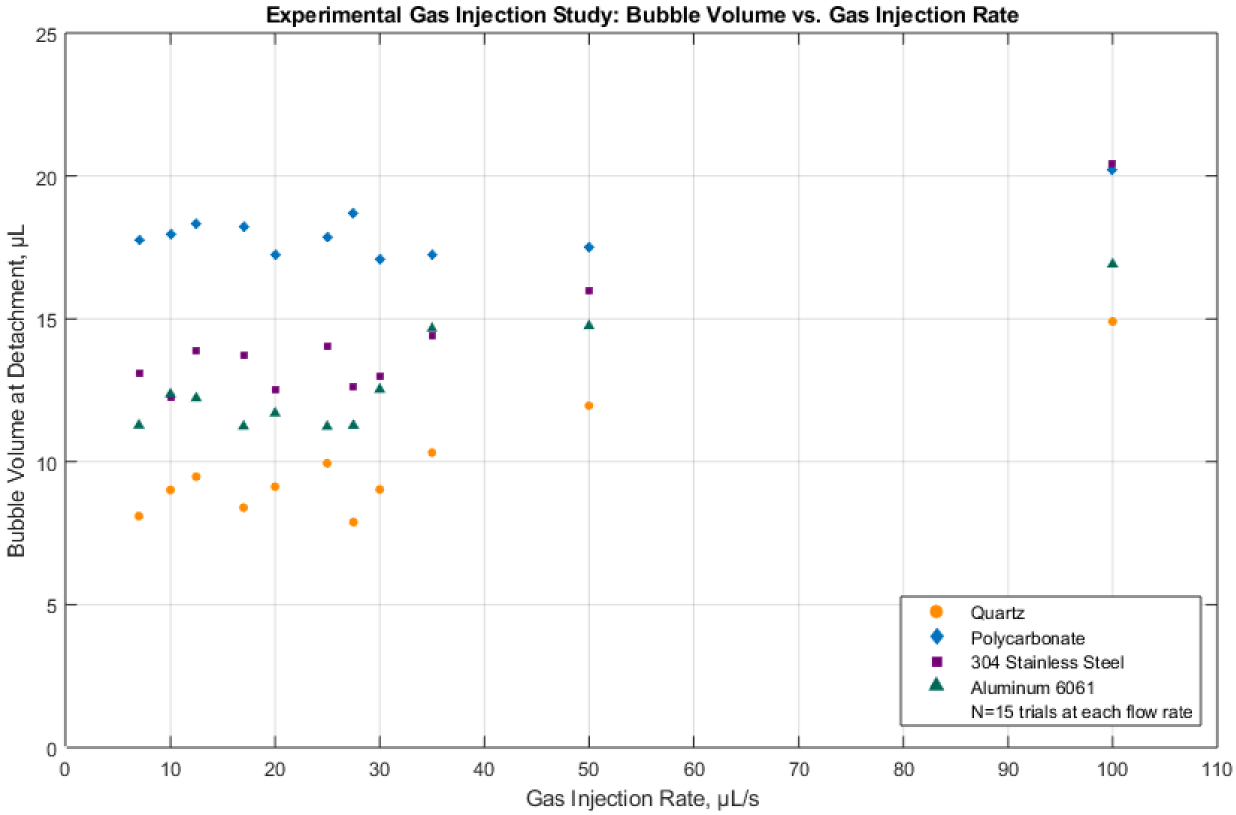

Figure 7.2: Bubble volume at detachment versus volumetric gas injection rate, as measured experimentally in 1 g.

Table 7.2: Experimental gas injection rates which eliminated jetting for each orifice plate

Orifice Plate Material	**Experimental Gas Injection Rate which Eliminated Jetting (μL/s)**
Quartz	27.5
Polycarbonate	25
304 Stainless Steel	30
Aluminum 6061	27.5

7.3 Empirical Validation of 1 g CFD Results

In Earth's gravity, gas injection studies were conducted using both the CFD model and the experimental platform. After determining the gas injection rate which minimized jetting effects, the second objective of the experimental 1 g gas injection study was to validate the 1 g CFD models. The validation occurred by comparing the bubble volume at detachment, as measured by the experimental trials, to the bubble detachment volume modeled by CFD. For the purposes of this analysis, the average bubble volume at detachment was defined as the average of all bubble detachment volumes below the gas injection rate which stabilized the volume measurements, as determined by the CFD analysis. For example, the average 1 g bubble detachment volume for the quartz orifice plate is equal to the average of the bubble detachment volumes at gas injection rates of 7, 10, 12.5, 17, 20, and 25 μL/s. The average experimental and CFD 1 g bubble detachment volumes for each orifice plate are summarized in Table 7.3. The percent difference between the experimental data and CFD bubble detachment volumes are also displayed in Table 7.3. The percent difference was calculated using Equation 7.1.

$$Percent\ Difference\ = \frac{|V_{CFD} - V_{exp}|}{\frac{1}{2}(V_{CFD} + V_{exp})} \tag{7.1}$$

Table 7.3: Comparison between CFD and experimental bubble volume at detachment for each orifice plate

Orifice Plate Material	CFD Bubble Detachment Volume (μL)	Experimental Bubble Detachment Volume (μL)	Experimental Standard Deviation (μL)	Percent Difference
Quartz	9.08	9.01	0.30	0.48%
Polycarbonate	22.42	17.89	0.62	21.1%
304 Stainless Steel	32.51	13.17	0.36	90.8%
Aluminum 6061	27.94	11.61	0.71	82.6%

As discussed in Sections 7.1-7.2, the bubble volume at detachment was measured experimentally and modeled by CFD for each of the four orifice plate materials in 1 g. To reiterate, the constant contact angle CFD boundary condition for the orifice plate was inputted into the CFD model as the average contact angle measured by the goniometer in Section 5.2. Just like every experimental measurement, the average contact angle had a standard deviation and standard error associated with it. Variation in the contact angle has been shown to vary the bubble detachment volume. So, to compare the CFD data to the experimental data, error bars were added to the data points. For the experimental data, the standard error of the bubble detachment volume and equilibrium contact angle (as measured by the goniometer) was used as the height and width of the error bars, respectively. For the CFD data, the error bars were determined as follows. First, the four resulting bubble detachment volumes were plotted with a curve fit determined by regression analysis. The equation of this curve fit is shown in Equation 7.2 and shown in the graph of 7.3.

$$V_b = 0.0003284326 * \theta^3 - 0.0396254990 * \theta^2 + 1.6601656861 * \theta - 15.4315292514 \tag{7.2}$$

Then, using Equation 7.2, the bubble detachment volumes were calculated for ± 1 standard error of the Sessile drop contact angle measurement. The resulting maximum and minimum bubble detachment volumes (with a single standard error variation) were used as the error bars for the CFD data. Just as in the experimental data, the width of the horizontal error bars was equal to the standard error of the contact angle measurements, as measured by the goniometer. Figure 7.4 presents the experimental and CFD bubble detachment volumes and corresponding curve fit and error bars.

Table 7.3 and Figure 7.4 demonstrate that the standard deviations and standard errors were small and thus increase confidence in the data and repeatability of the experiment. The error bars for each measurement indicate that the data points are significantly different. Next, Table 7.3 shows that the CFD models accurately model the quartz and polycarbonate experimental trials to within

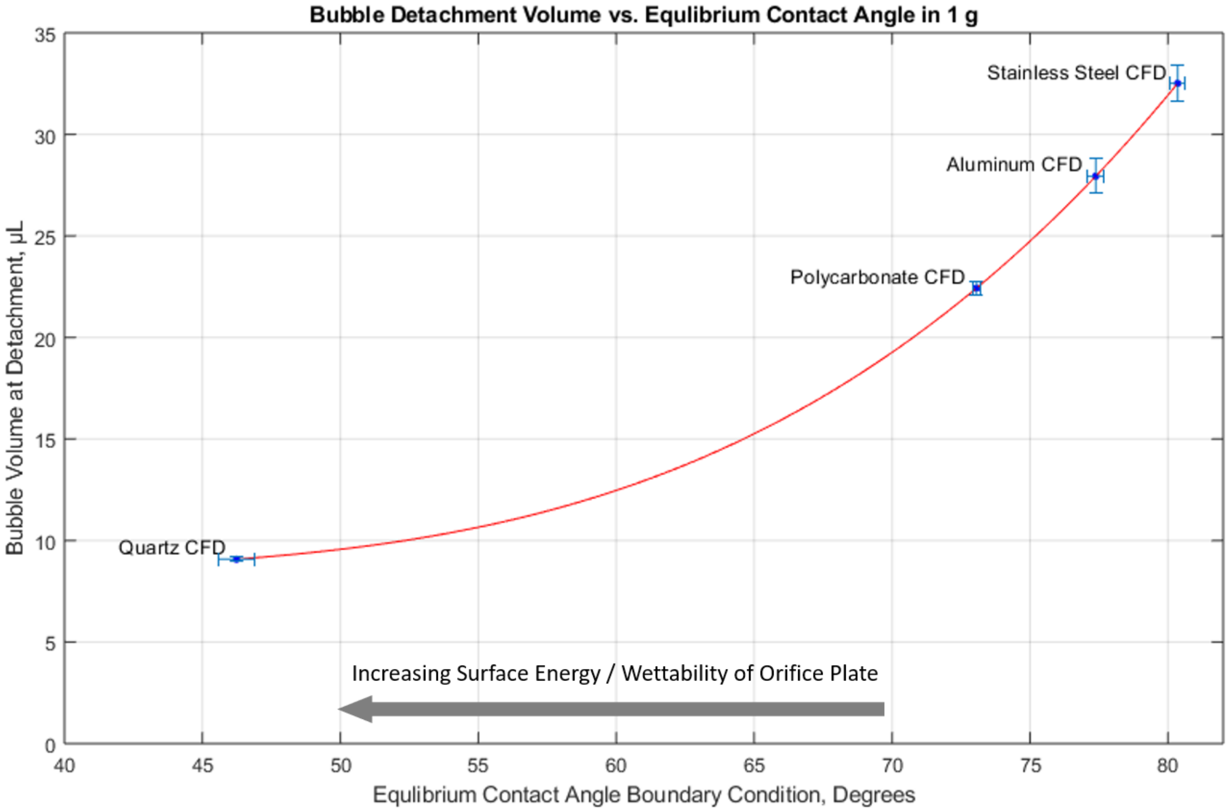

Figure 7.3: Bubble volume at detachment versus constant contact angle boundary condition of orifice plate, as modeled by CFD in 1 g. The curve fit of the data (as determined by regression analysis) is also presented.

0.48% and 21.1%, respectively. When the experimental data at 1g in Figure 7.4 is compared to the CFD data in Figure 7.3, it is observed that the experimental and CFD results for quartz are nearly identical, with both averages and error bars overlaying each other. The experimental results for polycarbonate are lower than the predicted CFD results, although aligned with the trend of the CFD. Unexpectedly, the experimental and CFD bubble detachment volumes for the aluminum and stainless-steel orifice plates however, differ significantly and demonstrate lower bubble detachment volumes in the experimental results. These differences will be discussed further in Section 9.3.

To illustrate the differences and similarities between the 1 g CFD and experimental results, Figures 7.5-7.8 present CFD and experimental sequences of bubble growth and detachment from each orifice plate. The time stamps displayed are all based off of T_d, or the time of bubble detachment.

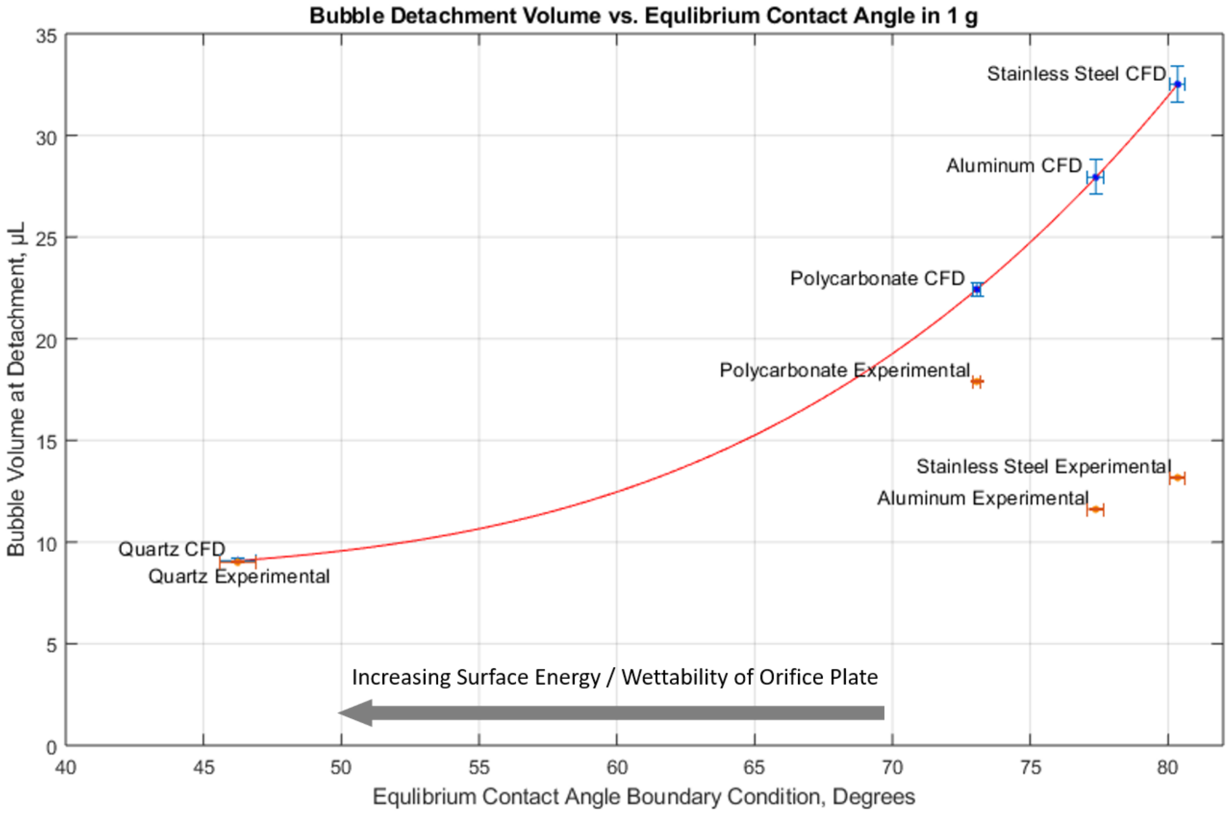

Figure 7.4: Bubble volume at detachment versus Constant Contact Angle Boundary Condition of Orifice Plate, as measured experimentally and modeled by CFD in 1 g.

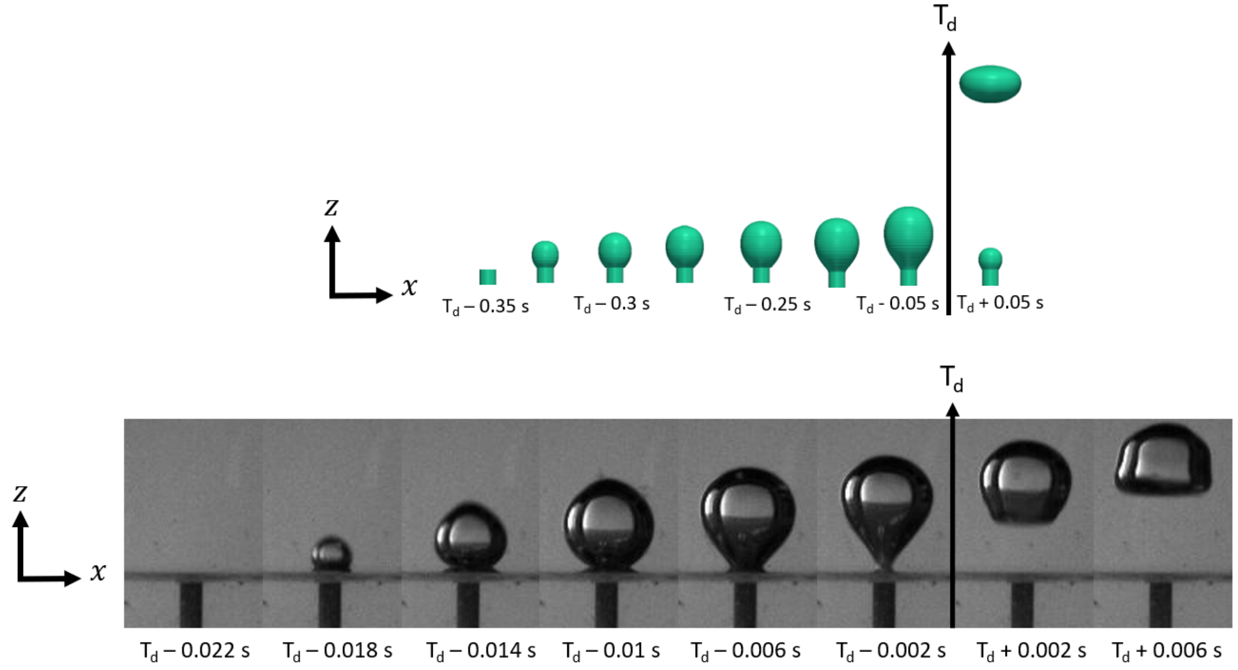

Figure 7.5: CFD (top) and experimental (bottom) sequences of bubble formation and detachment from a quartz orifice plate in 1 g.

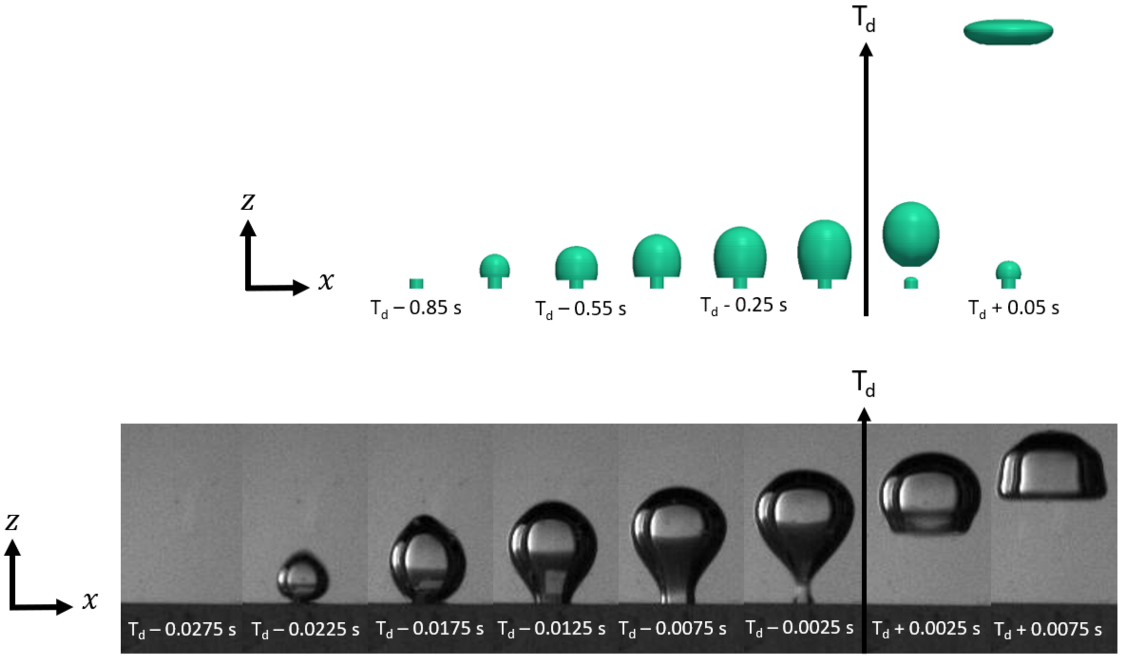

Figure 7.6: CFD (top) and experimental (bottom) sequences of bubble formation and detachment from a polycarbonate orifice plate in 1 g.

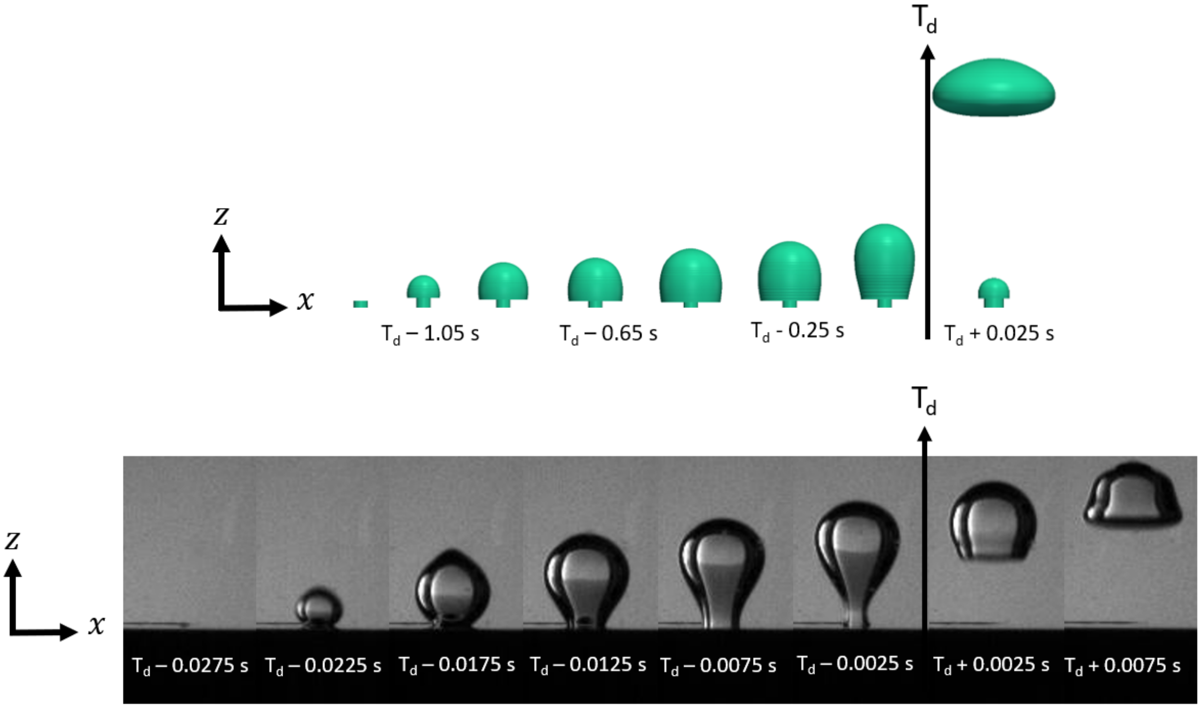

Figure 7.7: CFD (top) and experimental (bottom) sequences of bubble formation and detachment from a 304 stainless-steel orifice plate in 1 g.

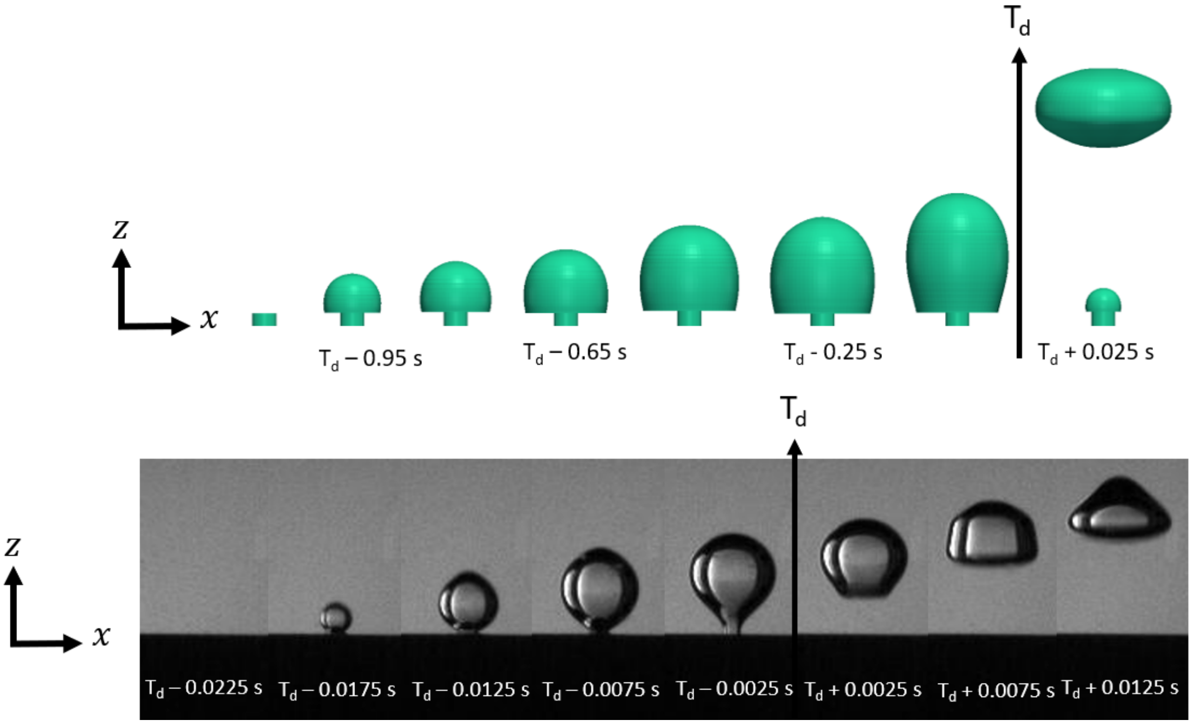

Figure 7.8: CFD (top) and experimental (bottom) sequences of bubble formation and detachment from an aluminum 6061 orifice plate in 1 g.

8. CFD RESULTS (GRAVITY VARIATION STUDY)

After validating the CFD models in Earth's gravity, a gravity variation study was conducted according to the methodology described in Section 6.9.3. To study the effects of gravitational acceleration on bubble behavior, the g-level was varied between microgravity and 1 g on each material. For all orifice plates, the microgravity case was stopped after seven seconds of model time since bubble detachment was not expected. For the quartz model, detachment was observed at 0.1 g. However, for the polycarbonate, stainless-steel, and aluminum cases, file size and memory usage errors were encountered as the limits of the supercomputer allocation were reached after running the models for greater than 200 clock hours. Bubble detachment was therefore not observed in 0.1 g for the polycarbonate, stainless-steel, and aluminum orifice plates.

8.1 Bubble Volume at Detachment vs. Gravitational Acceleration

The bubble volume at detachment was measured for each orifice plate across all gravity levels. Figure 8.1 plots the curves of bubble detachment volume versus gravitational acceleration for each orifice plate.

The CFD data presented in Figure 8.1 includes error bars for each data point. As discussed in Section 5.2, the Sessile drop contact angles, which were used as boundary conditions in the CFD model, had small variations, as expected in all experimental measurements. Assuming the variations in experimental measurements followed a normal distribution, the error bars were determined as follows. For each gravity level, a curve of bubble detachment volume versus equilibrium contact angle (Similar to that shown in Figure 7.3) was plotted using the results from the four orifice plate materials: quartz, polycarbonate, 304 stainless steel, and aluminum 6061. Regression analysis was then used to determine a curve fit of bubble detachment volume versus equilibrium contact angle for the gravity level. Then, using the equation of the curve fit, the bubble detachment volumes were calculated for ± 1 standard error of the Sessile drop contact angle measurement. The resulting maximum and minimum bubble detachment volumes (with a single standard error variation)

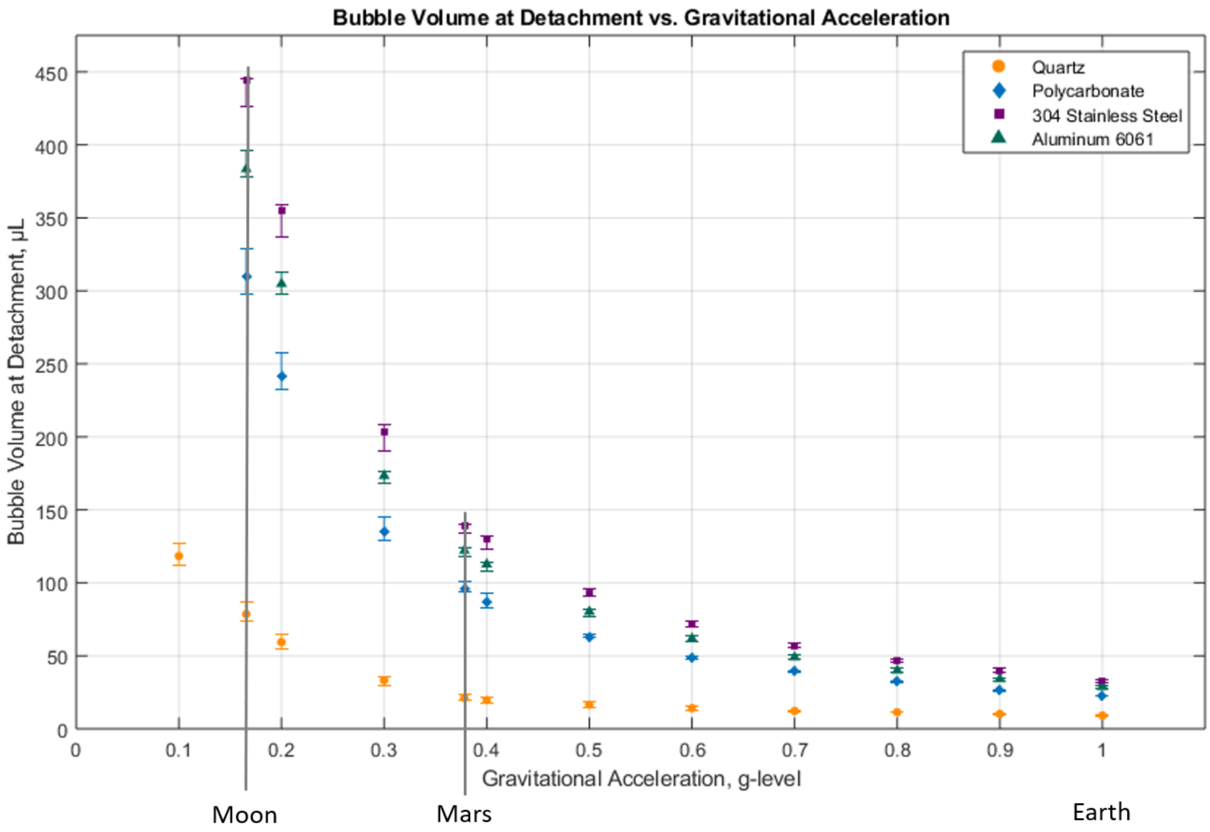

Figure 8.1: Bubble volume at detachment versus gravity level (where 1 g is Earth's gravity, or 9.81 m/s^2) for each orifice plate, as modeled by CFD.

were used as the error bars for the CFD data. The process was repeated for each gravity level. The error bars show that for each material, the difference in bubble volume at detachment is statistically significant for each gravitational acceleration tested.

The bubble detachment volume versus gravitational acceleration plots reveal that each orifice plate material follows a similar trend. That is, as gravitational acceleration is decreased, the bubble volume at detachment increases according to a power law equation of the form in Equation 8.1.

$$V_b = a * g^{-n} \tag{8.1}$$

Table 8.1 gives the values of the power law constants in Equation 8.1 for each material, as determined by regression analysis. As noted by the coefficient of determination (R^2), a very strong fit is observed for each material.

Table 8.1: Power law equation constants and R-squared values for each orifice plate material.

Orifice Plate Material	**Value of Power Law Coefficients**		**R-squared Value**
	a	n	
Quartz	8.113	1.17	0.981
Polycarbonate	23.07	1.455	0.999
304 Stainless Steel	33.83	1.456	0.999
Aluminum 6061	29.24	1.454	0.999

8.2 Bubble Shape vs. Gravitational Acceleration

At lower gravity levels, not only do bubbles increase nonlinearly in volume, but their shape also changes. Related to increased bubble spreading, at lower gravity levels, bubbles appear wider and less elongated in the z-axis. To illustrate this, Figures 8.2-8.3 show a comparison between bubble formation and detachment sequences in 1 g and Lunar gravity. The Lunar gravity cases appear much less elongated in the z-axis throughout bubble growth.

To quantify the change in bubble shape, the bubble's aspect ratio was defined according to Equation 8.2, The bubble's height (b_h) was measured from the orifice to the highest point on the bubble in the z-axis. The bubble's width (b_w) was measured at the widest point on the bubble in the x-axis. The timestep at which the bubble height and width measurements were taken was chosen to be $t = 0.3\ s$ across all materials and all gravity levels. This was the largest timestep for which the bubbles on all orifice plates were still attached.

$$AR = \frac{b_h}{b_w} \tag{8.2}$$

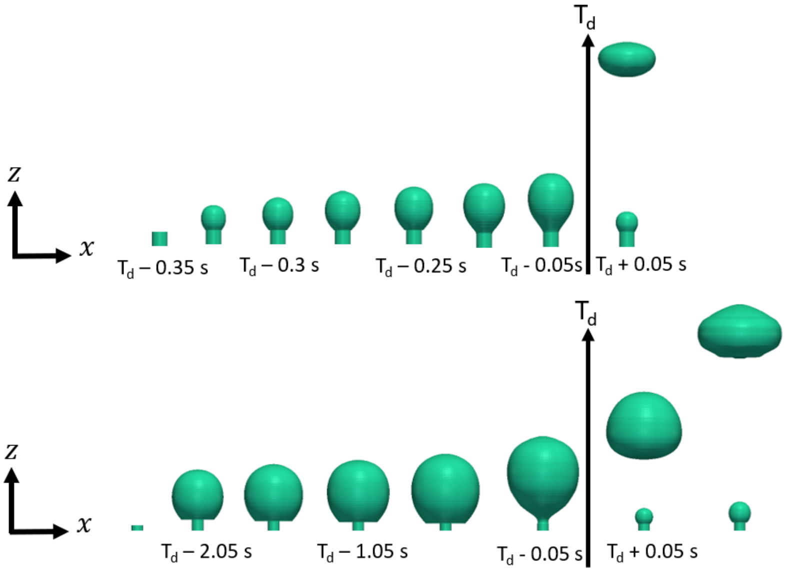

Figure 8.2: CFD sequences of bubble formation and detachment from a quartz orifice plate in 1 g (top) and Lunar gravity (bottom).

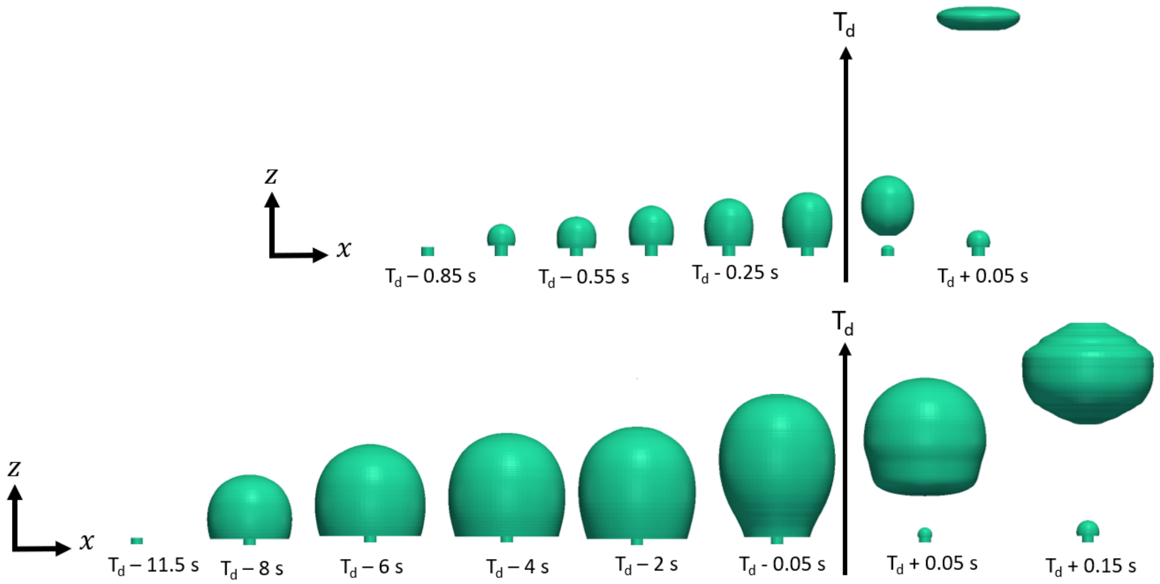

Figure 8.3: CFD sequence of bubble formation and detachment from a polycarbonate orifice plate in 1 g (top) and Lunar gravity (bottom).

Figure 8.4 displays plots of bubble aspect ratio versus gravitational acceleration for all materials. Each orifice plate follows a similar trend. As the gravity level decreases, the aspect ratio decreases, leading to wider bubbles.

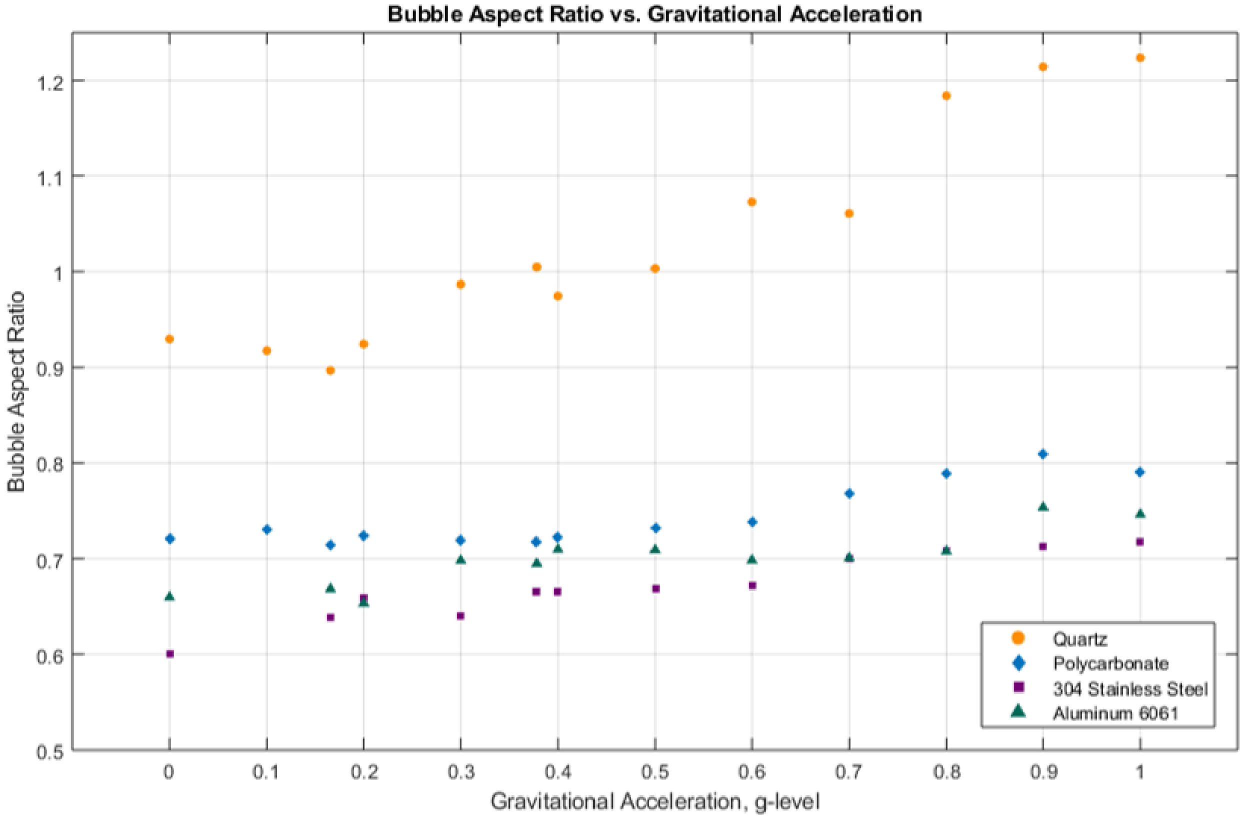

Figure 8.4: Plot of bubble aspect ratio versus gravity level (where 1 g is Earth's gravity, or 9.81 m/s^2) for each orifice plate material.

8.3 Time to Detachment vs. Gravitational Acceleration

When conducting the CFD gravity variation study, the bubble's time to detachment was also recorded. The time to detachment is simply defined as the time between the initiation of gas injection to the time the bubble detaches from the orifice. As one would expect, as bubble volume increases, so does the time to bubble detachment. Figure 8.5 displays the plots of time to detachment, t_d, versus gravitational acceleration. The curves follow a trend which is very similar to the bubble detachment volume versus gravitational acceleration curves. Since gas is injected through the orifice at a constant rate, is it intuitive that time and bubble volume are directly correlated.

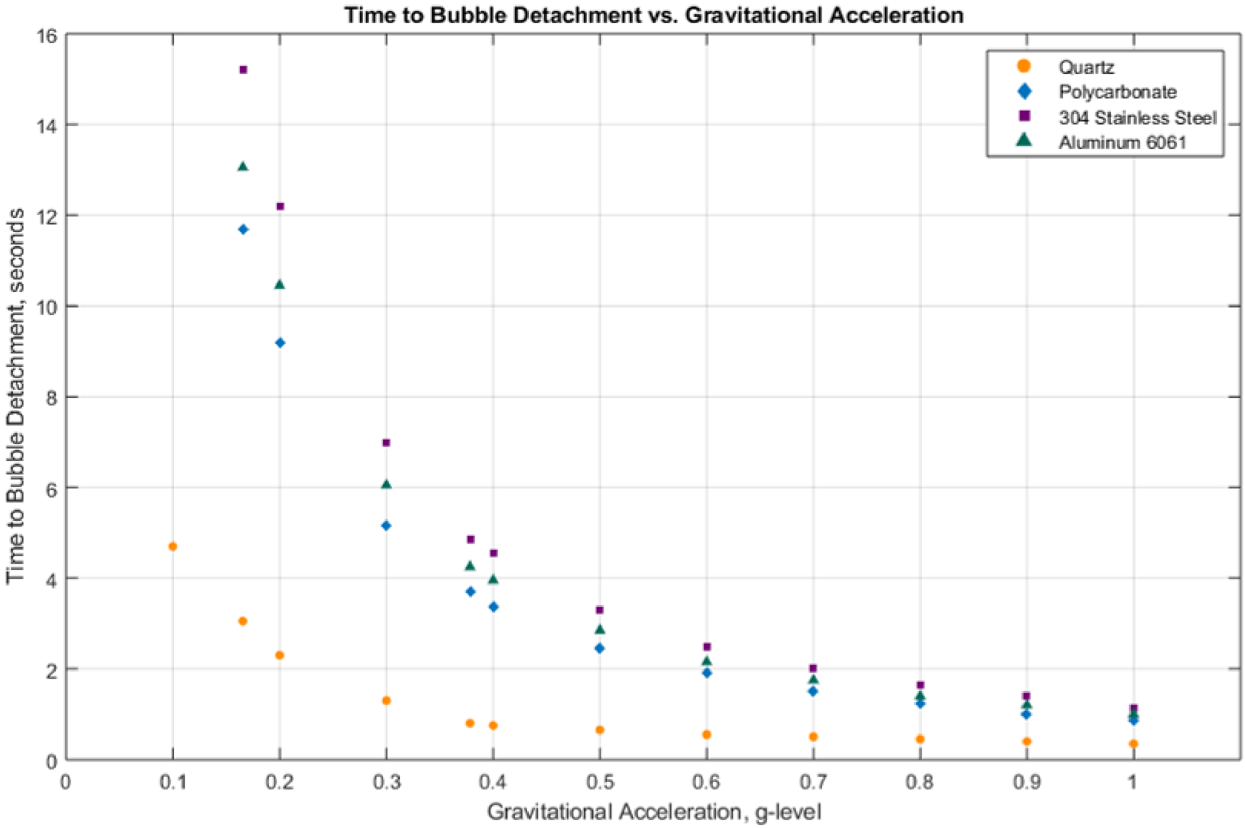

Figure 8.5: Plot of time to bubble detachment versus gravity level (where 1 g is Earth's gravity, or 9.81 m/s^2) for each orifice plate material.

9. DISCUSSION

9.1 Summary of Results and Discussion Introduction

Three approaches were used to study the formation, growth, and buoyancy-driven detachment of a bubble from a submerged orifice. The parameter of interest studied, modeled, and measured across all research was the bubble volume at detachment. Theoretical force balance analysis was first used to define and characterize all forces acting on the bubble. Next, experimental research was conducted using a two-axis high-speed imaging system. Using a shadowgraphy technique, bubble formation and detachment data were collected on four orifice plate materials for two purposes: to determine a sufficiently low gas injection rate and to validate CFD models. In parallel with the experimental work, a volume of fluid (VOF) CFD solver was used to create a CFD model of bubble formation and detachment. The CFD model was first validated in 1 g using the experimental data. The CFD models were then further developed to model bubble formation and detachment across all gravity levels from microgravity to Earth's gravity. It was found that there exists a nonlinear relationship between bubble volume and gravitational acceleration. The curves of bubble detachment volume versus gravity level follow a power law relationship and indicate significant implications for the design of two-phase fluid systems in reduced gravity.

This discussion will first characterize the magnitude of the errors of the CFD models, by presenting its residuals. Then, a discussion of the agreement between experimental and CFD data is presented. The results obtained from this dissertation research are then compared to data sets from past literature. Similarities and differences are noted. Next, a new dimensionless quantity, which describes bubble behavior across gravity levels, is derived and compared to trends produced by the CFD and experimental data. Finally, the possible applications of these results and future work related to this research is presented.

9.2 Residuals and Variation in CFD Measurements

9.2.1 Discussion of CFD Residuals

As with all iterative numerical simulations which solve partial differential equations, the CFD model's conservation of flow properties was measured with residuals [127]. In general, residuals are the instantaneous imbalance of conserved properties [128]. Specifically, the values of the continuity and momentum residuals were monitored throughout the simulation process. Over the duration of all simulations, both the continuity and momentum residuals never rose above values on the order of 10^{-6}. The average residual values were on the order of 10^{-8} to 10^{-7}. These values were considered sufficiently low and indicated a sufficiently refined mesh for the flow being modeled.

9.2.2 Quantification of Bubble Volume Measurement Variation

As discussed in Section 6.8, all CFD data analysis and post-processing were performed in ParaView. To measure the volume of the bubble, the *slice* filter was used. The *slice* filter can threshold a certain fluid property above or below a specified value. In the bubble volume measurements, the phase fraction (α) was the property used to differentiate between the gas of the bubble and the surrounding liquid. The phase fraction was defined as follows in Equations 9.1.

$$\begin{aligned} Cell\ contains\ all\ liquid\ .....\ \alpha &= 1 \\ Cell\ contains\ all\ gas\ .....\ \alpha &= 0 \\ Cell\ contains\ both\ gas\ and\ liquid\ ...\ 0 < \alpha &< 1 \end{aligned} \tag{9.1}$$

This means that the phase front, or bubble boundary, lays in cells where the phase fraction is between the values of 0 and 1. To measure the total bubble volume therefore, the location of the bubble boundary must be determined. The ParaView *slice* filter is used to determine this location. In all volume measurements, a threshold of $\alpha = 0.5$ was used. This means that any cell with a phase fraction of 0.5 or below, was defined as gas and any cell with a phase fraction greater than 0.5 was considered liquid. The bubble volume was then measured as the total volume of all gaseous cells. To illustrate this point, Figure 9.1 shows a simplified two-dimensional mesh containing a bubble's boundary on the left. The right of Figure 9.1 shows the determination of the bubble boundary via a thresholding process, where $\alpha = 0.5$. As can be seen, cells with phase fractions equal to 0.51 were considered liquid, and cells with phase fractions equal to 0.48 were considered gas.

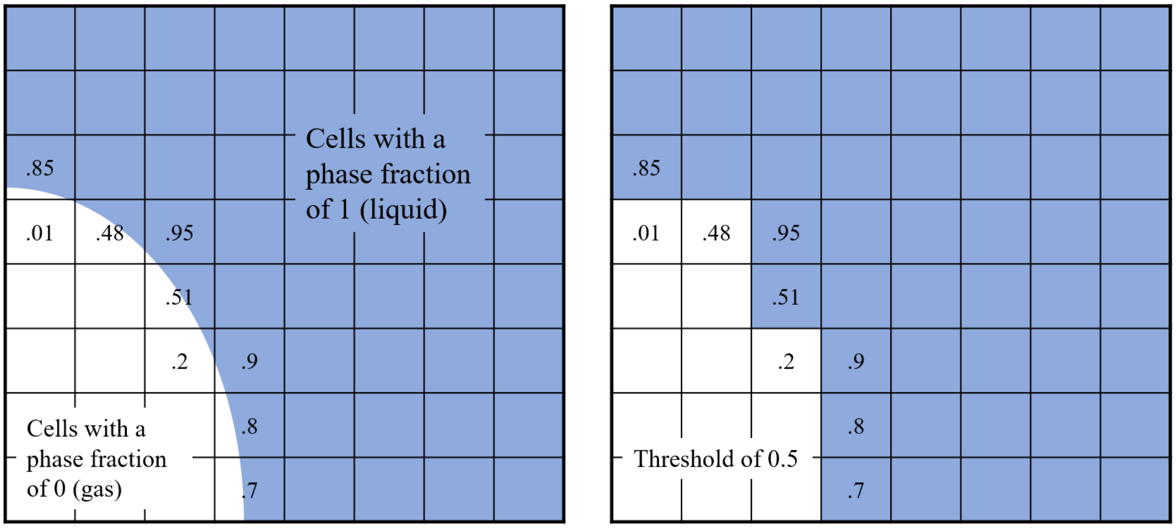

Figure 9.1: A simplified thresholding process showing: A bubble boundary overlaying a mesh with cells containing phase fraction values (left) and a measurement of bubble volume with a phase fraction threshold of 0.5 (right).

The creation of the threshold at a phase fraction of 0.5 is intuitive, but could leave some room for variation in bubble volume measurement. To determine the magnitude of this possible variation, high and low threshold extremes were tested. The phase fraction threshold was varied from $0.5 \pm 5\%$, or $0.5 \pm .025$, or from 0.475 to 0.525. Another simplified example of this threshold variation is shown in Figure 9.2. It is shown that a threshold of 0.475 produces the smallest bubble and a threshold of 0.525 produces the largest bubble. While the variation appears large in this simplified example, it is important to remember that the cells are much smaller in the actual CFD model, where an average cell width is equal to 0.05 mm.

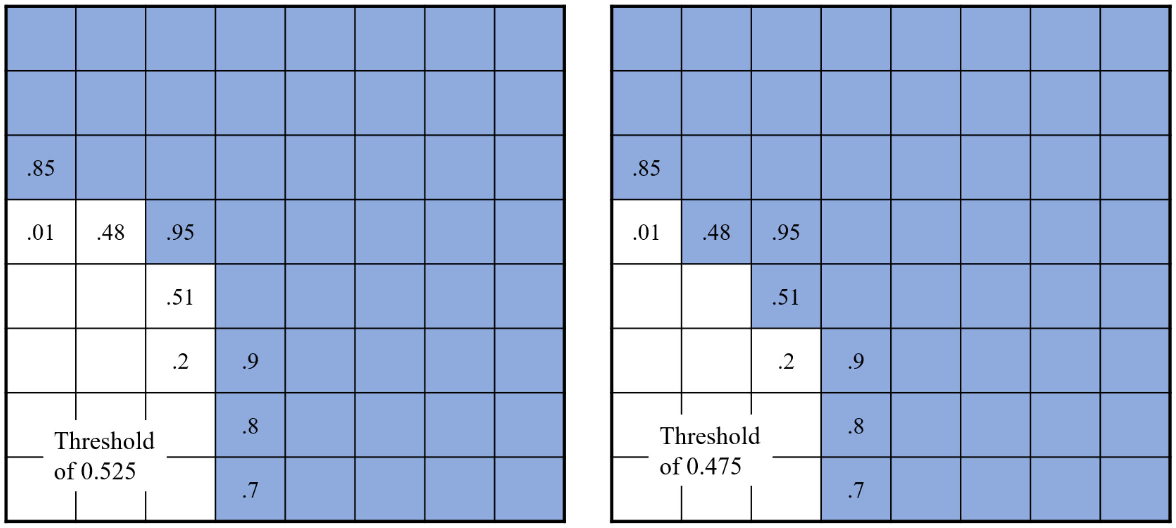

Figure 9.2: A simplified thresholding process showing: A measurement of bubble volume with a phase fraction threshold of 0.525 (left) and a bubble volume measurement with a phase fraction threshold of 0.475 (right).

The 10% threshold variation was applied to the CFD model to quantify the variation in bubble volume measurements. Table 9.1 displays the volume of a bubble forming on a quartz orifice plate as measured with different phase fraction thresholds.

Table 9.1: Effect of phase fraction threshold on measurement of bubble volume

Phase Fraction Threshold	**Measured Bubble Volume (μL)**
0.475	9.12
0.5	9.17
0.525	9.22

Even with a 10% variation in the phase fraction threshold, the bubble volume varied by at most 1%, just under 0.1 μL. Similar to the sufficiently low residuals, a 1% variation in bubble volume measurements was considered negligible and indicated a sufficiently refined mesh.

9.3 Comparison of Experimental and CFD Results

Table 7.3 presents a comparison between the bubble detachment volumes measured experimentally and those modeled by CFD in 1 g. Good agreement is observed for the bubble detachment volumes produced by the quartz and polycarbonate orifice plates. The stainless-steel and aluminum orifice plates, however, show significant differences in the bubble detachment volumes presented by the CFD model and experimental trials. The visual representations in Figures 7.5-7.8 present some important observations, which can be used to explain the differences between empirical and CFD bubble detachment volumes. Figures 7.5-7.8 display comparisons between the experimental and CFD bubble behavior, defined here as bubble shape, spreading, size, etc. For the quartz orifice plate, the bubble behavior matches quite well between the CFD models and experimental results. That is, in both the CFD visuals and experimental images, the bubble remains pinned to the orifice rim and does not spread beyond the orifice. For the polycarbonate case, the bubble behavior matches well, as the bubble does spread beyond the orifice rim in both the CFD and experimental sequences. Although difficult to observe experimentally, the bubble on the polycarbonate orifice plate does at least spread slightly beyond the rim. This agreement is not observed for the stainless-steel and aluminum orifice plates. For both stainless steel and aluminum, little to no bubble spreading is observed in the experimental sequences, while significant spreading *is* observed in the CFD model. The CFD model also displays bubbles which are more elongated in the x-axis than those observed experimentally. This indicates that bubble behavior does not match between the stainless-steel and aluminum CFD and experimental sequences.

It is shown in Equation 4.5 that when a bubble spreads beyond the orifice perimeter (mode B bubble growth), the magnitude of the interfacial tension force increases, since the bubble contact area with the orifice plate also increases. An increase in the interfacial tension force leads to an increase in the bubble's volume at detachment. So, a CFD model which overpredicts the magnitude of bubble spreading, would lead to a larger bubble detachment volume than is measured from an experimental trial which does *not* exhibit bubble spreading. Therefore, CFD models which accurately predict experimental bubble behavior (bubble shape and spreading), result in bubble detachment volumes which agree well with experimental data. In this case, the CFD models accurately predicted bubble behavior, and thus bubble detachment volume, for the quartz and polycarbonate orifice plates. When the bubble behavior does not match between the CFD and experimental results, the bubble detachment volumes do not match either. This is observed for the stainless-steel and aluminum orifice plates, for which the CFD model predicts a much larger amount of bubble spreading than is observed experimentally. Possible causes of these discrepancies for the stainless-steel and aluminum cases, which will be investigated in future work, are discussed further in Section 9.10.

9.4 Comparison of CFD Results with Data from Past Literature

Since no empirical data exists to validate the CFD models at partial gravity levels, the results were compared to data and trends produced by past literature.

9.4.1 Comparison of Gas Injection Study with Gerlach's Findings

Using a 1 g CFD model for submerged-orifice bubble behavior, Gerlach conducted a gas injection study on various orifice plates. The data cannot be directly compared since Gerlach used a larger orifice diameter (1 mm) and different materials [87] than the present research in this dissertation. However, Gerlach found a trend which agrees with the trend presented in Section 7. That is, below a specific constant gas injection rate, the bubble volume at detachment remains constant, indicating the elimination of jetting effects.

9.4.2 Comparison of Gravity Variation Study with Data found in the Literature

Qui conducted experiments onboard a parabolic aircraft to determine the relationship between bubble volume at detachment and gravity level for pool boiling on a silicon heater [89]. Qui's experimental data found that bubble detachment volume scales with gravity level according to a power law relation expressed by Equation 9.2 [89].

$$V_d \propto g^{-1.5} \tag{9.2}$$

The CFD results presented in Section 8 show an average power law exponent of 1.41; indicating good agreement with Qui's experimental observations. When the quartz CFD model is not considered, the average power law exponent is 1.47. This is a good indication that bubble formation and detachment from an orifice can approximate pool boiling bubble behavior. Reasons why the quartz case may vary slightly from the other orifice plates is discussed further in Section 9.6.3.

The CFD results in Section 8 were also compared to Di Bari's CFD results. Di Bari developed a level set CFD model of bubble formation and detachment from a submerged orifice [36]. Di Bari concluded that his CFD model indicates an inverse relationship between bubble detachment volume and gravity level ($V_d \propto g^{-1}$) [36]. However, Di Bari's only data points were on a single material at gravity levels of 0.5 g, 1 g, and 1.5 g. It is hypothesized that with additional data points at reduced gravity levels, Di Bari's model would approach the relationship ($V_d \propto g^{-1.5}$) found by Qui's experimental work and the CFD results presented in Section 8.

9.4.3 Comparison of Bubble Detachment Volume versus Equilibrium Contact Angle Trend with Gerlach's Findings

Gerlach used a CLSVOF CFD solver to model bubble formation and detachment from a submerged orifice in 1 g. One important result was the relationship between bubble volume at detachment and equilibrium contact angle boundary condition of the orifice plate. Gerlach found that there was a cubic relationship between bubble detachment volume and the orifice plate's equilibrium contact angle. The CFD data in Section 7.3 was plotted to obtain a curve of bubble detachment volume versus orifice plate equilibrium contact angle, as shown in Figure 7.4 for the 1 g case. The best curve fit for Figure 7.4 was determined. The regression analysis produced a cubic curve fit ($V_d \propto \theta^3$), as shown in Equation 7.2, indicating strong agreement with Gerlach's 1 g CFD models.

9.5 Analytical Derivation of a New Dimensionless Quantity, *Bu*, for Scaling Bubble Behavior Across Gravity Levels

Section 4 presents a complete force balance analysis of all forces which act on a bubble rising from a submerged orifice. Assuming low gas injection rates, jetting effects were neglected and the balance between buoyancy and the surface and interfacial tension forces was expressed as Equation 9.3.

$$\sum \boldsymbol{F} = (\rho_{liquid} - \rho_{gas}) * g * V_{gas} - \pi * d_c * \sigma = 0 \tag{9.3}$$

At the moment Equation 9.3 is completely balanced, the forces favoring bubble detachment equal the forces favoring bubble attachment to the orifice plate. When the bubble grows differentially larger, the upward forces are infinitesimally larger than the downward forces and bubble detachment occurs. Suppose a non-dimensional parameter is defined as the ratio between the balanced forces in Equation 9.3. Define this dimensionless quantity as the **Bu**bble scaling number, Bu. Equation 9.4 presents the equation for Bu, where V_b is the volume of the bubble, d_b is the diameter of the bubble, g is the acceleration due to gravity, $\Delta\rho$ is the difference in gas and liquid densities, σ_{sg} is the solid surface energy of the orifice plate, and d_c is the contact diameter.

$$Bu \ = \ \frac{V_b \ g \ \Delta\rho}{\pi \ d_c \ \sigma_{sg}} \ = \ \frac{d_b^3 \ g \ \Delta\rho}{6 \ d_c \ \sigma_{sg}} \tag{9.4}$$

For the purposes of analysis, the volume at which detachment occurs is assumed to be the maximum bubble volume, since the bubble detaches and no additional gas can be injected. Define this volume as $V_{b\,max}$. It is also assumed that at the moment Equation 9.3 is balanced and detachment begins, the contact diameter is at its maximum magnitude. Define this contact diameter as $d_{c\,max}$. By definition, the value of Bu necessary for detachment, occurs when $V_b = V_{b\,max}$ and $d_c = d_{c\,max}$. This is defined as the critical Bu, denoted Bu^*, and is shown in Equation 9.5.

$$Bu^* = \frac{V_{b\,max} \ g \ \Delta\rho}{\pi \ d_{c\,max} \ \sigma_{sg}} \tag{9.5}$$

It is noted that Equation 9.5 can often not be solved since the contact diameter is not known. Chesters performed analytical analysis to find key bubble parameters across mode A and mode B bubble growth [78]. Chesters notes that no analytical solution exists for bubble contour, volume, or contact diameter at any time, but analytical solutions *do* exist for the *maximum* bubble volume and *maximum* contact diameter [78]. Chesters analytically found $d_{c\,max}$ for all bubbles which exhibit mode B growth and maintain a constant contact angle with the orifice plate [78]. Equation 9.6 presents the equation for the maximum contact diameter.

$$d_{c\,max} = \left(\frac{9}{8\sqrt{2}}\right) * sin(\theta)^2 * \sqrt{\frac{\sigma_{lg}}{g\ \Delta\rho}} \tag{9.6}$$

Substituting Equation 9.6 into Equation 9.5, yields Equation 9.7. Equation 9.7 is the Bu number at the moment of bubble detachment. Unlike Equation 9.5 which contained the unknown $d_{c\,max}$ term, Equation 9.7 is only dependent upon the bubble volume (which can be measured) and fluid and solid material properties (which are known for a given material/fluid combination). Equation 9.7 will be used in Section 9.6 to calculate Bu at detachment for the CFD and experimental trials.

$$Bu^* = \frac{8\sqrt{2}\ \ V_{b\,max}\ \ g^{1.5}\ \ \Delta\rho^{1.5}}{9\pi\ \ \sigma_{sg}\ \ \sigma_{lg}^{0.5}\ \ sin(\theta)^2} \tag{9.7}$$

Fritz performed analytical analysis, validated by experimental work, to determine the maximum diameter a bubble can obtain before detaching [69, 75]. Fritz assumed mode B bubble growth in all analysis [75, 129]. Using Fritz's definition of the detachment diameter, the maximum bubble volume ($V_{b\,max}$) was calculated. Equation 9.8 presents the expression for the maximum volume a bubble can obtain while still attached to a surface, where σ_{lg} is the liquid-gas surface tension and θ is the contact angle between the phase front and the orifice plate. This can also be referred to as the bubble volume at detachment, V_d.

$$V_d = V_{b\,max} = \frac{\pi}{6} * (d_{b\,max})^3 = \frac{2^{1.5}\ \pi\ \ 0.851^3\ \ sin(\theta)^3\ \ \sigma_{lg}^{1.5}}{6\ \ g^{1.5}\ \ \Delta\rho^{1.5}} \tag{9.8}$$

Substituting Equation 9.8 into Equation 9.7, yields Equation 9.9.

$$Bu^* = \frac{16}{27} * 0.851^3 * \frac{sin(\theta)\ \ \sigma_{lg}}{\sigma_{sg}} \tag{9.9}$$

It can be seen that the critical Bu number, Bu^*, is only dependent upon the material and fluid properties of the system. This means that for any given fluid/material system, the Bu^* needed for detachment is constant.

As stated previously, the above analysis assumes that the only forces which act on the bubble are buoyancy, surface and interfacial tension forces, and the weight of the gas in the bubble. The analysis also assumed all bubbles grow according to mode B bubble growth. This is a good assumption since even mode A bubbles spread infinitesimally beyond the orifice edge [78].

9.6 Comparison of CFD Results to Trends Predicted by *Bu*

While no experimental data sets exist for validation of CFD models in reduced gravity, the analytical work and dimensionless quantity derived in Section 9.5 can be compared to the trends found from the CFD results.

9.6.1 Trend of Bubble Detachment Volume versus Gravity Level

Figure 8.1 displays the nonlinear trend as bubble detachment volume scales across gravity levels. The trend exhibited in the curves of Figure 8.1 were compared to the trends predicted by Bu. During the development of Bu, Section 9.5 presents an equation for the maximum bubble volume, or volume at detachment. For completeness, the equation is repeated here in Equation 9.10.

$$V_d = V_{b\,max} = \frac{\pi}{6} * (d_{b\,max})^3 = \frac{2^{1.5}\ \pi\ \ 0.851^3\ \ sin(\theta)^3\ \ \sigma_{lg}^{1/5}}{6\ \ g^{1.5}\ \ \Delta\rho^{1.5}} \tag{9.10}$$

The bubble volume at detachment is shown to have a nonlinear relationship to gravitational acceleration according to the relation in Equation 9.11.

$$V_d\ \propto\ g^{-1.5} \tag{9.11}$$

Table 8.1 shows that for every material except quartz, the CFD produces a bubble detachment volume versus gravity level power-law curve fit with exponents on g between -1.454 and -1.512. This matches extremely well with the predicted, theoretical scaling ($g^{1.5}$) of bubble detachment volume across gravity levels shown in Equation 9.11. This builds confidence in the power law form of the equation and the power law constants produced by the CFD models. Section 9.6.3 will discuss possible causes of the deviation found on the quartz orifice plate.

9.6.2 Critical *Bu* Number

The critical bubble scaling number, denoted Bu^*, is defined as the value of Bu at the moment bubble detachment begins, when the bubble volume and contact diameter are maximized. The theoretical value of Bu^* for each orifice plate was calculated using Equation 9.9, repeated below in Equation 9.12. Table 9.2 displays the theoretical Bu^* for each orifice plate material.

$$Bu^* = \frac{16}{27} * 0.851^3 * \frac{sin(\theta)\ \ \sigma_{lg}}{\sigma_{sg}} \tag{9.12}$$

Table 9.2: Values of the Critical Bu number (Bu^*), as calculated theoretically for each orifice plate

Orifice Plate Material	**Theoretical Bu^***
Quartz	0.367
Polycarbonate	0.606
304 Stainless Steel	1.01
Aluminum 6061	0.942

To compare with the theoretical Bu^* values, CFD results were used to calculate Bu^* at all gravity levels for each orifice plate. The calculation was performed at the moment of bubble detachment using Equation 9.7, repeated below in Equation 9.13.

$$Bu^* = \frac{8\sqrt{2}\ \ V_{b\,max}\ \ g^{1.5}\ \ \Delta\rho^{1.5}}{9\pi\ \ \sigma_{sg}\ \ \sigma_{lg}^{0.5}\ \ sin(\theta)^2} \tag{9.13}$$

All material and fluid properties, such as solid surface energy and water surface tension were known. The $V_{b\,max}$ was taken to be the bubble detachment volume, as modeled by CFD. The contact angle, θ was taken to be the equilibrium contact angle boundary condition used in the CFD models. The same was done for the experimental results in 1 g. Table 9.3 compares the theoretical Bu^* to the Bu^* values calculated from CFD data across all gravity levels and experimental data collected in 1 g. For the CFD results, the Bu^* values remained nearly constant across all gravity levels for a given material (with standard deviations between 0.02-0.06). The reported values for the CFD model are averaged across all gravity levels.

Table 9.3: Values of the Critical Bu number, as calculated for each orifice plate from the theoretical analysis, from the CFD model, and experimentally.

Orifice Plate Material	**Theoretical Bu^***	**Bu^* modeled by CFD**	**Bu^* found experimentally**
Quartz	0.367	0.334	0.481
Polycarbonate	0.606	0.846	0.678
304 Stainless Steel	1.01	1.88	0.756
Aluminum 6061	0.942	1.56	0.644

Excellent agreement is shown between the theoretical and calculated Bu^* values for the quartz orifice plate. Fairly good agreement is observed for the polycarbonate orifice plate, and differences are seen on the stainless-steel and aluminum orifice plates. These differences will be discussed in Section 9.6.3. Nevertheless, the agreement of critical Bu numbers across gravity levels builds further confidence in the reduced gravity CFD model. Although the precise values of Bu^* may display some differences between theoretical and calculated values for the metallic orifice plates, the general trends remain the same. That is, as surface energy decreases (stainless steel being the lowest), bubble volume and Bu^* increase (stainless steel being the largest).

Again, these results are significant and could be extremely useful. For a given fluid/solid combination, a single value of Bu^* can be calculated using only material and fluid properties. For a chosen material, this critical value, Bu^*, is constant across all gravity levels. So by calculating Bu^* and measuring a bubble volume at detachment in 1 g, a bubble's volume can be predicted for any other gravity level.

9.6.3 Limitations of Scaling Bubble Behavior with *Bu*

Using the derivations of Bu, an equation for the maximum bubble volume, or volume at detachment, was found. Both the theoretical equation (Equation 9.8) and the curved-fitted CFD data show that the bubble detachment volume scales nonlinearly, proportional to $g^{-1.5}$. Great agreement between the CFD data and Bu scaling was observed for all orifice plates, except quartz (which scaled bubble detachment volume proportional to $g^{-1.17}$). However, at higher gravity levels near 1 g, the bubbles forming on the quartz orifice plate most likely experienced a mix between mode A and mode B bubble growth and spreading. Since the development of Bu assumed mode B bubble growth, the assumption may not be valid on the quartz orifice plate in gravity levels near 1 g, thus leading to slight disagreements.

As another comparison to the CFD models, the theoretical critical Bu numbers were calculated for each orifice plate. Using data measured from the CFD models, the value of Bu^* was calculated at each gravity level for each orifice plate. Good agreement is seen between the theoretical Bu^* values and those produced by CFD and experimental trials for the quartz and polycarbonate orifice plates. The stainless-steel and aluminum CFD trials, however, deviated from the theoretical Bu^* values. Chesters explained why this deviation might have occurred [78]. Throughout the theoretical analysis in Section 9.5, the bubble's instantaneous contact angle with the orifice plate was assumed to be equal to the equilibrium Sessile drop contact angle. This is a good assumption for low contact angles, such as those measured on the quartz orifice plate [130]. Once the contact angle gets too large, the assumption of constant contact angle starts to break down, and an analytical solution for bubble contours no longer exists [78, 130]. In these cases, the contact angle attains its equilibrium value much more slowly [78]. Chesters also explains that the use of water as a liquid can compound the issues experienced with materials with large contact angles, due to water being a polar molecule [78]. It is expected therefore, that the closest agreement between theoretical and CFD results occurs at the higher surface energy materials of quartz and polycarbonate.

9.7 Summary of Force Balance and Dimensionless Quantity, *Bu*

The CFD models and analytical work reveal that the magnitude of bubble spreading beyond the orifice is affected by a change in gravity level, such that as the gravitational acceleration is decreased, the bubbles experience increased spreading beyond the orifice. This is shown visually in Figures 8.2-8.3 and analytically in Equation 9.6. Even the bubbles growing on the quartz orifice plate, which experienced minimal bubble spreading in the 1 g CFD models, experience significant spreading at reduced gravity levels. It is shown that a bubble which spreads beyond the orifice increases the magnitude of the interfacial tension force, as observed in Section 4 where the contact diameter, d_c, in Equation 4.7 increases. An increase in the interfacial tension force (caused by increased bubble spreading) leads to an increase in the bubble's volume at detachment.

The critical Bu number (Bu^*) defines a necessary condition for bubble detachment for a specific orifice plate and fluid combination across all gravity levels. For a given orifice plate and fluid, the value of Bu^* remained constant across all gravity levels. Larger Bu^* values, also indicate larger bubble volumes at detachment. Although the metallic plates showed differences in the theoretical Bu^* and CFD-generated Bu^* values, the general trends are still extremely useful. Simple and quick calculations of Bu^* for a range of material and fluid combinations can allow the easy comparison of bubble detachment volume across a range of variables. Say, for example, two material/fluid systems were being compared: system A and system B. If system A produces a larger Bu^* value, this indicates that at all gravity levels, bubbles formed in system A will be larger at detachment than bubbles formed in system B.

Dimensionless quantities are extremely important in fluid mechanics. A Bu^* which scales across gravity levels means that bubble detachment volume can be scaled across gravity levels, as long as the Bu^* remains constant. For instance, assuming all other properties remain constant, the Bu^* could be used to characterize a 0.25 g experiment in a 1 g laboratory by simply using fluids with one-fourth the density difference.

9.8 Consideration of other Dimensionless Quantities: Bond and Weber Numbers

The behavior produced by the CFD is generally unexpected. Traditional techniques of scaling across gravity levels, such as using the Bond number, fail to account for this behavior. The Bond number, shown in Equation 9.14, is a dimensionless quantity which is the ratio of gravitational to surface tension forces on a bubble. It is typically used to characterize the shape of bubbles completely surrounded by a fluid.

$$Bo = \frac{\Delta\rho\ g\ D^2}{\sigma_{lg}} \tag{9.14}$$

Typically, D is taken as the bubble diameter. For the purposes of comparison, the Bubble scaling number (Bu) and the critical bubble scaling number (Bu^*) are repeated below.

$$Bu = \frac{V_b\ g\ \Delta\rho}{\pi\ d_c\ \sigma_{sg}} \tag{9.15}$$

$$Bu^* = \frac{8\sqrt{2}\ V_{b\,max}\ g^{1.5}\ \Delta\rho^{1.5}}{9\pi\ \sigma_{sg}\ \sigma_{lg}^{0.5}\ sin(\theta)^2} = \frac{16}{27} * 0.851^3 * \frac{sin(\theta)\ \sigma_{lg}}{\sigma_{sg}} \tag{9.16}$$

While the Bu number does appear to be of the same form as the Bond number, some important differences exist. First, one could argue that $V_{b\,max}$ could be expanded to $\left(\frac{\pi}{6}\ d_{b\,max}^3\right)$ to obtain a form similar to the Bond number which contains a distance squared (D^2). However, $d_{b\,max}$ cannot be canceled out with $d_{c\,max}$ since they are two entirely different quantities, meaning that the form of the Bond number (with D^2) cannot be obtained.

Next, the Bu number accounts for solid-fluid interactions, unlike the Bond number. The Bond number has no terms which account for the interfacial tension force when a solid surface is in contact with the liquid/gas interface of a bubble, such as when the bubble spreads beyond the orifice.

The Bu number on the other hand, accounts for the equilibrium contact angle, solid surface energy, and the contact diameter, all of which are solid material dependent. The Bu number illustrates a very important point which the Bond number fails to do: the selection of solid materials, when designing reduced gravity fluid systems, is of the utmost importance.

Other dimensionless quantities have attempted to characterize bubble behavior across gravity levels. Pamperin, for example, correlated bubble detachment in reduced gravity to inertial forces of the injected gas [64]. Pamperin used a critical Weber number as the necessary condition for bubble detachment in microgravity. When jetting forces are minimized however, as in the case of this research, buoyancy and surface/interfacial tension forces are the only terms which determine bubble detachment, not the inertial forces caused by gas injection.

9.9 Applications and Implications of Two-Phase Fluids in Variable Gravity

As gravity is decreased, the bubble detachment volume increases proportionally to $g^{-1.5}$. This has significant implications for fluid systems, especially those involving heat and mass transfer, in reduced gravity environments. These critical fluid systems include phase separators, chemical separation processes, ISRU processes, boiling heat exchangers, and ECLSS systems. The nonlinear, power law scaling of the bubble detachment volume means bubbles on the Lunar surface could detach at volumes more than 13 times their detachment volumes on Earth.

As the CFD and theoretical analysis show, however, the increase in bubble volume can be controlled through material selection. Higher surface energy materials, like quartz, should be selected when bubble detachment is wanted, such as in boiling heat exchangers. Another possible alternative to control bubble formation and volumes is surface modification. Artificial surface roughness could be created on a surface to increase the apparent surface energy and thus better control the detachment of bubbles. This is demonstrated by the critical parameter, Bu^*, which serves to predict bubble detachment. Bu^* is only dependent upon the fluid's surface tension and the material properties of apparent surface energy and equilibrium contact angle. This has significant implications for the design of fluid systems. Regardless of fluid density differences or gravity level, the condition for bubble detachment (Bu^*) can only be modified by selection of the fluids and/or selection of the solid material. Designers, therefore, must carefully consider material selection when designing multiphase fluid systems.

The results presented in this dissertation do not only relate to space-related fluid systems. There are many systems on Earth which involve flows in which surface and interfacial tension forces dominate over buoyancy. Microfluidics, for example, rely on surface tension driven flows and often aim to produce or eliminate microbubbles. Again, through the use of material selection and artificial surface roughness, the flow and production of bubbles in microfluidic devices could be controlled. Another application of material selection affecting bubble detachment can be seen in the design of porous electrodes, used in the electrolysis of water. Iwata recently found that the wettability of a porous electrode can significantly impact bubble detachment size [131]. When the wettability of the electrode was increased (via a coating), bubble size dramatically decreased, leading to less electrode clogging and much higher efficiencies [131].

9.10 Forward Work

Additional work could be conducted as part of an ongoing effort to study the effects that reduced gravity levels have on fluid systems. An obvious expansion of the test matrix could be done to include additional orifice plate materials and fluids. Variation in viscosity and densities would be of interest. Two immiscible liquids could also be used to evaluate if the same trends hold when the injected fluid is a liquid instead of a gas. Through material selection and artificial surface roughness generation, the extremes of apparent material surface energies could be tested.

The differences in CFD and experimental results shown for the stainless-steel and aluminum orifice plates will be further explored in future work. It is theorized that the orifice plate CFD boundary conditions are the cause of the differences seen between the CFD and experimental results. First, there exists a singularity at the rim of the orifice in the CFD model, where no constant contact angle can be measured. Further work is needed to determine the most accurate way to account for this singularity at the orifice rim, while maintaining contact angle boundary conditions which accurately reflect the experimental orifice plates. Next, as discussed in Section 9.6.3, the CFD and theoretical analysis assume a constant contact angle. This is generally regarded as a fair assumption, especially on high surface energy materials. However, at lower surface energy materials, the models and the theoretical analysis start to diverge. In order to more appropriately model bubble formation and spreading on an orifice plate, a dynamic contact angle boundary condition, including contact angle hysteresis, would have to be implemented. Dynamic contact angle models and contact angle hysteresis models are much more computationally intensive and require additional measurements by the goniometer, such as advancing and receding contact angles.

Another hypothesis regarding the differences in the CFD and experimental results for stainless steel and aluminum, involves surface roughness near the orifice. Even though the measured contact angles and calculated surface energies for each material were within the published literature ranges as displayed in Table 5.1, the experimental orifice plates could have been affected by surface roughness near the drilled orifice, despite meticulous surface polishing. The contact angles measured by the goniometer were measured on the bulk, nonmachined material away from the orifice. The surface energies calculated from the equilibrium contact angle measurements are called apparent surface energies [132]. Apparent surface energies are those calculated from experimental contact angle measurements, instead of theoretical analysis. The surface energies calculated in Section 5 expectedly matched well with the published surface energy ranges, which also assumed a pristine, nonmachined material. However, surface features, such as the sharp edge of a machined orifice, create different, highly-localized variations in Sessile drop contact angles and thus variations in apparent surface energies [36, 87]. The CFD models use the contact angles measured by the goniometer on the nonmachined material as boundary conditions for the orifice plate. Therefore, the CFD models do not account for any surface roughness near the orifice and may be using boundary conditions which do not accurately represent the apparent surface energy experienced by the bubble as it grows at the orifice. If this is true, the contact angles used as boundary conditions in the CFD did not properly characterize the surface energies of the physical orifice plates and could have been the reason for disagreement between experimental and CFD results for the stainless-steel and aluminum trials. Past literature has shown that surface features, such as surface roughness or sharp edges, can affect a bubble's shape, detachment volume, and ability to spread beyond the orifice [63, 87].

An additional possible cause of the differences observed between experimental and CFD bubble behavior is possible variation in orifice plate surface composition. Although stainless-steel and aluminum are typically noncorrosive, a change in material composition could have occurred when the orifice plates were exposed to oxygen and the moisture experienced during the experimental trials. A change in material composition would have certainly changed the orifice plate's surface energy and therefore bubble volume at detachment.

Future work will therefore focus on modifying CFD boundary conditions to properly model bubble behavior (and thus bubble detachment volume) for the metallic orifice plates. These boundary condition modifications could include dynamic contact angle models, accounting for surface roughness, or other modifications which make the CFD model reflect the bubble behavior observed in the physical experimental trials.

10. SUMMARY AND CONCLUSIONS

The current research presents a broad study of the growth, formation, and buoyancy-driven detachment of a gas bubble from a submerged orifice. This chapter presents a summary of the work completed and important conclusions to be drawn from the work.

10.1 Summary of Work Completed

Five objectives were presented in Section 2.2. The objectives can be divided into three categories: theoretical analysis, experimental, and CFD modeling.

10.1.1 Summary of Theoretical Analysis

A force balance analysis was developed and presented in Section 4. The analysis provides a summary of all forces which act on the bubble and, assuming a low gas injection rate, determines which forces can be neglected for the purposes of force balance analysis.

A dimensionless quantity, the Bubble scaling number (Bu), was also analytically derived and characterizes bubble behavior across gravity levels and orifice plate material properties. A critical value, denoted Bu^*, was then determined as a necessary condition for bubble detachment for a given orifice plate material and fluid combination.

In summary, Research Objective 1 was completed by conducting a force balance analysis of submerged-orifice bubble formation and detachment. A dimensionless quantity was also analytically derived, which scales bubble behavior across gravity levels and orifice plate materials.

10.1.2 Summary of 1 g Empirical Validation

An experimental apparatus, called g-BUBB, was designed and constructed in a 1 g laboratory environment. The experimental research had two main objectives: (1) to determine a sufficiently low gas injection rate to eliminate jetting effects and (2) to collect data for the purposes of 1 g CFD model validation. Both objectives were achieved as high-speed shadowgraphy video was taken of bubbles forming and detaching from four different orifice plates: quartz, polycarbonate, 304 stainless steel, and aluminum 6061. A calibrated imaging system allowed for the measurement of experimental bubble volume.

It was shown using the experimental data, that there exists a sufficiently low gas injection rate, below which, bubble detachment volume was independent of gas injection rate. This gas injection study was successfully completed across all four orifice plate materials and 11 gas injection rates, thus satisfying Research Objective 2.

10.1.3 Summary of Computational Fluid Dynamic (CFD) Research

To satisfy Research Objectives 3 and 4, an axisymmetric, volume of fluid (VOF) CFD model was developed in OpenFOAM, to model the formation and buoyancy-driven detachment of a gas bubble from a submerged orifice. The mesh and computational efficiency of the model were both optimized. The CFD research took place across two phases. First, the CFD models were run to replicate the 1 g laboratory experimental trials for the purposes of model validation. Validation was provided by the 1 g experimental results.

Completing Research Objective 4, good agreement was seen between the quartz and polycarbonate CFD and experimental trials, resulting in a 0.48% difference for quartz and a 21.1% difference for polycarbonate. However, large differences were observed for the stainless-steel and aluminum trials. It was observed that when bubble behavior (shape and spreading) matched well between the CFD models and experimental results, the bubble detachment volumes also matched well.

The second phase of the CFD research aimed to examine the effect that gravitational acceleration has on bubble volume at detachment. Across all materials, bubble detachment volume versus gravity level curves were produced, thus satisfying Research Objective 5. These curves follow a nonlinear, power-law relationship ($V_d \ \propto \ g^{-1.5}$). Since validation is currently unavailable in reduced gravity environments, the curves' shapes were compared to theoretical analysis, past literature, and the dimensionless quantity Bu.

Using CFD results, it was determined that the dimensionless quantity, Bu, can scale bubble volume at detachment across gravity levels and orifice plate material properties.

10.2 Conclusions

Four significant conclusions can be drawn from the presented work:

1. Gas bubble formation and detachment from an orifice submerged in a liquid can be modeled by an asymmetric, volume of fluid (VOF) Computational Fluid Dynamic (CFD) solver. The CFD model's accuracy in 1 g has been validated by empirical data. The CFD model's trends and scaling across gravity levels were compared to and match well with those predicted by the dimensionless quantity Bu.

2. The volume of a bubble, at the point of detachment from a submerged orifice, is directly proportional to $g^{-1.5}$, as g, the acceleration due to gravity, is scaled from microgravity to Earth's gravity.

3. Bubble volume at detachment from an orifice is highly dependent upon the apparent surface energy of the orifice plate. The dependence grows with the decrease of gravitational acceleration. This indicates that heat and mass transfer, caused by bubble detachment, in reduced gravity is highly dependent upon material selection for all components in contact with the fluids.

4. There exists a dimensionless quantity, Bu, which describes submerged orifice bubble behavior across gravity levels and orifice plate material properties. Additionally, a critical value of Bu, denoted Bu^*, was derived. For a given orifice plate material and fluid combination, Bu^* predicts the point at which the bubble will detach from the orifice across all gravity levels. Bu^* is only dependent upon the orifice plate's apparent surface energy and fluid surface tension.

REFERENCES

[1] D. Varnum-Lowry, “Designing and testing an experimental platform in support of partial gravity two-phase fluid physics modeling,” Master’s thesis, Texas A&M University, May 2020.

[2] J. Kim and R. Raj, “Gravity and heater size effects on pool boiling heat transfer,” tech. rep., NASA, May 1, 2014.

[3] C. Burgess, *Aurora 7: The Mercury Space Flight of M. Scott Carpenter*. Bangor, NSW, Australia: Springer International Publishing, 1 ed., 2016.

[4] A. F. Witt, H. C. Gatos, M. Lichtensteiger, M. C. Lavine, and C. J. Herman, “Crystal growth and steadystate segregation under zero gravity: Insb,” *Journal of the Electrochemical Society*, vol. 122, no. 2, pp. 276–283, 1975. 10.1149/1.2134195.

[5] A. F. Witt, H. C. Gatos, M. Lichtensteiger, and C. J. Herman, “Crystal growth and segregation under zero gravity: Ge,” *Journal of the Electrochemical Society*, vol. 125, no. 11, pp. 1832–1840, 1978. 10.1149/1.2131306.

[6] H. Gatos and A. Witt, “Indium antimonide crystal growth experiment m562,” tech. rep., The National Aeronautics and Space Administration (NASA), September 01, 1974.

[7] M. T. Ababneh, C. Tarau, W. G. Anderson, J. T. Farmer, and A. R. Alvarez-Hernandez, “Hybrid heat pipes for lunar and martian surface and high heat flux space applications,” (Hampton), NASA/Langley Research Center, Jul 10, 2016.

[8] G. R. Warrier, V. K. Dhir, and D. F. Chao, “Nucleate pool boiling experiment (npbx) in microgravity: International space station,” *International Journal of Heat and Mass Transfer*, vol. 83, pp. 781–798, 2015.

[9] Y. Barr, G. Clement, and P. Norsk, “Human health countermeasures - partial-gravity analogs workshop,” tech. rep., NASA/Langley Research Center, Jul 1, 2016.

[10] N. Ramachandran, D. Frazier, S. L. L., and C. B. R., “Joint launch + one year science review of usml-1 and usmp-1 with the microgravity measurement group,” (Marshall Space Flight

Center, Alabama), National Aeronautics and Space Administration (NASA), May 1994 May 1994.

[11] R. Naumann, “Usml-1 glovebox experiments,” tech. rep., National Aeronautics and Space Administration (NASA), January 31, 1995.

[12] Y. Kamotani and S. Ostrach, “Design of a thermocapillary flow experiment in reduced gravity,” *Journal of Thermophysics and Heat Transfer*, vol. 1, no. 1, pp. 83–89, 1987. doi: 10.2514/3.10; 05.

[13] Y. Kamotani, S. Ostrach, and A. Pline, “Oscillatory thermocapillary flow experiment (otfe),” tech. rep., National Aeronautics and Space Administration (NASA), May 1, 1994.

[14] Y. Kamotani, S. Ostrach, and A. Pline, “Some results from the surface tension driven convection experiment aboard usml-1 spacelab,” in *32nd Aerospace Sciences Meeting and Exhibit*, (Reston), American Institute of Aeronautics and Astronautics, January 10-13,1994 Jan 1, 1994.

[15] Y. Kamotani, S. Ostrach, and A. Pline, “Analysis of velocity data taken in surface tension driven convection experiment in microgravity,” *Physics of Fluids*, vol. 6, no. 11, pp. 3601–3609, 1994. doi: 10.1063/1.868432; 25.

[16] Y. Kamotani, L. Chao, S. Ostrach, and H. Zhang, “Effects of g jitter on free-surface motion in a cavity,” *Journal of Spacecraft and Rockets*, vol. 32, no. 1, pp. 177–183, 1995. doi: 10.2514/3.26591; 25.

[17] Y. Kamotani, S. Ostrach, and A. Pline, “Some velocity field results from the thermocapillary flow experiment aboard usml-1 spacelab,” *Advances in Space Research; Microgravity Sciences: Results and Analysis of Recent Spaceflights*, vol. 16, no. 7, pp. 79–82, 1995.

[18] Y. Kamotani, S. Ostrach, and A. Pline, “A thermocapillary convection experiment in microgravity,” *Journal of Heat Transfer*, vol. 117, no. 3, pp. 611–618, 1995. SO: Journal of Heat Transfer August 1, 1995 117(3):611.

[19] Y. Kamotani, A. Chang, and S. Ostrach, “Effects of heating mode on steady axisymmetric thermocapillary flows in microgravity,” *Journal of Heat Transfer*, vol. 118, no. 1, pp. 191–

197, 1996. SO: Journal of Heat Transfer February 1, 1996 118(1):191.

[20] Y. Kamotani, A. Chang, and S. Ostrach, "Effects of heating mode on steady axisymmetric thermocapillary flows in microgravity," *Journal of Heat Transfer*, vol. 118, no. 1, pp. 191–197, 1996. SO: Journal of Heat Transfer February 1, 1996 118(1):191.

[21] Y. Kamotani, S. Ostrach, and J. Masud, "Conditions for the onset of oscillatory thermocapillary flows in cylindrical containers with co2 laser heating," in *35th Aerospace Sciences Meeting and Exhibit*, January 1997 1997.

[22] Y. Kamotani, S. Ostrach, and J. Masud, "Oscillatory thermocapillary flows in open cylindrical containers induced by co2 laser heating," *International Journal of Heat and Mass Transfer*, vol. 42, no. 3, pp. 555–564, 1999.

[23] Y. KAMOTANI, S. OSTRACH, and J. MASUD, "Microgravity experiments and analysis of oscillatory thermocapillary flows in cylindrical containers," *Journal of Fluid Mechanics*, vol. 410, pp. 211–233, 2000.

[24] S. Ostrach and A. Pradhan, "Surface-tension induced convection at reduced gravity," *AIAA Journal*, vol. 16, no. 5, pp. 419–424, 1978. doi: 10.2514/3.60906; 01.

[25] S. Ostrach and Y. Kamotani, "Surface tension driven convection experiment (stdce)," tech. rep., National Aeronautics and Space Administration (NASA), June 1, 1996.

[26] S. Ostrach and Y. Kamotani, "Surface tension driven convection experiment-2 (stdce-2)," in *Proceedings of the 1996 3rd Microgravity Fluid Physics Conference, July 13, 1996 - July 15*, (Cleveland, OH, USA), pp. 331–336, Case Western Reserve Univ, Cleveland, United States, NASA, 1996 1996. Compilation and indexing terms, Copyright 2018 Elsevier Inc.; T3: NASA Conference Publication; undefined; undefined; undefined.

[27] J. Leidich, E. A. Thomas, and D. M. Klaus, "A novel testing protocol for evaluating particle behavior in fluid flow under simulated reduced gravity conditions," SAE International, 2009-07-12 2009. ID: 2009-01-2359.

[28] D. Qiu, V. Dhir, M. Hasan, D. Chao, E. Neumann, G. Yee, A. Birchenough, and J. Withrow, "Dynamics of bubble growth on a heated surface under low gravity conditions," 38th

Aerospace Sciences Meeting and Exhibit, American Institute of Aeronautics and Astronautics, 2000. 17; M1: 0; doi:10.2514/6.2000-852.

[29] J. Kim, J. F. Benton, and D. Wisniewski, "Pool boiling heat transfer on small heaters: effect of gravity and subcooling," *International Journal of Heat and Mass Transfer*, vol. 45, no. 19, pp. 3919–3932, 2002.

[30] K. M. Hurlbert, *Flow dynamics for two -phase flows in partial gravities*. PhD thesis, University of Houston, 2000. Compilation and indexing terms, Copyright 2018 Elsevier Inc.; undefined; undefined; undefined; undefined; undefined; undefined; undefined; undefined.

[31] K. M. Hurlbert, L. C. Witte, F. R. Best, and C. Kurwitz, "Scaling two-phase flows to mars and moon gravity conditions," *International Journal of Multiphase Flow*, vol. 30, no. 4, pp. 351–368, 2004.

[32] C. Kurwitz and D. F. Best, "New results in gravity dependent two-phase flow regime mapping," *AIP Conference Proceedings*, vol. 608, no. 1, pp. 14–20, 2002. doi: 10.1063/1.1449703; 21.

[33] C. Kurwitz, ryoji oinuma, and frederick best, "Development and application of vortex liquid / gas phase separator for reduced gravity environment," in *ASME International Mechanical Engineering Congress and Exposition*, vol. 26, (Orlando, Florida USA), p. 226, November 5-11, 2005 2009.

[34] M. G. Cooper, "Growth and departure of individual bubbles at a wall," *Applied Scientific Research*, vol. 38, no. 1, pp. 77–84, 1982. ID: Cooper1982.

[35] M. Ishii and T. Hibiki, *Introduction*, pp. 1–10. Thermo-Fluid Dynamics of Two-Phase Flow, New York, NY: Springer New York, 2011. ID: Ishii2011.

[36] S. D. Bari, D. Lakehal, and A. J. Robinson, "A numerical study of quasi-static gas injected bubble growth: Some aspects of gravity," *International Journal of Heat and Mass Transfer*, vol. 64, pp. 468–482, 2013.

[37] L. Rayleigh, "Viii. on the pressure developed in a liquid during the collapse of a spherical cavity," *null*, vol. 34, no. 200, pp. 94–98, 1917. doi: 10.1080/14786440808635681.

[38] S. Nukiyama, "The maximum and minimum values of the heat q transmitted from metal to boiling water under atmospheric pressure," *International Journal of Heat and Mass Transfer*, vol. 9, no. 12, pp. 1419–1433, 1966.

[39] H. S. Lee and H. Merte, "Spherical vapor bubble growth in uniformly superheated liquids," *International journal of heat and mass transfer*, vol. 39, no. 12, pp. 2427–2447, 1996.

[40] P. D. Marco, P. D. Marco, W. Grassi, and W. Grassi, "Effect of force fields on pool boiling flow patterns in normal and reduced gravity," *Heat and mass transfer*, vol. 45, pp. 959–966, May 2009. ID: Di Marco2009.

[41] S. W. J. Welch, "Direct simulation of vapor bubble growth," *International Journal of Heat and Mass Transfer*, vol. 41, no. 12, pp. 1655–1666, 1998.

[42] V. K. Dhir, M. Asme, and N. Ramanujapu, "G. son dynamics and heat transfer associated with a single bubble during nucleate boiling on a horizontal surface," *Journal of Heat Transfer*, vol. 121, no. 3, pp. 623–631, 1999. 2021.

[43] A. J. Robinson and R. L. Judd, "Bubble growth in a uniform and spatially distributed temperature," *International Journal of Heat and Mass Transfer*, vol. 44, no. 14, pp. 2699–2710, 2001.

[44] V. K. Dhir, H. S. Abarajith, and D. Li, "Bubble dynamics and heat transfer during pool and flow boiling," *Heat transfer engineering*, vol. 28, pp. 608–624, July 1, 2007. doi: 10.1080/01457630701266421.

[45] F. Chiaramonte and J. Joshi, "Workshop on critical issues in microgravity fluids, transport, and reaction processes in advanced human support technology," tech. rep., NASA Glenn Research Center, February 01, 2004.

[46] C. Herman, "Heat transfer and thermal engineering bubble formation and coalescence under the influence of electric fields herman," in *ASME 2013 International Mechanical Engineering Congress and Exposition*, (San Diego, CA), November 15-21, 2013 November 21, 2013.

[47] S. M. O'Shaughnessy and A. J. Robinson, "Numerical investigation of bubble-induced marangoni convection," *Annals of the New York Academy of Sciences*, vol. 1161, pp. 304–

320, April 2009. https://doi.org/10.1111/j.1749-6632.2008.04332.x; 20.

[48] S. Ramakrishnan, R. Kumar, and N. R. Kuloor, "Studies in bubble formationi bubble formation under constant flow conditions," *Chemical Engineering Science*, vol. 24, no. 4, p. 1, 1969.

[49] D. J. McCann and R. G. H. Prince, "Regimes of bubbling at a submerged orifice," *Chemical engineering science*, vol. 26, no. 10, pp. 1505–1512, 1971.

[50] Y. Park, A. L. Tyler, and N. de Nevers, "The chamber orifice interaction in the formation of bubbles," *Chemical Engineering Science*, vol. 32, no. 8, pp. 907–916, 1977.

[51] H. TSUGE and S.-I. HIBINO, "Bubble formation from an orifice submerged in liquids," *Chemical engineering communications*, vol. 22, pp. 63–79, Jul 01, 1983. doi: 10.1080/00986448308940046.

[52] J. N. Lin, S. K. Banerji, and H. Yasuda, "Role of interfacial tension in the formation and the detachment of air bubbles. 1. a single hole on a horizontal plane immersed in water," *Langmuir*, vol. 10, pp. 936–942, March 1, 1994. doi: 10.1021/la00015a054.

[53] M. Jamialahmadi, M. R. Zehtaban, H. Müller-Steinhagen, A. Sarrafi, and J. M. Smith, "Study of bubble formation under constant flow conditions," *Chemical engineering research and design*, vol. 79, no. 5, pp. 523–532, 2001.

[54] S. V. Gnyloskurenko, A. V. Byakova, O. I. Raychenko, and T. Nakamura, "Influence of wetting conditions on bubble formation at orifice in an inviscid liquid. transformation of bubble shape and size," *Colloids and Surfaces A: Physicochemical and Engineering Aspects*, vol. 218, p. 73, May 1, 2003.

[55] A. V. Byakova, S. V. Gnyloskurenko, T. Nakamura, and O. I. Raychenko, "Influence of wetting conditions on bubble formation at orifice in an inviscid liquid: Mechanism of bubble evolution," *Colloids and Surfaces A: Physicochemical and Engineering Aspects*, vol. 229, no. 1, pp. 19–32, 2003.

[56] V. K. Badam, V. Buwa, and F. Durst, "Experimental investigations of regimes of bubble formation on submerged orifices under constant flow condition," *The*

Canadian Journal of Chemical Engineering, vol. 85, no. 3, pp. 257–267, 2007. https://doi.org/10.1002/cjce.5450850301; 20.

[57] H. Wong, D. Rumschitzki, and C. Maldarelli, "Theory and experiment on the low-reynolds-number expansion and contraction of a bubble pinned at a submerged tube tip," *Journal of Fluid Mechanics*, vol. 356, pp. 93–124, 1998.

[58] Z. Xiao and R. B. H. Tan, "An improved model for bubble formation using the boundary-integral method," *Chemical Engineering Science*, vol. 60, no. 1, pp. 179–186, 2005.

[59] B. K. Mori and W. D. Baines, "Bubble departure from cavities," *International journal of heat and mass transfer*, vol. 44, no. 4, pp. 771–783, 2001.

[60] A. A. Kulkarni and J. B. Joshi, "Bubble formation and bubble rise velocity in gasliquid systems: a review," *Industrial and Engineering Chemistry Research*, vol. 44, no. 16, pp. 5873–5931, 2005. doi: 10.1021/ie049131p.

[61] A. Satyanarayana, N. Kuloor, and R. Kumar, "Studies in bubble formation,ăbubble formation under constant pressure conditions," *Chemical Engineering Science*, vol. 24, p. 731, 1969.

[62] A. E. Wraith, "Two stage bubble growth at a submerged plate orifice," *Chemical Engineering Science*, vol. 26, no. 10, pp. 1659–1671, 1971.

[63] A. Marmur and E. Rubin, "Equilibrium shapes and quasi-static formation of bubbles at submerged orifice," *Chemical Engineering Science*, vol. 28, no. 7, pp. 1455–1464, 1973.

[64] O. Pamperin and H.-J. Rath, "Influence of buoyancy on bubble formation at submerged orifices," *Chemical Engineering Science*, vol. 50, no. 19, pp. 3009–3024, 1995.

[65] H. Tsuge, K. Terasaka, W. Koshida, and H. Matsue, "Bubble formation at submerged nozzles for small gas flow rate under low gravity," *Chemical Engineering Science*, vol. 52, no. 20, pp. 3415–3420, 1997.

[66] C. Herman and E. Iacona, "Selection of working fluids for electrohydrodynamic experiments in terrestrial conditions and microgravity," *Heat and Mass Transfer*, vol. 47, no. 8, p. 973, 2011. ID: Herman2011.

[67] E. Iacona, C. Herman, S. Chang, and Z. Liu, "Electric field effect on bubble detachment in reduced gravity environment," 2006. ID: 271092.

[68] T. Acquaviva, E. Julian, D. VanZandt, A. Taylor, N. Grant, C. Herman, H. Nahra, D. Robinson, E. Iacona, and B. Coho, "Enhancement of pool boiling heat transfer and control of bubble motion in microgravity using electric fields (bcoel)," tech. rep., NASA Glenn Research Center, Dec 1, 2001.

[69] W. Fritz, "Berechnung des maximalen volumens von dampfblasen," *Phys. Z.*, vol. 36, no. 11, pp. 157–161, 1935.

[70] F. Suñol and R. González-Cinca, "Effects of gravity level on bubble formation and rise in low-viscosity liquids," *Physical Review E*, vol. 91, no. 5, p. 053009, 2015. ID: 10.1103/PhysRevE.91.053009; J1: PRE.

[71] R. Delombard, J. McQuillen, and D. Chao, "Boiling experiment facility for heat transfer studies in microgravity," tech. rep., American Inst. of Aeronautics and Astronautics, April 01, 2008.

[72] N. Yaddanapudi and J. Kim, "Single bubble heat transfer in saturated pool boiling of fc-72," *Multiphase Science and Technology*, vol. 12, no. 3, pp. 47–63, 2000.

[73] A. Dhruv, E. Balaras, A. Riaz, and J. Kim, "A formulation for high-fidelity simulations of pool boiling in low gravity," *International Journal of Multiphase Flow*, vol. 120, p. 103099, 2019.

[74] S. Singh, V. K. Dhir, and E. Foundation, "Effect of gravity, wall superheat, and liquid subcooling on bubble dynamics during nucleate boiling," (New York, Oahu, HI), pp. 106–113, Begell House;, -01-01 2000. ID: CN050660483.

[75] K. Stephan, *Heat Transfer in Condensation and Boiling*. Stuttgart, Germany: Springer, Berlin, Heidelberg, 1992.

[76] G. Son, V. K. Dhir, and N. Ramanujapu, "Dynamics and heat transfer associated with a single bubble during nucleate boiling on a horizontal surface," *Journal of Heat Transfer*, vol. 121, no. 3, pp. 623–631, 1999. 2021.

[77] V. K. Dhir, "Mechanistic prediction of nucleate boiling heat transferachievable or a hopeless task?," *Journal of heat transfer*, vol. 128, pp. 1–12, Jan 01, 2006. 2021.

[78] A. K. Chesters, "Modes of bubble growth in the slow-formation regime of nucleate pool boiling," *International Journal of Multiphase Flow*, vol. 4, no. 3, pp. 279–302, 1978. ID: 271484.

[79] A. K. Das and P. K. Das, "Bubble evolution through submerged orifice using smoothed particle hydrodynamics: Basic formulation and model validation," *Chemical Engineering Science*, vol. 64, no. 10, pp. 2281–2290, 2009.

[80] A. K. Das and P. K. Das, "Numerical study of bubble formation from submerged orifice under reduced gravity condition," *Procedia IUTAM; IUTAM Symposium on Particle Methods in Fluid Dynamics*, vol. 18, pp. 8–17, 2015.

[81] M. Ohta, D. Kikuchi, Y. Yoshida, and M. Sussman, "Direct numerical simulation of the slow formation process of single bubbles in a viscous liquid," *Journal of Chemical Engineering of Japan*, vol. 40, no. 11, pp. 939–943, 2007. TI:.

[82] M. Ohta, D. Kikuchi, Y. Yoshida, and M. Sussman, "Robust numerical analysis of the dynamic bubble formation process in a viscous liquid," *International Journal of Multiphase Flow*, vol. 37, no. 9, pp. 1059–1071, 2011.

[83] I. Chakraborty, G. Biswas, and P. S. Ghoshdastidar, "Bubble generation in quiescent and coflowing liquids," *International Journal of Heat and Mass Transfer*, vol. 54, no. 21, pp. 4673–4688, 2011.

[84] I. Chakraborty, B. Ray, G. Biswas, F. Durst, A. Sharma, and P. S. Ghoshdastidar, "Computational investigation on bubble detachment from submerged orifice in quiescent liquid under normal and reduced gravity," *Physics of Fluids*, vol. 21, no. 6, p. 062103, 2009. doi: 10.1063/1.3152437; 01.

[85] V. V. Buwa, D. Gerlach, F. Durst, and E. Schlücker, "Numerical simulations of bubble formation on submerged orifices: Period-1 and period-2 bubbling regimes," *Chemical Engineering Science; 8th International Conference on Gas-Liquid and Gas-Liquid-Solid Reactor*

Engineering, vol. 62, no. 24, pp. 7119–7132, 2007.

[86] D. Gerlach, N. Alleborn, V. Buwa, and F. Durst, “Numerical simulation of periodic bubble formation at a submerged orifice with constant gas flow rate,” *Chemical Engineering Science*, vol. 62, no. 7, pp. 2109–2125, 2007.

[87] D. Gerlach, G. Biswas, F. Durst, and V. Kolobaric, “Quasi-static bubble formation on submerged orifices,” *International Journal of Heat and Mass Transfer*, vol. 48, no. 2, pp. 425–438, 2005.

[88] S. D. Bari and A. J. Robinson, “Experimental study of gas injected bubble growth from submerged orifices,” *Experimental Thermal and Fluid Science*, vol. 44, pp. 124–137, 2013.

[89] D. M. Qiu, V. K. Dhir, D. Chao, M. M. Hasan, E. Neumann, G. Yee, and A. Birchenough, “Single-bubble dynamics during pool boiling under low gravity conditions,” *Journal of thermophysics and heat transfer*, vol. 16, pp. 336–345, Jul 2002. doi: 10.2514/2.6710; 23.

[90] S. Manoharan, *Bubble Growth from Submerged Orifices: Investigating the Influence of Surface Wettability, Liquid Properties, and Design Conditions*. PhD thesis, University of Cincinnati, 2016.

[91] R. Ma, B. Wei, and J. Wang, “Theoretical study for bubble diameter prediction at detachment from an orifice in high liquid velocity cross-flow,” *null*, pp. 1–10, 2021. doi: 10.1080/01932691.2021.1883054.

[92] J. Yuan and Y. Li, “Effect of orifice geometry on bubble formation in melt gas injection to prepare aluminum foams,” *Science China Technological Sciences*, vol. 58, no. 1, pp. 64–74, 2015. ID: Yuan2015.

[93] A. Albadawi, D. B. Donoghue, A. J. Robinson, D. B. Murray, and Y. M. C. Delauré, “On the analysis of bubble growth and detachment at low capillary and bond numbers using volume of fluid and level set methods,” *Chemical Engineering Science*, vol. 90, pp. 77–91, 2013.

[94] KDScientific, “Kds legato 100 series user’s manual.”

[95] P. Prime, “Prime capsule portable data logger user manual.”

[96] C. Herman, S. Chang, and E. Iacona, “Bubble detachment in variable gravity under the

influence of electric fields; asme international mechanical engineering congress and exposition," in *International Mechanical Engineering Congress and Exposition*, pp. 241–248, American Society of Mechanical Engineers (ASME), November 1722, 2002 2002. 10.1115/IMECE2002-39688.

[97] D. Group, "Mercury u3v cameras user manual," 2016.

[98] E. Optics, "Techspecs c series fixed focal length lenses," tech. rep., Edmund Optics, 2014.

[99] T. Ziegenhein, D. Lucas, G. Besagni, and F. Inzoli, "Experimental study of the liquid velocity and turbulence in a large-scale air-water counter-current bubble column," *Experimental Thermal and Fluid Science*, vol. 111, 2020.

[100] F. D. Nunno, F. A. Pereira, F. Granata, G. D. Marinis, F. D. Felice, R. Gargano, and M. Miozzi, "A shadowgraphy approach for the 3d lagrangian description of bubbly flows," *Measurement Science and Technology*, vol. 31, no. 10, 2020. Compilation and indexing terms, Copyright 2021 Elsevier Inc.; undefined; undefined; undefined; undefined; undefined; undefined; undefined; undefined.

[101] A. Dash, S. Jahangir, and C. Poelma, "Direct comparison of shadowgraphy and x-ray imaging for void fraction determination," *Measurement Science and Technology*, vol. 29, no. 12, 2018. Compilation and indexing terms, Copyright 2021 Elsevier Inc.; undefined; undefined; undefined; undefined; undefined; undefined; undefined; undefined.

[102] D. Instruments, "Optical contact angle (oca) series," tech. rep., Dataphysics Imstruments.

[103] C.-L. Lai, J. H. Harwell, E. O. A., S. Komatsuzaki, J. Arai, T. Nakakawaji, and Y. Ito, "Adsorption isotherms of perfluorocarbon surfactants from aqueous and non-aqueous solutions and friction measurements of perfluorosurfactant-adsorbed alumina," *Colloids and Surfaces A: Physicochemical and Engineering Aspects*, vol. 104, no. 2, pp. 231–241, 1995.

[104] N. Tasaltin, D. Sanli, A. Joná, A. Kiraz, and C. Erkey, "Preparation and characterization of superhydrophobic surfaces based on hexamethyldisilazane-modified nanoporous alumina," *Nanoscale research letters*, vol. 6, pp. 1–8, December 2011. ID: Tasaltin2011.

[105] A. Zdziennicka, K. Szymczyk, and B. Jaczuk, "Correlation between surface free energy of

quartz and its wettability by aqueous solutions of nonionic, anionic and cationic surfactants," *Journal of colloid and interface science*, vol. 340, no. 2, pp. 243–248, 2009.

[106] D. Enterprises, "Surface energy data for pc: Polycarbonate," tech. rep., June 21, 2018.

[107] K. Azelmad, F. Hamadi, R. Mimouni, A. E. boulani, K. Amzil, and H. Latrache, "Physicochemical characterization of pseudomonas aeruginosa isolated from catering substratum surface and investigation of their theoretical adhesion," *Surfaces and Interfaces*, vol. 12, pp. 26–30, 2018. ID: 314133.

[108] J. D. Bernardin, I. Mudawar, C. B. Walsh, and E. I. Franses, "Contact angle temperature dependence for water droplets on practical aluminum surfaces," *International Journal of Heat and Mass Transfer*, vol. 40, no. 5, pp. 1017–1033, 1997.

[109] Z. Zhang, "A flexible new technique for camera calibration," *IEEE Transactions on Pattern Analysis and Machine Intelligence*, vol. 22, no. 11, pp. 1330–1334, 2000.

[110] Z. Zhang, "Camera calibration with one-dimensional objects," *IEEE Transactions on Pattern Analysis and Machine Intelligence*, vol. 26, no. 7, pp. 892–899, 2004.

[111] M. Hödlmoser, H. Zollner, and M. Kampel, "An evaluation of camera calibration methods using digital low cost cameras," in *Computer Vision Winter Workshop*, (Novt'e Hrady, Czech Republic), Czech Pattern Recognition Society, February 35, 2010 2010.

[112] T. Xue, L. Qu, Z. Cao, and T. Zhang, "Three-dimensional feature parameters measurement of bubbles in gasliquid two-phase flow based on virtual stereo vision," *Flow measurement and instrumentation*, vol. 27, pp. 29–36, October 2012.

[113] J. Estrada-Martínez, J. Reyes-Gasga, R. García-García, N. Vargas-Becerril, M. G. Zapata-Torres, N. V. Gallardo-Rivas, A. M. Mendoza-Martínez, and U. Paramo-García, "Wettability modification of the aisi 304 and 316 stainless steel and glass surfaces by titanium oxide and titanium nitride coating," *Surface and coatings technology*, vol. 330, pp. 61–70, Dec 01, 2017.

[114] NASA, "Marshall space flight center research and technology report," tech. rep., NASA, 2019.

[115] H. Flynn, B. Lusby, and M. Villemarette, “Liquid oxygen/liquid methane integrated propulsion system test bed,” tech. rep., 2011. 26; M1: 0; doi:10.2514/6.2011-5842.

[116] U. A. Systems and NASA, “Nasa extravehicular mobility unit (emu) lss/ssa data book,” tech. rep., NASA, September 2017.

[117] C. W. Hirt and B. D. Nichols, “Volume of fluid (vof) method for the dynamics of free boundaries,” *Journal of Computational Physics*, vol. 39, no. 1, pp. 201–225, 1981.

[118] J. U. Brackbill, D. B. Kothe, and C. Zemach, “A continuum method for modeling surface tension,” *Journal of computational physics*, vol. 100, no. 2, pp. 335–354, 1992.

[119] J. A. Heyns and O. Oxtoby, “Modelling surface tension dominated multiphase flows using the vof approach,” 2014.

[120] W. Haynes, *CRC Handbook of Chemistry and Physics*. CRC Press, 97th ed., June, 2016.

[121] J. Crittenden, R. Trussell, D. Hand, K. Howe, and G. Tchobanoglous, *Appendix C: Physical Properties of Water*, pp. 1861–1862. MWH’s Water Treatment: Principles and Design, Third Edition, John Wiley and Sons, Inc., 2012. 25; https://doi.org/10.1002/9781118131473.app3.

[122] Y. Toulouklan, “Thermophysical properties of matter,” tech. rep., Plenum Publishing Corporation, 1975.

[123] J. Contreras, R. Corral, J. Fernandez-Castaneda, G. Pastor, and C. Vasco, “Semi-unstructured grid methods for turbomachinery applications; asme turbo expo 2002: Power for land, sea, and air,” 2002. 2021.

[124] S. Prakash and C. R. Ethier, “Requirements for mesh resolution in 3d computational hemodynamics,” *Journal of Biomechanical Engineering*, vol. 123, no. 2, pp. 134–144, 2000. 2021.

[125] C. Freitas, “Policy statement on the control of numerical accuracy,” *ASME Journal of Fluids Engineering*, vol. 115, pp. 339–340, 1993.

[126] P. Roache, *Verification and Validation in Computational Science and Engineering*. Albuquerque, NM: Hermosa Publishers, August 1998.

[127] H. K. Versteeg and W. Malalasekera, *An introduction to computational fluid dynamics : the finite volume method*. Harlow, England ;: Pearson Education Ltd., 2nd ed. ed., 2007.

[128] D. Amsallem, M. J. Zahr, and C. Farhat, "On the accuracy and convergence of minimum-residual-based nonlinear reduced-order models in cfd," in *21st AIAA Computational Fluid Dynamics Conference*, Fluid Dynamics and Co-located Conferences, (San Diego, CA), American Institute of Aeronautics and Astronautics, June 24-27, 20213 2013. 04; M1: 0; doi:10.2514/6.2013-2447.

[129] W. Fritz and W. Ende, "Ober den verdampfungsvorgang nach kinematographischen aufnahmen an dampfblasen," *Phys. Z.*, vol. 37, pp. 391–401, 1936.

[130] A. K. Chesters, "An analytical solution for the profile and volume of a small drop or bubble symmetrical about a vertical axis," *Journal of fluid mechanics*, vol. 81, pp. 609–624, August 5, 1977.

[131] R. Iwata, L. Zhang, K. L. Wilke, S. Gong, M. He, B. M. Gallant, and E. N. Wang, "Bubble growth and departure modes on wettable/non-wettable porous foams in alkaline water splitting," *Joule*, 2021. doi: 10.1016/j.joule.2021.02.015; 03.

[132] K. Terpiowski, "Apparent surface free energy of polymer/paper composite material treated by air plasma," *International Journal of Polymer Science*, vol. 2017, 2017.

APPENDIX A

ENGINEERING DRAWINGS OF FLUID CHAMBER PARTS

This appendix presents the engineering drawings used to design and manufacture the fluid chamber components.

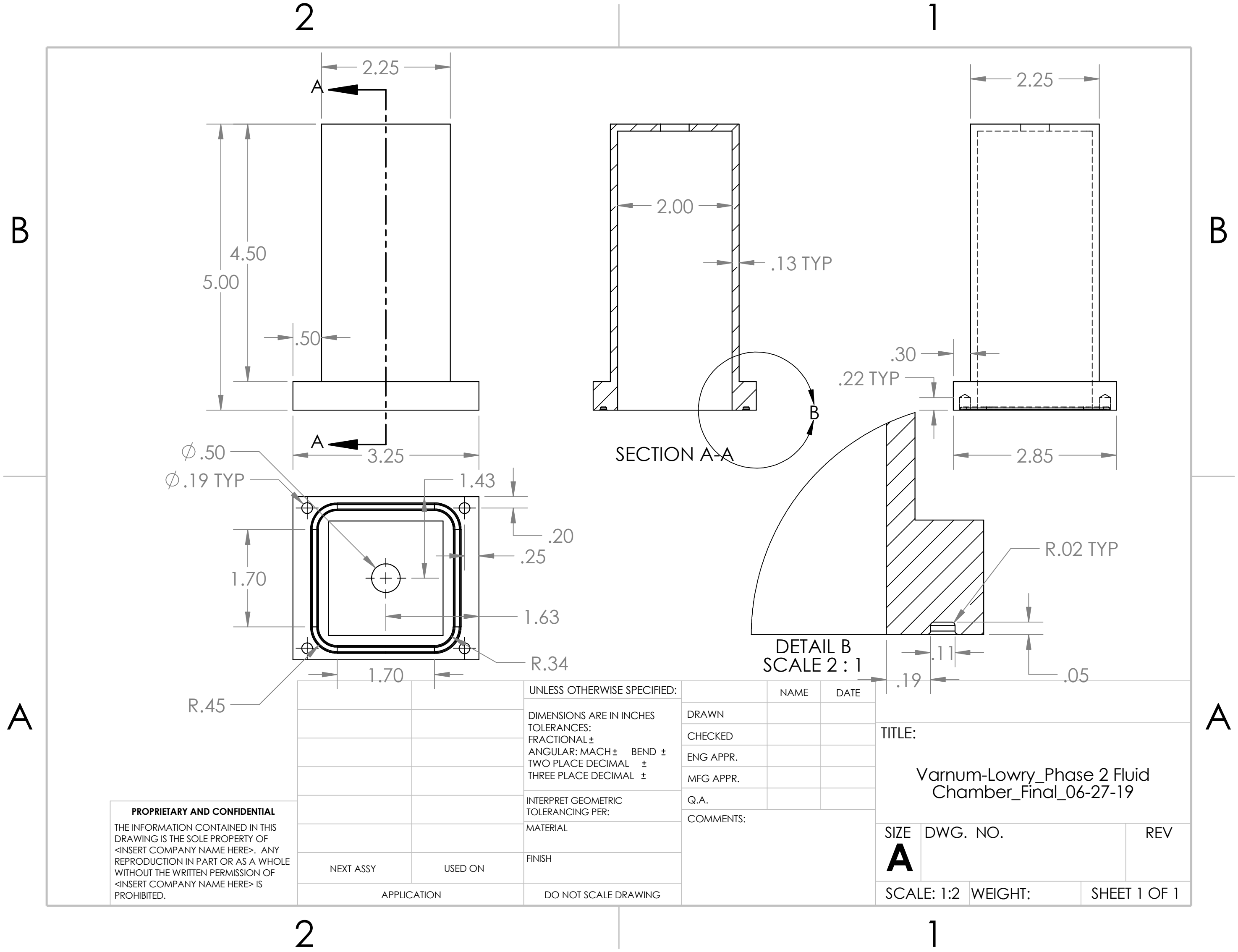

Figure A.1: Engineering drawing of the fluid chamber.

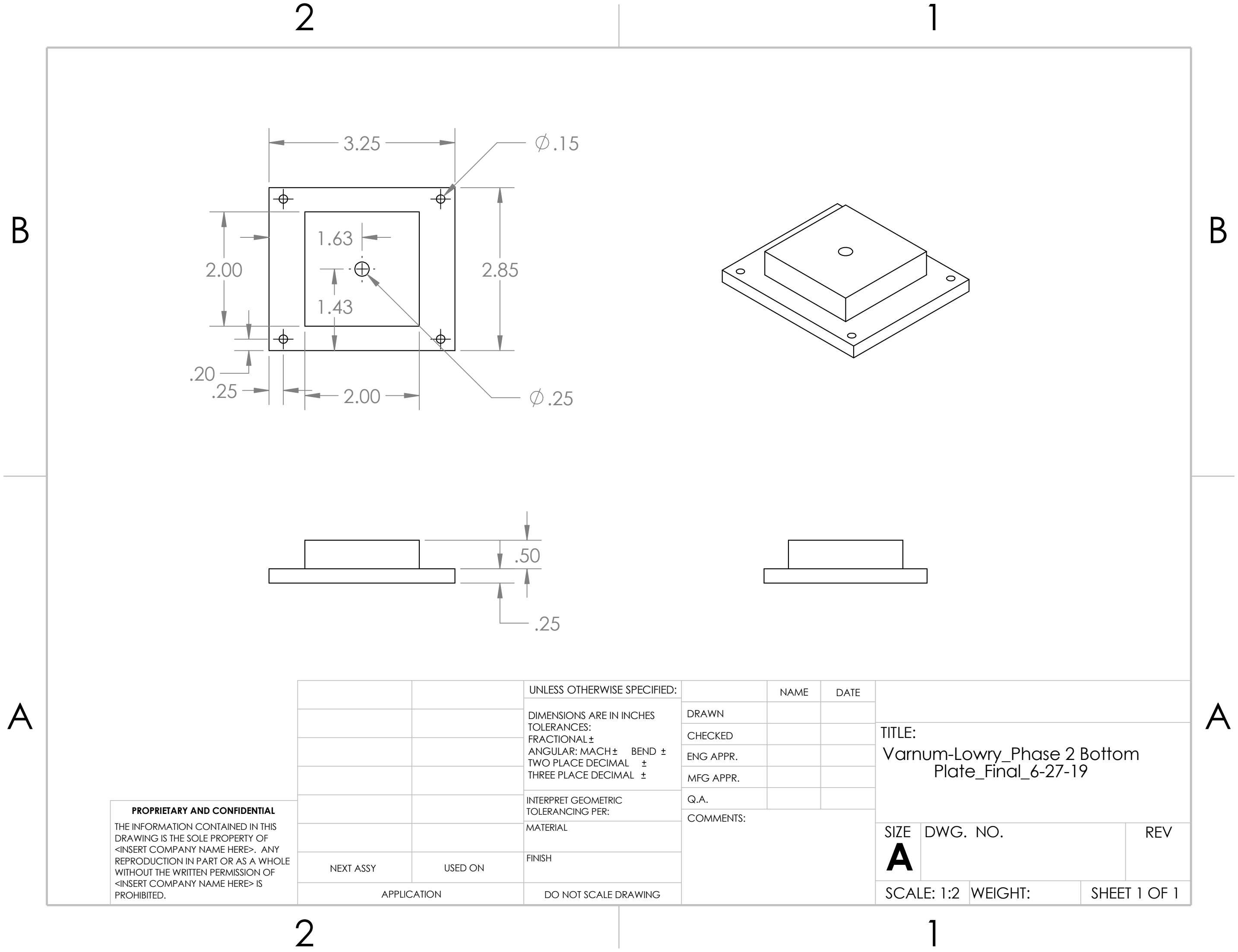

Figure A.2: Engineering drawing of the fluid chamber’s interface plate, which connected to the gas injection system on one side and the orifice plate on the other.

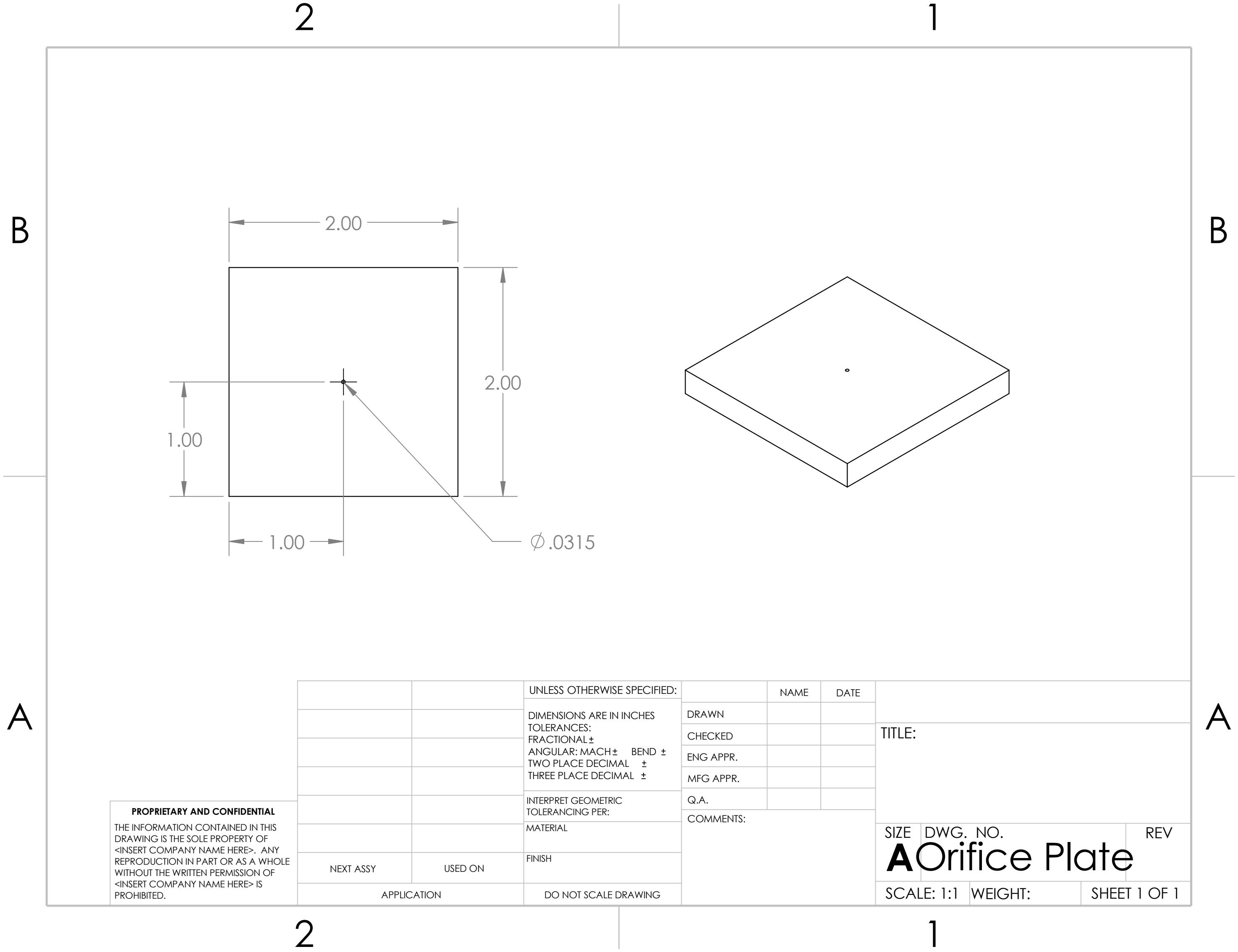

Figure A.3: Engineering drawing of the orifice plate, through which gas was injected into the fluid chamber.